Towards Navigation for Surgical Robotics

Developing a Surgical Robotic Navigation System for the Human Skull

Willem Momma

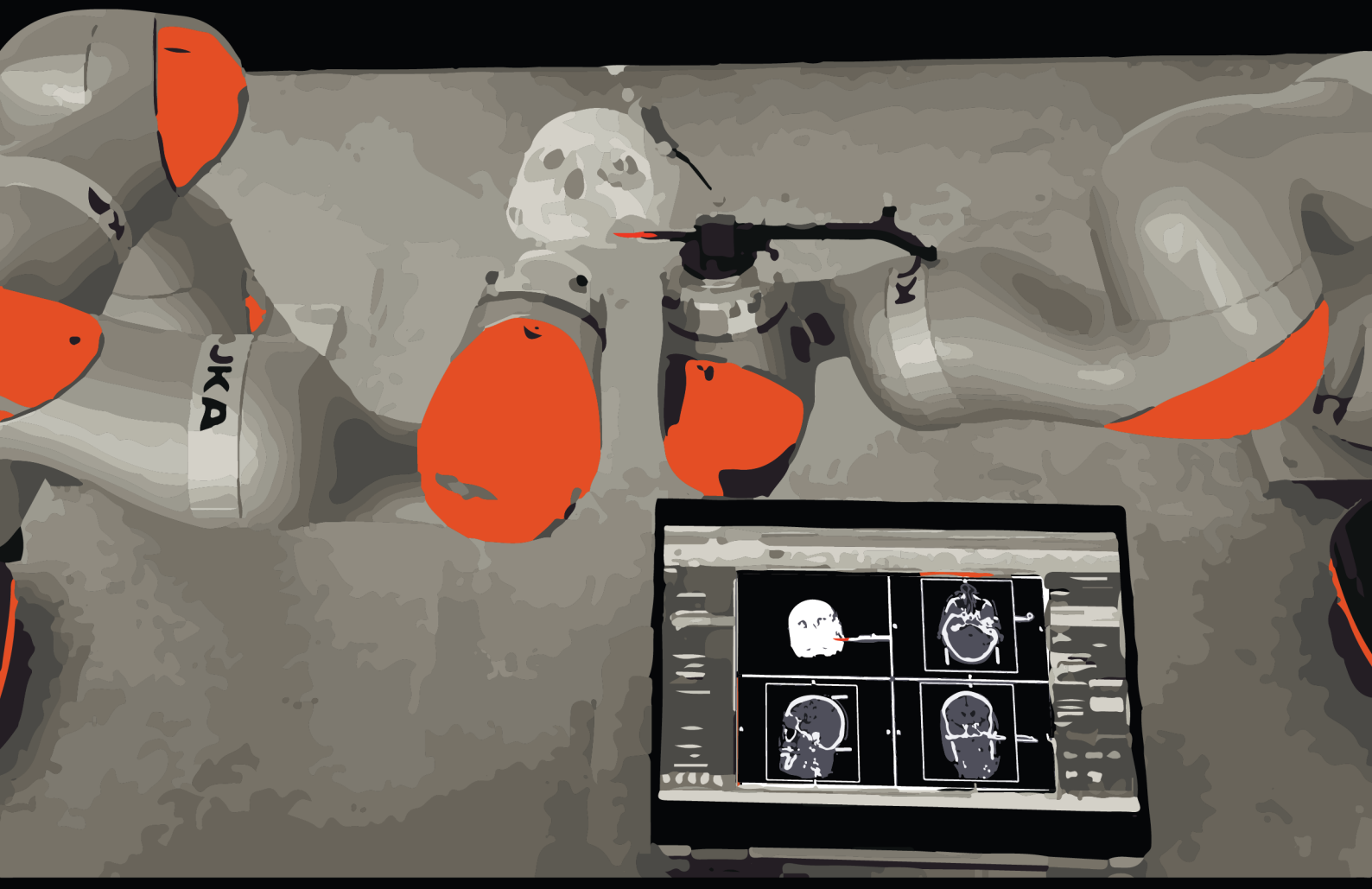

TU Delft

Amsterdam UMC

Towards Navigation for Surgical Robotics

Developing a Surgical Robotic Navigation System for the Human Skull

by

Willem Momma

Thesis committee:

Dr. Ir. Jens Kober:	Chair and supervisor TU Delft
Dr. Tom van Riet:	Supervisor Amsterdam UMC
Dr. Ruud Schreurs	Supervisor Amsterdam UMC
Naomi Rood	Supervisor Amsterdam UMC
Dr. Ir. Micah Prendergast	External examiner TU Delft
Dr. Ir. Dimitra Dodou	External examiner TU Delft

Department of Oral and Maxillofacial Surgery · Amsterdam UMC - location AMC
Faculty ME - Department Cognitive Robotics · Delft University of Technology

Acknowledgments

Over a year ago, this project began for me as an internship at Amsterdam UMC - Department of Oral and Maxillofacial Surgery. In a short amount of time, I was exposed to many different surgeries, gained clinical insights, and explored various research opportunities. Reflecting on this journey, I realize how fortunate I have been to have had the best guiding team in this field, which is why I can look back on this project with joy and pride. This project has been a combined effort of many individuals to whom I wish to express my deepest gratitude.

First and foremost, I would like to express my sincere gratitude to Dr. Ir. J. Kober for arranging this project and supervising me throughout its duration. You efficiently managed everything I needed, right up to organizing the defense and assembling a committee of six members. I especially want to thank you for being available during the final weeks for personal matters and providing the necessary guidance to navigate any issues.

To Dr. T. van Riet, I am amazed at how you found so much time in your busy schedule, juggling multiple roles and jobs, to support your students and this project. Your ability to prioritize this project, despite its demands, is incredibly impressive. I never felt stuck or left waiting for guidance. Thank you for your effort and amazing guidance.

To Dr. R. Schreurs, you are probably the only supervisor in all TU Delft projects who stands with his master's students in Café Nol. Simultaneously, you are also the only mentor who can meticulously deconstruct every sentence of a report, giving the work much-needed direction. Thank you for the countless hours of feedback you have provided.

I want to shine a special light on N. Rood. You have been a mentor, sparring partner, and collaborator throughout this project, excelling in all roles. I had the privilege of pretending to be a technical expert during our collaboration on the review and explaining transformations to you using drawn potatoes. Meanwhile, you provided tremendous help with the clinical aspects and the writing of this project, especially in the final days when working through the night until 3 AM was no problem for you. You have been a lifeline, and I owe you a great deal. I look forward to our future collaborations and hope you will make great use of this experience.

I want to express my thanks to Mees van der Lecq for assisting me during all measurements. This task took many hours, and I would probably still be working on them without your help. I look forward to returning the favor soon for your Master's Thesis. Hopefully, you have enough glow-in-the-dark 3D printing material to keep yourself going for a while.

Finally, I want to thank Kiki Nolen for being the only person in the world, outside of the thesis committee, who has read this thesis from top to bottom, supporting me in the final steps of making this thesis into a complete report.

Abstract

Surgical navigation involves transferring preoperative imaging data, along with preplanned information, onto the patient in the operating theater without using constant radiation. This technique has proven effective and is widely adopted across various surgical specialties. Research has shown a consistent trend in surgical robotics, with numerous initiatives using this technology to navigate the robot's end-effector within the patient's anatomy. For this purpose, commercially available surgical navigation systems are often employed. However, these systems, which are primarily dominated by optical tracking, are not necessarily suited for robotic systems and exhibit limitations such as low update frequency and line-of-sight issues. Additionally, performance reporting in current surgical robotic research is highly inconsistent, and clear guidelines are lacking. This research aims to develop a surgical robotic navigation system to work towards establishing a performance benchmark and systematically assess various error components as a first step toward guiding the field of surgical robotic navigation. To this end, two systems, the Haply System and the Dual-Robot System, have been developed and evaluated for technical accuracy and registration accuracy in both static and dynamic environments. Furthermore, sensor fusion methods have been explored to enhance performance in the Haply system. The results and analysis indicate that the Dual-Robot System is the most accurate in dynamic navigation and presents a viable alternative to optical tracking systems in terms of performance. However, its clinical adoptability remains questionable.

Contents

Nomenclature

List of Abbreviations

CAS	Computer-Assisted Surgery
CBCT	Cone-Beam Computed Tomography
CMF	Craniomaxillofacial
CT	Computed Tomography
DH	Denavit-Hartenberg
DOF	Degrees of Freedom
DRF	Dynamic Reference Frame
FLE	Fiducial Localisation Error
FRE	Fiducial Registration Error
ICP	Iterative Closest Point
LOS	Line of Sight
MDH	Modified Denavit-Hartenberg
MRI	Magnetic Resonance Imaging
MTS	Mechanical Tracking System
OMF	Oral and Maxillofacial
OTS	Optical Tracking System
ROS	Robot Operating System
STL	Stereolithography
SVD	Singular Value Decomposition
TRE	Target Registration Error
URDF	Unified Robot Description Format

List of Figures

List of Tables

1

Introduction

Image-guided surgical navigation is an essential tool across various surgical specialties, designed to localize a surgical instrument intraoperatively in relation to preoperatively obtained image data and virtual planning [1] [2]. This process involves creating a detailed preoperative scan of the patient's anatomy, followed by a virtual plan illustrating the location of critical structures, such as bones or implants. During surgery, this virtual plan is transferred to the patient by establishing a transformation matrix that aligns the real-life anatomy with the image data. Throughout the procedure, both the surgical tool and the patient are continuously tracked, allowing for the real-time visualization of the imaging data without the need for intraoperative radiographic imaging, thereby providing guidance and confirmation to the surgeon. Optical Tracking Systems (OTS), which employ infrared cameras and reflective markers, are the most widely adopted method for tracking in surgical navigation [3] [4] [5]. Despite limitations such as the requirement for constant line of sight (LOS) and a low update frequency [4] [6] [7], optical surgical navigation systems have been shown to effectively reduce postoperative complications [3] [8] [9] and increase surgical accuracy [10].

When introduced into the operating theater, surgical robotic systems with any degree of autonomy or guiding capabilities require advanced surgical navigation technology for effective localization within human anatomy. Robotic manipulators, capable of high accuracy, precision, and immunity to tremors, hold significant potential as surgical tools. These systems can execute small, precise movements that might be difficult for a human surgeon, thereby achieving higher accuracy and reducing the risk of complications [11]. Additionally, equipped with advanced control methods and predictive algorithms, surgical robotic systems can offer semi-autonomous procedures, shared control, and guidance during surgery, potentially reducing the intraoperative workload for surgeons or assistants and improving post-operative outcomes [12]. However, to realize the accuracy and assistance that robots potentially offer, the system's performance is heavily dependent on the employed surgical navigation technology. Existing literature often fails to address critical aspects and understanding regarding both the surgical navigation and the robotic system [13] (Appendix A). For instance, several systems utilize existing optical surgical navigation systems for patient and instrument localization. These systems, however, often have an update frequency far below the control rate of the robotic manipulator and may not complement the accuracy and precision achievable by robotic systems. Additionally, articles frequently neglect to report crucial system information and misinterpret the metrics they present. For example, the authors mention in [11] that the employed robotic manipulator has a repeatability of less than 0.015 mm. This specification, provided by the manufacturer in accordance with ISO 9283 standard task repeatability tests, does not necessarily reflect the positioning accuracy of the robot, which is a far more relevant metric in this context since repeatability only reflects how well a robot can repeat a movement, while accuracy indicates the robot's ability to move to a specified point in space [14]. Moreover, the authors do not mention the performance of the optical tracking navigation system used by the surgical robot, which essentially equals the maximum achievable accuracy of the surgical robotic system. This incomplete and unclear manner of reporting on system performance combined the current surgical navigation systems used in surgical robotic research, severely limits the full potential of robots in surgery.

To address this gap, the authors aim to develop a high-performing surgical robotic navigation system in which each component is thoroughly validated and its individual contribution to overall accuracy is systematically assessed. This research explores and compares different tracking methods for patients and instruments that are suitable for robotic systems. Two system setups, visualized in Figure 1.1, have been developed and systematically assessed under different scenarios. These setups compare optical tracking with alternative methods, including a mechanical patient and instrument tracking system and a haptic feedback controller used as a patient tracker. Additionally,

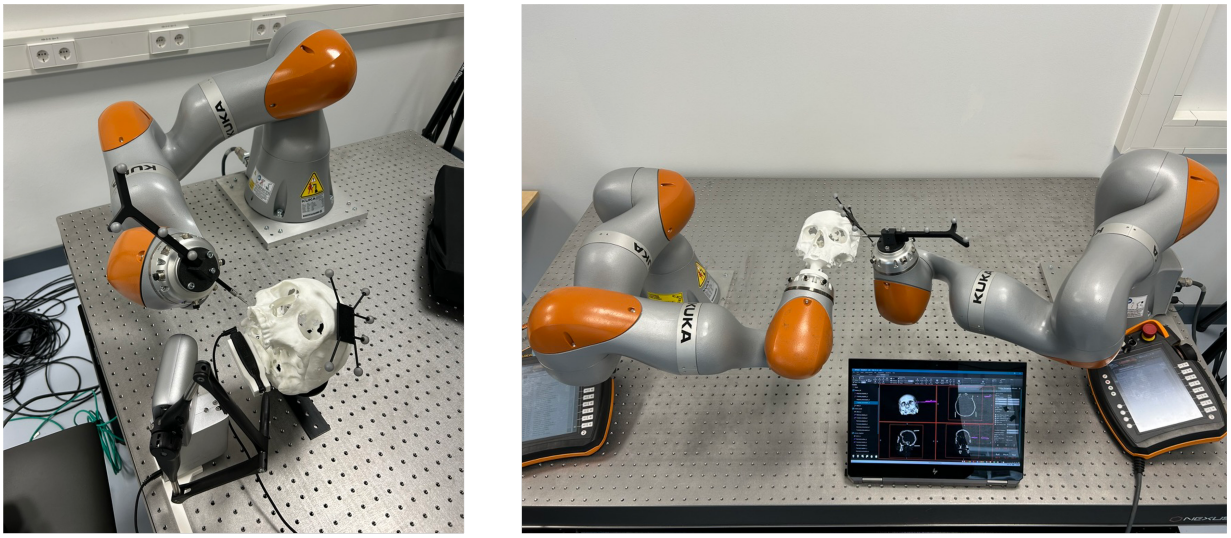

Figure 1.1: A) The Haply System and B) the Dual-Robot System used in this thesis. The Haply System employs the Haply Inverse3 as a patient tracker, while the Dual-Robot System uses a KUKA LBR iiwa 7 for the same purpose. Both systems use a similar phantom skull for evaluation, the OptiTrack system to compare tracking methods, and the KUKA LBR iiwa 14 to hold and track the surgical instrument.

sensor fusion is investigated as a method to enhance performance accuracy. Ultimately, this thesis takes the first steps towards establishing a benchmark for surgical robotic navigation systems and provides a structured approach to performance assessment in an *in-vitro* setup.

1.1. Research Questions

The research motivation and objective can be formulated into the following main research question:

"How can a benchmark surgical robotic navigation system be established utilizing tracking methods suitable for robotic technology and systematically assessed in a reproducible manner to serve as a model for future developments?"

This can be deconstructed into the following sub-questions:

- *How do different tracking devices compare in terms of accuracy, compatibility and reliability for surgical navigation within robotic systems?*
- *How can accuracy errors be systematically assessed in surgical robotic navigation systems?*
- *To what extent can the performance of surgical robotic navigation systems be further enhanced using algorithms such as sensor fusion technology?*

1.2. Contribution and Outline

This thesis presents an extensive evaluation of two surgical navigation setups. The contributions are structured as follows: Chapter 2 describes and motivates the materials and methods used in the experimental work. Chapter 3 details the experiments and their results. Chapter 4 discusses these results and outlines future work. The final chapter, Appendix A, summarizes a systematic review conducted by the author in collaboration with N. Rood. This review systematically identifies a gap in the literature regarding surgical robotic navigation, highlighting the relevance of this research. Both the systematic review and the experimental research detailed in this thesis are intended for publication. Supplementary materials are included in Appendix B and C, providing additional information about the results and detailed design choices, respectively.

2

Materials and Methods

A surgical robotic navigation system comprises hardware and software components designed to localize the end-effector tool of a robotic manipulator within the human anatomy in relation to preoperative imaging data. To navigate within the human anatomy, a patient and instrument tracking device is required, along with a method to transform preoperative imaging data onto the patient. This data is continuously visualized to show the surgical instrument's position relative to the patient. The aim of this research is to establish a surgical robotic navigation system in which different tracking methods can be compared. For a surgical robotic navigation system, the surgical instrument is attached to the end-effector of the robotic manipulator. Therefore, a complete surgical robotic navigation system should include a robotic manipulator equipped with a surgical instrument, a patient and instrument tracking method, and a transformation method to establish the relationship between the patient and the image.

The experiments conducted in this research were performed on two distinct systems, the Haply System and the Dual-Robot System, which used overlapping hardware components and different patient tracking methods. This chapter begins with a description of the hardware components used throughout the research, including their specifications. A section is then dedicated to the validation steps undertaken for the individual hardware components. Following this, the different systems are outlined and explained. Finally, the methods employed in this thesis are presented, including the registration method, robot control, sensor fusion (only applicable to the Haply System), and the suggested framework for performance evaluation.

2.1. Hardware Components

This research relies on advanced hardware components integrated to function as a surgical robotic navigation system. The individual components used in the experimental setups of this research, along with relevant performance metrics, are outlined in this section and visualized in Figure 2.1.

Robotic Manipulators (A, K): This research utilizes two robotic manipulators from KUKA. The first, the KUKA LBR iiwa 14 R820 (A) (KUKA Roboter GmbH, Augsburg, Germany) [15], is employed to hold and track the surgical instrument. The "iiwa" in its name stands for "intelligent industrial work assistant," reflecting its collaborative features. The iiwa series is equipped with advanced force-torque sensors in each joint and features collaborative control modes, allowing manual guidance to specific configurations and poses. This model has 7 degrees of freedom (DOF), a payload capacity of 14 kg, and a reach of 820 mm. It offers a repeatability of 0.015 mm according to ISO 9283 standards [14], although the manufacturer does not provide data on absolute position accuracy. The KUKA LBR iiwa 14 includes a control unit, a smart-pad for direct commands, and a Fast Research Interface (FRI) that supports a 1000 Hz control loop rate for external control [16]. The second manipulator, the KUKA LBR iiwa 7 (K), shares similar features but has a slightly shorter reach of 800 mm, a lower payload of 7 kg, and a higher repeatability of 0.1 mm. It is used exclusively in the Dual-Robot system, where it is attached to a patient phantom to serve as a patient tracker. The KUKA LBR iiwa series has been extensively used in various research applications. The manufacturer is renowned, and their control interfaces offer numerous software development options. Their medical counterpart, the LBR iiwa med, is already employed in commercially available medical systems, which further justifies the selection of these manipulators for this research over other available robots.

Fixation (B, C): Both KUKA robots were mounted to a 1200 x 1800 mm Thorlabs B120180B - Nexus Breadboard, with M6 x 1.0 mounting holes. Two custom-manufactured mounting base plates, featuring M6 threaded holes

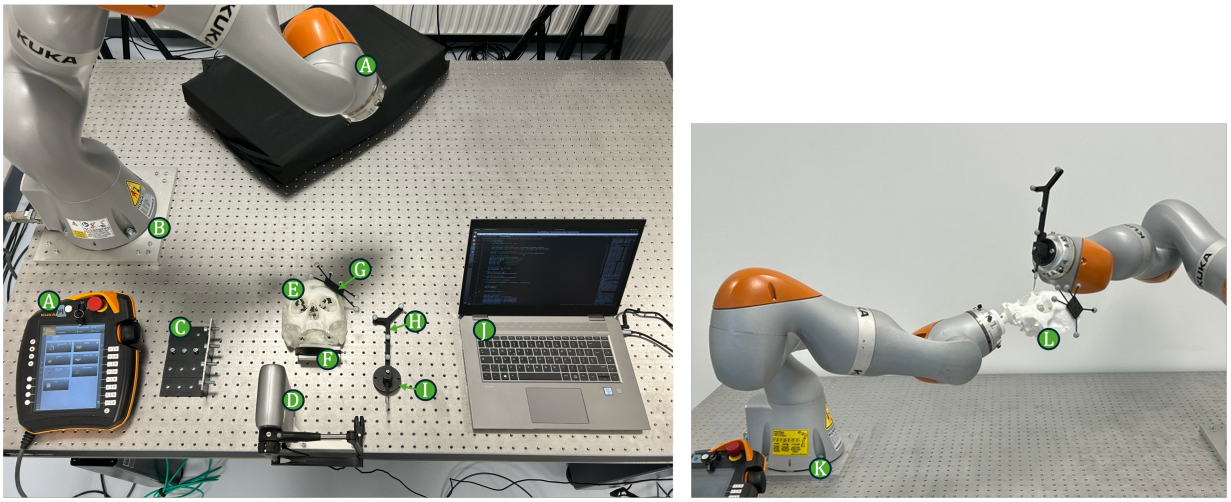

Figure 2.1: Materials used in this research: A) KUKA LBR iiwa 14 Robot, B) mounting plate, C) fixating clamps, D) Haply Inverse3 robot, E) 3D-printed phantom skull, F) Haply VerseGrip Handle, G) OptiTrack reference marker object, H) OptiTrack Digitizer Probe, I) 3D-printed end-effector mount for probe attachment to KUKA, J) PC for system control, K) KUKA LBR iiwa 7 robotic manipulator, L) 3D-printed phantom skull.

spaced 25 mm, were used to attach the robots to the table. Clamps including threaded holes and M8 and M6 bolts were used to rigidly attach phantoms to the breadboard table.

Phantom Head Mount: To test the system in a more dynamic context, particularly with reference to anatomically significant movements, a camera mount featuring a ball socket construction was employed to simulate the movement of the human head relative to the neck. The natural range of motion for a human head without any restraint includes −70 to 70 degrees for left/right rotation, −60 to 60 degrees for cervical flexion/extension, and −40 to 40 degrees for left/right lateralization [17] [18], as illustrated in Figure 2.2. The head mount restricts the workspace to mirror the clinical limitations encountered during surgical procedures. While many surgical robotic research initiatives use a rigidly fixed phantom to perform procedures (see Appendix A), it may be necessary in craniomaxillofacial (CMF) surgery to adjust the patient's head during the operation. To evaluate different scenarios, the head mount was designed to simulate movements of the phantom skull that are similar to those of a patient, assessing the impact of dynamic movement on the navigation system's performance.

Haply System as Patient Tracker (D, F): The Haply Inverse3 (Haply Robotics, Montreal, Quebec, Canada), including the VerseGrip development handle, was selected as a patient tracking device. Although primarily designed as a 6 DOF haptic force feedback controller, its compact design and sufficient workspace made it a potentially viable option for surgical robotic navigation. Prior to this research, an extensive hardware comparison was conducted, as detailed in C. This comparison showed that the Haply system was significantly more cost-effective than other components, had the potential for high-accuracy tracking, and featured a very practical design for clinical applications. By incorporating the Haply system, the aim was to evaluate its accuracy and reliability in comparison to the more established OptiTrack system and to assess its suitability for addressing limitations of optical tracking, such as line-of-sight issues. The Haply Inverse3 consisted of a 3 DOF robotic manipulator with three joints, each equipped with encoders, and a handle that could track orientation around the X, Y, and Z axes. According to the manufacturer's specifications, the Inverse3 device has a update frequency of 4000 Hz and a resolution of 0.1 mm. The specification sheet was not publicly available, and there were no records of accuracy, repeatability, or precision measurements. The Haply was anchored to the table via a 3D-printed custom calibration mount, which dictated the calibration position for the device. The precise method by which the VerseGrip handle estimated orientation remained unclear to the authors. No official update frequency or accuracy measurement was provided, aside from an indication of around 200 Hz. The resolution of the VerseGrip handle was a 16-bit quaternion, indicating that each component of the quaternion could represent 65,536 different values.

Skull Phantoms (E, L): A 3D model of a skull was derived from a cadaver Computed Tomography scan (Siemens Somatom Force, Siemens Healthineers, Forchheim, Germany) using the following scan parameters: 120 kVp, 350 mAs, collimation 0.6 mm, pitch 0.55, 250 mm FOV diameter, 512x512 matrix size, 1.0 mm slice thickness, and 0.7 mm slice increment, with an Hr 64 bone kernel. Using Blender, six registration fiducials and six target points

were added, designed as half-sphere slots (1 mm diameter) for precise positioning of the digitizing probe tip. For the Haply System, a mold was created from the Haply VerseGrip 3D model and integrated into the phantom to allow attachment of the Haply VerseGrip. The VerseGrip has a ball at which the end-effector of the Haply can be attached via a socket construction. This skull phantom was printed by an external party (Oceanz 3D Printing, Ede, the Netherlands) using Polyamide 12 material and an EOS Formiga p100 Selective Laser Sintering 3D printer with a print thickness of 0.12 mm. For the Dual-Robot System, the same 3D model was used, but the mounting was adjusted to be directly attachable to the end-effector flange of the KUKA LBR iiwa 7. This phantom was printed on a Bambulab P1s 3D printer using PLA material, with print settings including a layer height of 0.1 mm, a nozzle diameter of 0.2 mm, and an infill density of 20%.

OptiTrack as Patient and Instrument Tracking System: The OptiTrack system consists of nine Prime X13W cameras and two Prime X13 cameras, all connected via Ethernet to a Windows PC that runs the Motive software (version 2.1; NaturalPoint Inc., Corvallis, Oregon, USA). This arrangement of 11 cameras, mounted on four tripods around the mounting table and positioned at various heights and angles, aims to minimize field-of-view overlap, which theoretically enhances tracking accuracy. The system is capable of sampling at a maximum rate of 240 Hz. Specifically, the Prime X13 camera achieves a 3D accuracy of 0.20 mm, and the Prime X13W reaches a 3D accuracy of 0.30 mm [19]. The methodology for determining this accuracy is not specified.

To calibrate, the cameras were positioned around the tracking volume at varying heights. Subsequently, the focus and focal lengths of the cameras were adjusted to center on a marker in the middle of the tracking volume. The exposure was set to 100 μs, the frequency to 100 Hz, the tracking volume cleared, objects masked, and the tracking wand along with the wanding calibration method of OptiTrack was employed to calibrate the system by collecting a sufficient number of samples for high-quality results. Upon completion of the calibration, the frequency was reset to 240 Hz to optimize tracking performance.

Dynamic Reference Array (G): The OptiTrack Rigid Body marker base with 12 mm diameter markers were attached to the phantom skull. The markers attached are defined as a rigid body in the OptiTrack Motive software which provides 6 DOF real-time pose estimation of the geometrical center of the markers at the operating frequency of the OptiTrack system.

Surgical Instrument (H, I): An OptiTrack Micron Series Digitizing Probe (H) was used as a surgical pointer instrument to indicate landmarks on the phantom. A custom 3D-printed mount (I) rigidly attached the probe to the robot's end-effector flange. The probe has a sphere as tool-tip with a diameter of 1 mm [20]. The probe, rigidly fixed in the end-effector flange mount, was measured using a micron digital caliper to update the kinematic model of the KUKA LBR iiwa 14, such that it includes the spatial information of the end-effector tool in its calculations.

Control PC, desktop, monitor and communication switch (J): The OptiTrack cameras and robot are connected over a local network via a network switch. A laptop and desktop computer both running Linux are also connected to the switch. The desktop runs the direct control commands to the robot and the communication of the OptiTrack system. The laptop handles any other data processing communication node, further explained in the software section. The desktop, monitor and communication switch are not visible in the picture. A monitor is used to display the probe in the DICOM image of the cadaver. The role of the Ethernet switch is to provide stable communication over a wired network at high speed, it can transfer data up to 1000 megabytes per second.

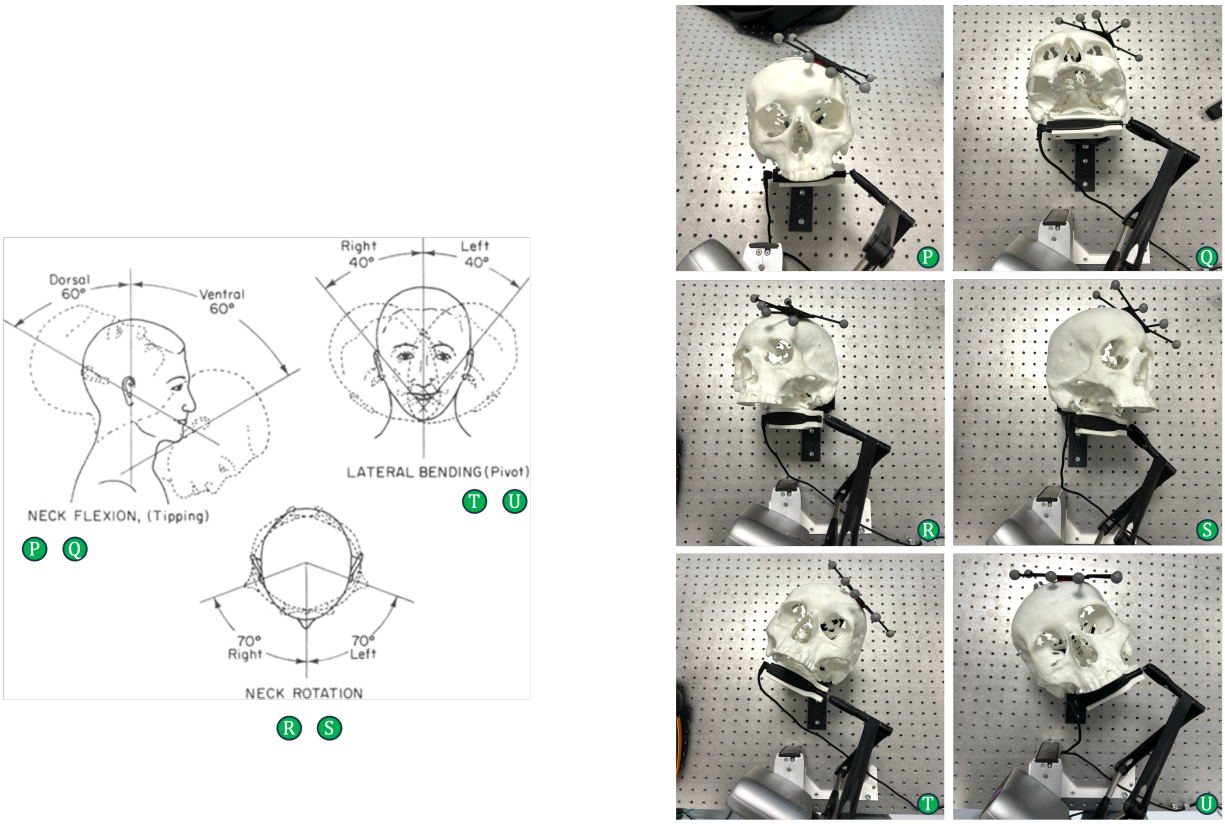

Figure 2.2: An illustration of the "workspace" of a human head [18] next to the proposed setup head mount for the phantom skull. The phantom skull mount allows for simulating the neck flexion (P,Q), lateral bending (T,U), and neck rotation (R,S).

2.2. Hardware Validation

In the process of hardware selection, it is not always immediately apparent what specific measures entail. For instance, while the Haply System specifies only its resolution and suggests potential for high accuracy, it does not provide explicit accuracy measurements. Similarly, robotic manipulators often provide only repeatability measurements, lacking detailed accuracy data. Although OptiTrack lists 3D accuracy per camera, these figures do not necessarily reflect the overall system performance, and the methods used to measure this accuracy remain unspecified. Therefore, before proceeding to establish a surgical navigation setup and conducting experiments, it is crucial to assess each component individually to gauge their performance and identify any significant systemic errors.

For the individual patient and instrument tracking hardware—including both robotic manipulators, the OptiTrack system, and the Haply System—initial tests were conducted. These tests were designed to provide an indication of their performance and to detect any significant systemic errors.

Robotic Manipulators Validation

The robots calculate the end-effector position using joint encoder measurements and forward kinematics based on a kinematic model. Generally, robots exhibit high repeatability; however, their positioning accuracy is often lower due to mechanical inaccuracies in the fabrication process. Repeatability refers to the robot's ability to replicate a particular movement multiple times, while positioning accuracy is its capability to reach a pose in space as commanded [14]. Positioning accuracy is influenced by several factors, including backlash, the efficiency of electrical drives, the accuracy of joint encoders, the control method employed, and the internal kinematic model [21]. The kinematic model is responsible for the end-effector position values provided by the robot, derived from joint sensor readings; it maps the joint state to the end-effector state.

In this thesis, the focus is on localization; thus, the robot is manually directed to target points using impedance control. The accuracy here depends solely on the calculations from joint sensor readings, hence, the kinematic model and joint encoder accuracy. Deviations between the actual robot and its inherent kinematic model can lead

to significant errors in end-effector position calculations. This discrepancy can be addressed through kinematic calibration, using a more accurate device such as a laser tracker or coordinate measuring machine to align the robot's actual pose with the measured pose [22].

Initial tests were conducted using the KUKA LBR iiwa 14 and its counterpart, the LBR iiwa 7, both equipped with a simple cone-shaped end-effector mount, see Figure 2.3. These tests aimed to provide an indication of the Target Registration Error, as detailed in Equation (2.17) and discussed in Section 3.1, against a 3D-printed phantom. The results did not reveal any significant systemic errors, indicating minimal kinematic discrepancies. Given the lack of standard kinematic calibration software for 7-DOF robotic manipulators, the unavailability of essential equipment like a laser tracker, and the absence of severe kinematic errors, it was decided not to proceed with calibrating the robot.

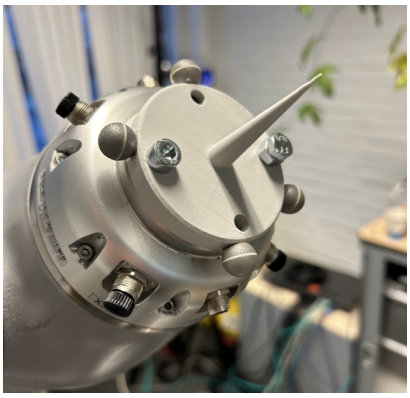

Figure 2.3: The cone-shaped 3D-printed end-effector used on the KUKA LBR iiwa 14 and iiwa 7 during initial hardware validation.

OptiTrack System Validation
Following the implementation of the initial 3D-printed end-effector mount on the KUKA robotic manipulators, an improved version was developed that included threading for infrared reflective markers to be tracked by the OptiTrack system, as shown in Figure 2.4. Using the marker configuration and Motive software, the geometric center calculated by Motive was aligned with the tip of the end-effector. When tested on the target skull, these measurements were found to be inaccurate, exceeding 3 mm, indicating systemic errors. In response, the manufacturer was consulted, and they provided results from tests conducted by their partners, as well as a series of experiments in similar setups. These results were achieved using the Digitizer Probe and the OptiTrack calibration block, both of which were subsequently acquired for this research.

Upon validation using the calibration block, the probe exhibited far fewer systemic inaccuracies but did not achieve the accuracies reported in OptiTrack's micron experiments. The manufacturer attributed this discrepancy to factors such as reflections, lighting conditions, camera distribution, and camera type, which affected the performance. Given that optimal camera conditions are challenging to replicate in an operating theater, it was deemed not useful to attempt to recreate these conditions in our system setup.

Haply System Validation
From initial device positional analysis, the Haply demonstrated a steep slope in the negative Z-direction when observed from the XZ plane, and a curved slope from the YZ plane. Initial rough point estimates on the flat table suggested a systemic kinematic error, as depicted in Figure 2.5. Upon consultation with the manufacturer, Haply indicated that these errors might result from the provided calibration method inaccuracies and an internal accelerometer in the Inverse3 device, which alters the base coordinate frame. Due to the device's intended application as a haptic controller, this discrepancy had not previously posed significant issues, given the lower accuracy requirements.

Figure 2.4: 3D-printed end-effector with iterated design improvements and threaded attachment points for 12 mm OptiTrack markers.

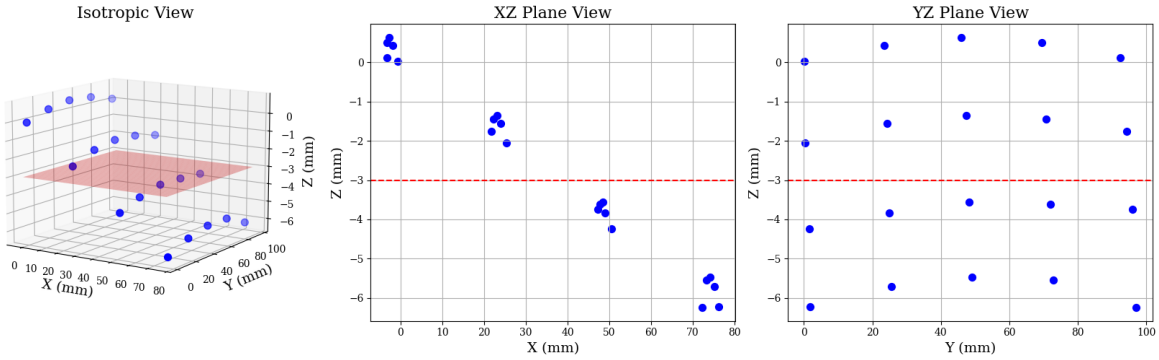

Figure 2.5: Measurements of 20 points, evenly spaced at 25 mm intervals, on the flat surface of the mounting table by the Haply Inverse3. The left plot displays an isotropic 3D view, while the middle and right plots show projections on the XZ and YZ planes, respectively. The red plane and lines represent the expected positions of the measured points. Deviations from these expected positions indicate the kinematic errors of the Haply Inverse3 system.

To address the offset in the Haply measurements, a 3D model was designed in Solidworks (Solidworks Corp., Waltham, Massachusetts, USA) to create a calibration mount, visualized in Figure 2.6. The Solidworks analysis accurately estimated the angles for the head, inner, and outer joints. Although Haply Robotics did not provide access to the kinematic model of the system or any specific calibration methods due to intellectual property constraints, they did offer a way to set the angles to a known configuration via the Hardware API. Using the 3D printed mount, the Haply was adjusted to this initial state, setting the angles to [-89.18, 86.76, -1.45] for the head, inner, and outer arm, respectively. This adjustment, in combination with switching off the internal accelerometer, reduced the z-axis error to a deviation from 10 mm to 1 mm over the workspace of the device.

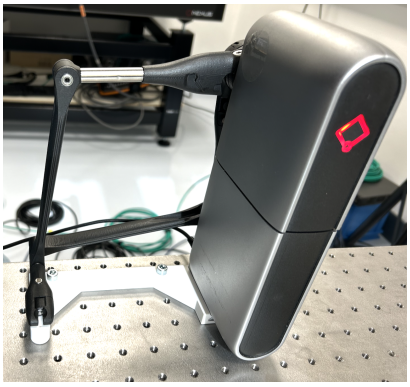

Figure 2.6: 3D-printed calibration mount to fixate the Haply Inverse3 onto the table, in the starting calibration position to provide the system with the correct angles corresponding to the encoder readings.

2.3. Description of the Two Systems

From the selected hardware components, two surgical robotic navigation systems have been developed using overlapping components and software described in Section 2.1. The goal of this research is to systematically assess the performance of different patient and instrument tracking methods and explore sensor fusion technology as a means of performance enhancement. The Haply System explores a cost-effective and practical patient tracking alternative and the incorporation of sensor fusion, while the Dual-Robot System compares a complete mechanical tracking system utilizing two robotic manipulators with an optical tracking system.

Figure 2.7 shows the Haply System in an experimental setup with the different coordinate reference frames used in the system. This system utilizes the Haply Inverse3 haptic controller to track the patient phantom. It also redundantly tracks the patient and instrument through the OptiTrack system for comparison and sensor fusion methods. The patient phantom is fixed to the head mount as described in Figure 2.2.

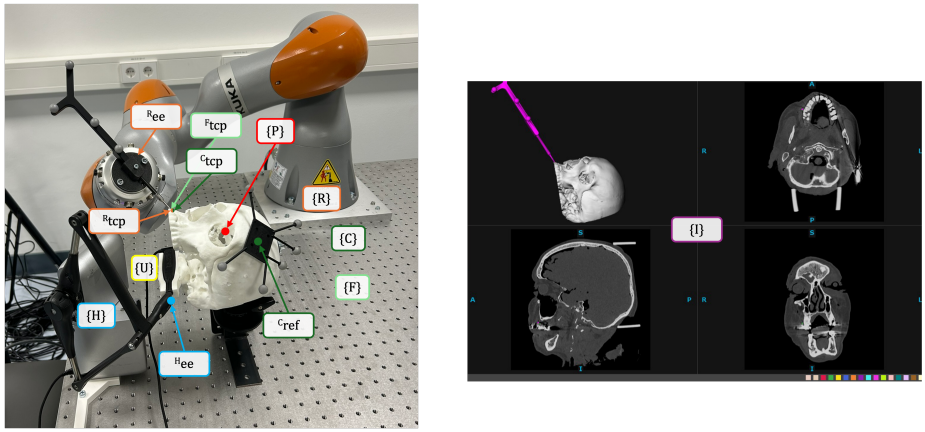

Figure 2.7: Coordinate frames used by the robotic navigation system. $\{R\}$ is the KUKA robot base frame, R_{ee} is the robot end-effector in $\{R\}$, R_{tcp} is the tool center point of the measurement probe in the robot, C_{tcp} is the tool center point measured in the OptiTrack base, $\{C\}$ is the OptiTrack ground base frame, $\{P\}$ is the patient frame, $\{H\}$ is the Haply robot base frame, C_{ref} is the dynamic reference frame measured in the OptiTrack base frame, H_{ee} is the Haply end-effector point in $\{H\}$, $\{I\}$ is the image frame which contains the preoperative imaging data and planning information.

The second navigation system is built to compare the effectiveness of a Mechanical Tracking System (MTS) against an Optical Tracking System (OTS). The system, shown in Figure 2.8, can track the phantom by communication between the two robots or by using the OptiTrack system.

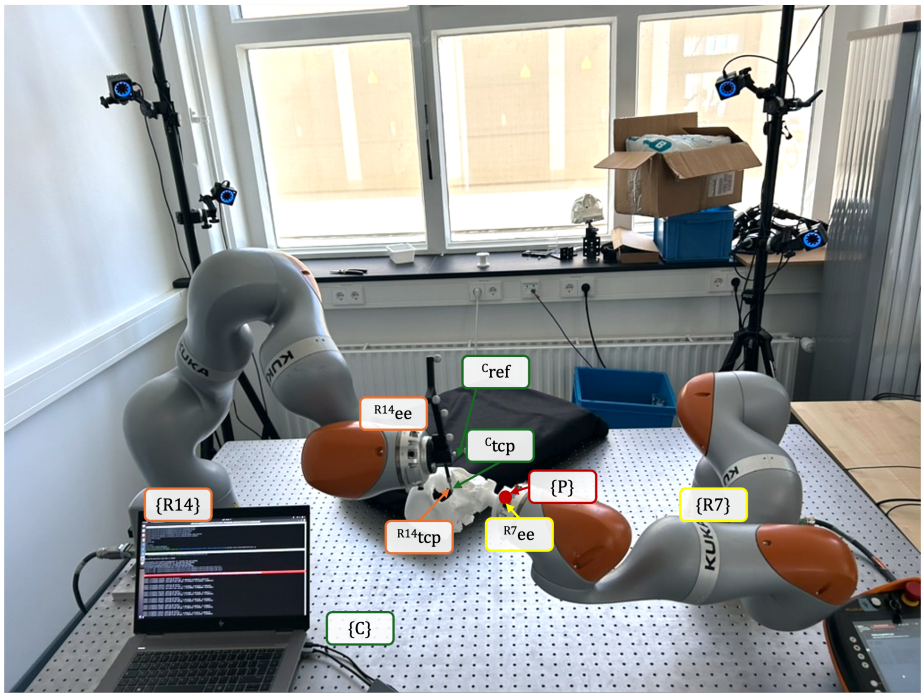

Figure 2.8: Surgical robotic navigation system featuring two KUKA robotic manipulators, LBR iiwa 14 and LBR iiwa 7. $\{R14\}$ and $\{R7\}$ are the base frames of the robotic manipulators. $R14_{ee}$ and $R7_{ee}$ are the end-effector frames, while $R14_{tcp}$ is the tool center point measured at the end-effector of the LBR iiwa 14. C_{tcp} is the tool center point measured in the OptiTrack system base frame, $\{C\}$ is the OptiTrack ground base frame, and C_{ref} is the dynamic reference frame measured in the OptiTrack base frame. Active OptiTrack cameras are visible behind the robots.

2.3.1. Software and Data Communication Haply System

In both systems Robot Operating System (ROS) is used for managing communication between various hardware components and their corresponding firmware. Figure 2.9 offers a general overview of this communication flow. ROS's fundamental functionality is built around nodes (processes that perform computation), topics (named buses for nodes to exchange messages), and the messages themselves (data structures for communication) [23]. Nodes can either subscribe to topics to receive messages or publish messages to these topics, creating a versatile framework for inter-process communication. In the figure, the oval elements represent the nodes, and the rounded square elements symbolize the topics in the robotic navigation system. Within these nodes, various processes like transformation, synchronization, filtering, and control methods are executed, which are elaborated in subsequent sections.

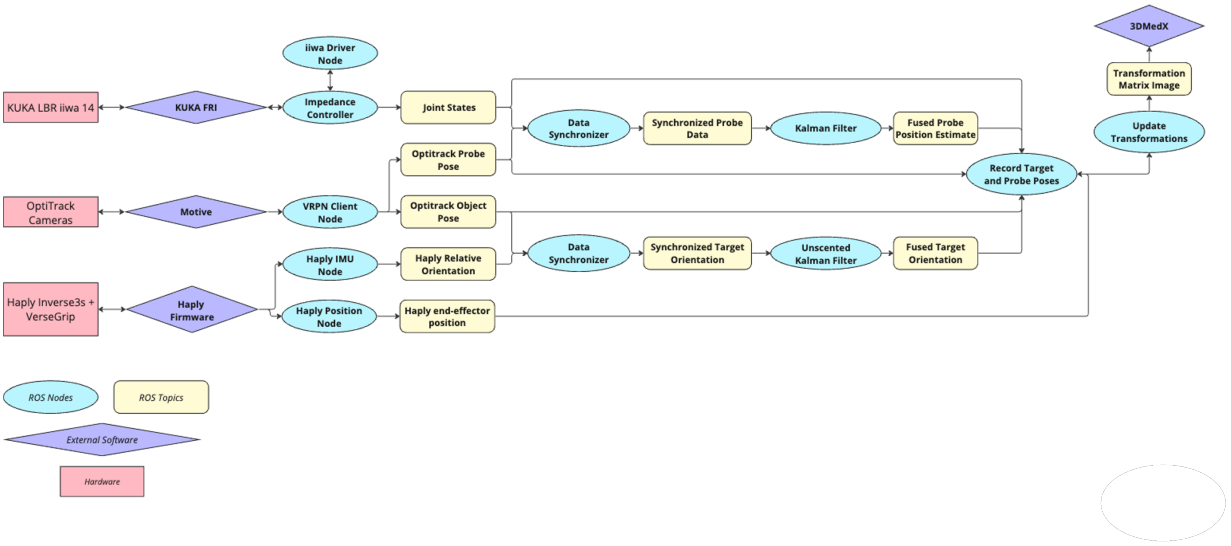

Figure 2.9: Data communication flow in the Haply System. Oval shapes represent ROS nodes, rounded yellow square shapes denote ROS topics, diamond-shaped boxes indicate external software or firmware applications, and the red squared boxes indicate the hardware components.

Communication with applications on the robot is facilitated through an implementation of the IIWA ROS stack [24]. This setup bridges the communication between the KUKA Fast Research Interface (FRI) and ROS. Java scripts, along with the Fast Research Interface and the IIWA ROS stack installed on the Sunrise cabinet, enable interaction between the Sunrise application and the ROS network. This setup empowers researchers to develop programs, for instance in Python, to extract data from the robot and send high-level commands.

Several specific implementations and libraries are employed in this system:

- For transformation algorithms, the SciKit-Surgery library, designed for surgical navigation, is used [25].
- Sensor fusion algorithms have been developed using the FilterPy library.
- The OptiTrack system relies on its native Motive (version 2.1) software for data streaming, which connects with the rest of the system through a VRPN client in ROS [19].
- The 3DMedX (v1 Radboudumc 3D Lab, Nijmegen, the Netherlands) application is utilized for visualizing the probe within the skull and displaying skull DICOM images.
- SolidWorks [26] and Blender [27] have been used for 3D modeling of the 3D-printed components in the system.
- Robotic toolbox for fast kinematic calculations using Python [28].

2.3.2. Software and Data Communication Dual-Robot System

Like the Haply System , the Dual-Robot System leverages ROS to integrate tracking and control data from both KUKA robots and the OptiTrack system. The system's architecture is shown in Figure 2.10. The OptiTrack system, using Motive software, tracks both the Digitizer Probe and Dynamic Reference Array. It provides pose data in the global camera frame to the ROS network through the VRPN client node. The Digitizer Probe's pose is then transformed into the local frame of the Dynamic Reference Array, as detailed in Section 2.3.4.

The KUKA LBR iiwa 14 and iiwa 7 robots are interfaced via KUKA's Fast Research Interface (FRI) protocol [24]. Similar to the Haply System , the robot controller nodes communicate with the iiwa driver to control the robots. Each robot is launched independently over the same ROS network using unique namespaces ('iiwa14' and 'iiwa7'). These namespaces ensure that topics, parameters, and services don't interfere with one another. Launch files accept arguments to specify the namespace, robot model, and controller type, enabling both robots to be launched and controlled simultaneously within their respective namespaces.

In the 'Transform End-effector' node, each robot's pose is transformed based on a predetermined static transformation broadcasted using tf2_ros over the ROS network between the 'iiwa14' base and the 'iiwa7' base. The 'Calculate

Relative Pose' node then computes the position of the iiwa 14 end-effector in the iiwa 7 frame, functioning similarly to how the Digitizer Probe and Dynamic Reference Array interact.

The final system output is achieved by synchronizing the probe and reference frame data with the transformed end-effector positions of both iiwa robots. The 'Synchronized Sampling' node calculates the relative poses of the two robots and the probe, resulting in the position of the iiwa 14 end-effector in the iiwa 7 frame.

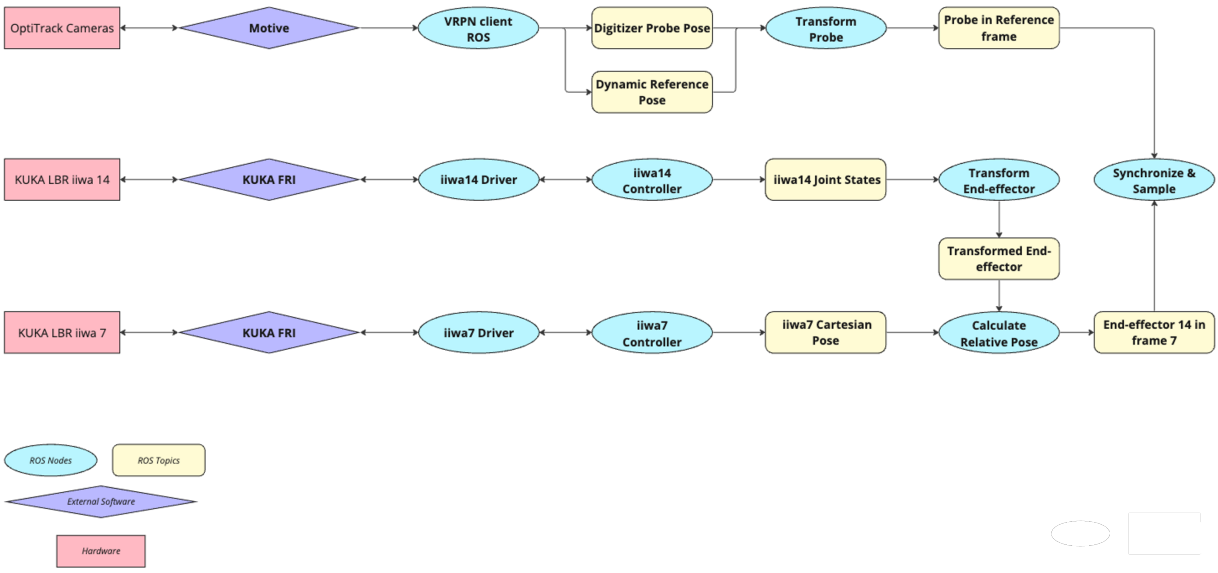

Figure 2.10: Data communication flow in the Dual-Robot System . Oval shapes represent ROS nodes, rounded yellow square shapes denote ROS topics, diamond-shaped boxes indicate external software or firmware applications, and the red squared boxes indicate the hardware components.

2.3.3. Transformations in the Haply System

The main method to align the patient frame with the image frame is through registration, which is outlined in 2.4. In generally available surgical navigation systems, a single tracking device is often used with one general global reference frame, a Dynamic Reference Frame (DRF), and the frame of the surgical instrument. Points are then sampled by computing the relative distance between the surgical instrument and the DRF. This ensures that if the patient moves, the DRF changes in the global frame, but the relative distance does not, allowing registration and navigation to continue. Due to hardware restrictions, the use of multiple systems with different reference frames, and the absence of a kinematic model or known reference from which the Haply samples, the navigation system transformation needs to be constructed in a different manner, as outlined below. As shown in Figure 2.9 the system fetches the positional data from multiple sources and then updates the transformations accordingly.

Updating Transformation Matrices with Movement Data

Dynamic surgical navigation systems require precise and adaptable transformations to accurately map the tools' position in real-time, especially when there is movement of the patient. The registration algorithm, later explained in Section 2.4, initially provides a rotation matrix $\mathbf{R}_{\text{init}}$ and a translation vector $\mathbf{T}_{\text{init}}$ to map points from the instrument's frame to the image frame. However, patient movement necessitates the recalculation of these transformations to maintain accuracy.

Global Transformation Matrix

The core of this recalculation is the computation of the global transformation matrix $\mathbf{M}_{\text{global}}$. This matrix accounts for changes in both position and orientation due to patient movement, including the offset from the tracked dynamic reference array to the patient's origin in the image frame.

$\mathbf{M}_{\text{global}}$ is computed from the difference between the initial and moved positions and orientations. It integrates two key components:

1. **Relative Rotation and Translation**: The global rotation matrix $\mathbf{R}_{\text{global}}$ and translation vector $\mathbf{T}_{\text{global}}$ are derived from comparing the initial and moved orientations and positions. They reflect the net rotational and translational movement of the patient.

2. **Accounting for the Offset**: The offset from the attachment point of the tracked dynamic reference to the patient's origin in the image frame significantly influences the rotations. This offset is crucial for accurate transformation and is incorporated into the global transformation matrix.

The global transformation matrix $\mathbf{M}_{\text{global}}$ is thus defined as:

$$\mathbf{M}_{\text{global}} = \begin{bmatrix} \mathbf{R}_{\text{global}} & \mathbf{T}_{\text{global}} \\ \mathbf{0} & 1 \end{bmatrix}$$

Updating Initial Transformations
Upon computing $\mathbf{M}_{\text{global}}$, the initial transformation matrices $\mathbf{R}_{\text{init}}$ and $\mathbf{T}_{\text{init}}$ are updated to realign the measured movements to the original position:

1. **Updated Rotation Matrix** ($\mathbf{R}_{\text{updated}}$): Achieved by multiplying the inverse of the global rotation matrix with the initial rotation matrix.
2. **Updated Translation Vector** ($\mathbf{T}_{\text{updated}}$): Calculated by rotating the initial translation vector by the inverse of the global rotation matrix and adding the inverse rotated global translation vector.

These updates ensure that the transformations obtained from the registration remain valid when the patient is moved during the procedure.

Implementation in Real-Time Navigation
The updated rotation matrix and translation vector are then used to transform the measured points back to the original reference frame. In order to perform live navigation, an algorithm is used that employs these transformations, depicted below in Algorithm 1.

Algorithm 1: Continuous Update of Transformation Matrices in Live Navigation

Data: Initial transformation matrices ($\mathbf{R}_{\text{procrustes}}$, $\mathbf{T}_{\text{procrustes}}$), Stream of new position and orientation data
Result: Continuously updated $\mathbf{R}$ and $\mathbf{T}$
Initialize with Procrustes-derived matrices
$\mathbf{R}_{\text{current}} \leftarrow \mathbf{R}_{\text{procrustes}}$
$\mathbf{T}_{\text{current}} \leftarrow \mathbf{T}_{\text{procrustes}}$
while *new position and orientation data is available* **do**
  Load new position ($\mathbf{P}_{new}$) *and orientation data* ($\mathbf{O}_{new}$)
  Compute global transformation matrix $\mathbf{M}_{\text{global}}$ *from* $\mathbf{P}_{\text{new}}$ *and* $\mathbf{O}_{\text{new}}$
  Update current rotation and translation matrices
  $\mathbf{R}_{\text{current}}, \mathbf{T}_{\text{current}} \leftarrow \text{update\_R\_T}(\mathbf{R}_{\text{current}}, \mathbf{T}_{\text{current}}, \mathbf{M}_{\text{global}})$
end
return $\mathbf{R}_{current}, \mathbf{T}_{current}$

2.3.4. Transformations in the Dual-Robot System

The previous section explained how the Haply System updates its transformation to enable continuous navigation in dynamic scenarios. However, the approach used in the Haply System does not resemble how conventional navigation systems work. In conventional methods, a continuous transformation mapping the TCP measurements in the local DRF is used, and a single image-to-patient registration matrix is computed.

In the Dual-Robot system, the kinematic models are available, and the transformation between the two bases is known. The system leverages the kinematic models of the robotic manipulators to allow for dynamic sampling in the robot system by continuously transforming the end-effector calculations within a single global frame and sampling the relative distance to the DRF. This method reduces the number of necessary transformations, thereby likely decreasing cumulative errors. By directly attaching the phantom to the end-effector of the KUKA LBR iiwa 7, the system aims to mimic a rigid attachment to the patient, minimizing clinical errors and focusing on navigation system errors.

The transformation between the bases of the KUKA LBR iiwa 14 (iiwa14_base) and the KUKA LBR iiwa 7 (iiwa7_base) is defined and broadcasted using 'tf2_ros'. This transformation is represented as shown in Equation (2.1), where $\mathbf{R}$ is the rotation matrix and $\mathbf{t}$ is the translation vector.

$$\mathbf{T}_{\text{iiwa7\_base}}^{\text{iiwa14\_base}} = \begin{bmatrix} \mathbf{R} & \mathbf{t} \\ 0 & 1 \end{bmatrix} \tag{2.1}$$

Using the joint states of the KUKA LBR iiwa 14, the forward kinematics are computed to determine the pose of its end-effector (iiwa14_end_effector) relative to its base. The forward kinematics map the joint positions to the end-effector pose using methods from the Python Robotics Toolbox.

The end-effector pose of the KUKA LBR iiwa 14 is then transformed into the frame of the KUKA LBR iiwa 7. This transformation uses the previously defined base transformation as shown in Equation (2.2).

$$T_{\text{iiwa14\_end\_effector}}^{\text{iiwa7\_base}} = T_{\text{iiwa7\_base}}^{\text{iiwa14\_base}} \cdot T_{\text{iiwa14\_end\_effector}}^{\text{iiwa14\_base}} \tag{2.2}$$

To determine the pose difference between the end-effectors of the two robots, the transformed pose of the KUKA LBR iiwa 14 end-effector ($T_{\text{iiwa14\_end\_effector}}^{\text{iiwa7\_base}}$) is compared to the pose of the KUKA LBR iiwa 7 end-effector ($T_{\text{iiwa7\_end\_effector}}^{\text{iiwa7\_base}}$). The difference in position and orientation is calculated as shown in Equation (2.3).

$$T_{\text{diff}} = T_{\text{iiwa7\_end\_effector}}^{\text{iiwa7\_base}} \cdot \left(T_{\text{iiwa14\_end\_effector}}^{\text{iiwa7\_base}} \right)^{-1} \tag{2.3}$$

where $\mathbf{T}_{\text{diff}}$ represents the relative transformation from the iiwa 14 end-effector to the iiwa 7 end-effector in the iiwa 7 base frame.

For OptiTrack, as seen in Figure 2.10, the positions of the instrument and patient are provided in the global camera frame, denoted as frame C. The transformation from the camera frame to the skull frame is denoted in Equation (2.4).

$$T_{C_{TCP}}^{C_{\text{DRF}}} = (T_{C_{\text{DRF}}}^{C})^{-1} \cdot T_{C_{TCP}}^{C} \tag{2.4}$$

In Equation (2.4), $(T_{C_{\text{DRF}}}^{C})^{-1}$ is the inverse of the skull pose matrix, effectively transforming the global camera frame into the skull frame. When this is multiplied by the probe pose matrix, the resulting matrix $T_{C_{TCP}}^{C_{\text{DRF}}}$ provides the probe pose relative to the skull frame.

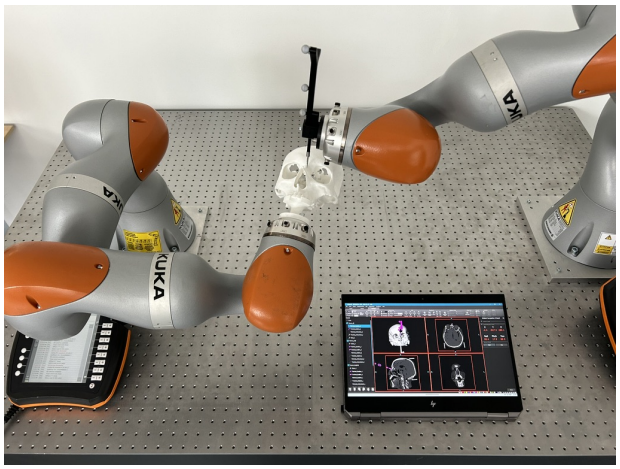

Figure 2.11: Real-time navigation using the two robotic manipulators. The subject and instrument are tracked mechanically, and the connection is made through ROS over UDP to 3DMedX for visualization.

These transformations enable both OptiTrack and the two KUKA robots to sample in the dynamic reference frame. Samples can be gathered and fed to the registration algorithm outlined in Section 2.4. By continuously applying the obtained transformations to the TCP calculations from both systems, continuous navigation and real-time visualization in the imaging data are achieved, as shown in Figure 2.11.

2.4. Image-to-Patient Registration

To accurately locate the tool center point (TCP) of a surgical probe in the image frame, a transformation matrix must be computed by the surgical robotic navigation system. This process of aligning the image frame with the patient in the operating theater is known as registration. Various methods can achieve this alignment, including surface-based matching through Iterative Closest Point, point-based registration using least-squares optimization, contour matching with computer vision techniques, and hybrid methods that combine these approaches [29]. The choice of technique depends on clinical factors such as the anatomical area of interest and the level of invasiveness. For instance, non-invasive methods like using a dental splint may not require additional procedures or imaging, whereas invasive methods like screw registration fiducials require both [1] [30] [29].

Point-based registration using invasive fiducials is often proven to be the most accurate [29] [31]. The point-based registration method proposed by Arun et al. was selected for both systems due to its proven effectiveness [32]. Arun's method is optimal for least-squares fitting under the assumption of isotropic noise and exact correspondences. This approach is often optimal for rigid body transformations [32].

To achieve the registration process in both the radiographic image and on the patient in the operating room, a corresponding set of fiducial markers need to be established as illustrated in Figure 2.12.

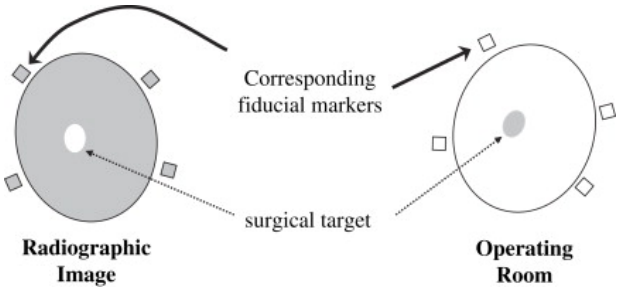

Figure 2.12: Illustration of fiducial markers in the radiographic image and the operating room. Adapted from [33].

The registration algorithm, detailed in Algorithm 2 computes an optimal transformation between two sets of corresponding points by using Singular Value Decomposition (SVD). This method finds the optimal rotation and translation that align the points by minimizing the sum of squared distances between the matched points, assuming exact correspondences. The effect of the algorithm is visualized in Figure 2.13.

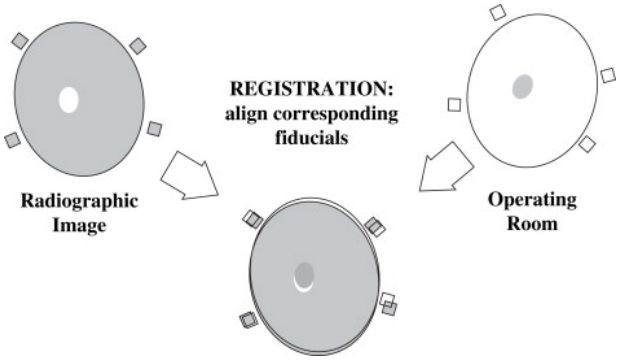

Figure 2.13: Illustration of the registration process aligning the corresponding fiducials. Adapted from [33].

Various types of errors can occur in this process, such as inaccuracies in locating fiducials in both the image and the operating room, known as Fiducial Localization Error (FLE). To evaluate the performance of the navigation system, it was essential to minimize external sources of error that could degrade registration performance. Therefore, registration fiducials were printed directly on the phantom skull, allowing their positions to be extracted from the 3D modeling software, thereby minimizing localization errors in the image frame. The only remaining error is the 3D printer's printing error, which is smaller than the cumulative FLE and imaging errors from CT scans and the localization process. Although the localization process during registration still influences FLE, it is significantly reduced.

The phantom was equipped with a total of 12 fiducials (see Figure 2.14), distributed around the entire skull. The SciKit-Surgery Python library's implementation of the least-squares algorithm from Arun et al. [32] was used for point-based registration, as detailed in Algorithm 2.

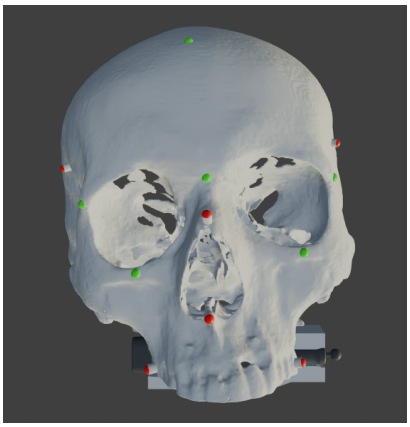

Figure 2.14: STL model of the skull with red registration fiducials and green target fiducials.

Figure 2.14 shows the following anatomical landmarks used as registration fiducials (in red) and target fiducials (in green):

Registration fiducials (red):

- Nasal bone
- Anterior nasal spine
- First molar on the left (16)
- First molar on the right (26)
- Temporal bone on the left
- Temporal bone on the right

Target fiducials (green):

- Midline os frontale
- Glabella
- Left lateral orbital rim
- Right lateral orbital rim
- Left inferior orbital rim
- Right inferior orbital rim

The number and distribution of registration fiducials around the target area significantly impact registration accuracy [34]. In this research, six registration and six target fiducials were evenly distributed around the skull to ensure comprehensive coverage. Increasing the number of registration fiducials around a small target area can reduce the registration error due to a higher density of reference points for accurate alignment. However, this approach does not provide a comprehensive evaluation of the system's performance across the entire workspace. When fiducials are spread out over a larger area, including regions further from the target, a better assessment of the navigation system's overall accuracy and robustness across the entire operational field is achieved. In this study, the registration and target fiducials were located around the entire skull, providing an indication of registration performance across the surgical workspace rather than in a confined area. This setup offers a more generalized assessment applicable to various procedures, giving a more realistic indication of the navigation system's performance around the 3D-printed phantom skull.

Algorithm 2: Orthogonal Procrustes Method for Point-Based Registration [32]

Data: Fixed point set $\mathbf{P}'$ (registration fiducials), Moving point set $\mathbf{P}$ (measured points)
Result: Rotation matrix $\mathbf{R}$, Translation vector $\mathbf{T}$, Fiducial Registration Error (FRE)
Validate inputs
Initialize rotation and translation; $\mathbf{R} \leftarrow \mathbf{I}_3$
$\mathbf{T} \leftarrow \mathbf{0}_{3\times 1}$
Compute centroids of the point sets (Arun Eq. 4 and 6); $\mathbf{p} \leftarrow \text{mean}(\mathbf{P}, \text{axis} = 0)$
$\mathbf{p}' \leftarrow \text{mean}(\mathbf{P}', \text{axis} = 0)$
Center the point sets (Arun Eq. 7 and 8); $\mathbf{Q} \leftarrow \mathbf{P} - \mathbf{p}$
$\mathbf{Q}' \leftarrow \mathbf{P}' - \mathbf{p}'$
Compute cross-covariance matrix (Arun Eq. 11); $\mathbf{H} \leftarrow \mathbf{Q}^T\mathbf{Q}'$
Compute SVD of cross-covariance matrix (Arun Eq. 12); $[\mathbf{U}, \mathbf{S}, \mathbf{V}^T] \leftarrow \text{SVD}(\mathbf{H})$
Correct SVD components to avoid reflection (Fitzpatrick's modification); $\mathbf{X} \leftarrow$ _fitzpatricks_X($[\mathbf{U}, \mathbf{S}, \mathbf{V}^T]$)
if *det*$(\mathbf{X}) < 0$ **then**
  Handle the case where determinant of $\mathbf{X}$ *is negative*
end
Compute rotation matrix; $\mathbf{R} \leftarrow \mathbf{X}$
Compute translation vector; $\mathbf{T} \leftarrow \mathbf{p}'^T - \mathbf{R}\mathbf{p}^T$
Compute Fiducial Registration Error; FRE $\leftarrow$ compute_fre($\mathbf{P}', \mathbf{P}, \mathbf{R}, \mathbf{T}$)
return $\mathbf{R}$, $\mathbf{T}$, *FRE*

2.5. Robot Control

The controller utilizes a feedback control approach combined with a dynamic model of the robot to achieve desired end-effector behavior in Cartesian space. Impedance control is a widely used technique for robot manipulators, allowing for the regulation of both position and force/torque at the end-effector [35]. This is particularly beneficial for tasks requiring interaction with the environment or human collaboration, such as in cases with surgical human robot interaction. Cartesian impedance control specifically focuses on achieving desired impedances in Cartesian space, which simplifies the control design and allows for intuitive interaction.

Mathematical Formulation:
The Cartesian impedance controller presented here utilizes the following control law:

$$\tau = J^T\left(-Ke - D\dot{e}\right) + \tau_{nullspace} + \tau_{ext} \tag{2.5}$$

where:

- τ is the vector of joint torques
- J is the geometric Jacobian matrix of the end-effector
- K is the stiffness matrix
- D is the damping matrix
- e is the Cartesian pose error
- $\dot{e}$ is the derivative of the pose error
- $\tau_{nullspace}$ is the torque contribution from nullspace control
- τ_{ext} is the torque contribution from external forces (e.g., assistance)

The pose error e is calculated as the difference between the desired end-effector pose and the actual pose, expressed in the base frame. The nullspace control term $\tau_{nullspace}$ utilizes the nullspace of the Jacobian to achieve additional objectives, such as joint configuration optimization, without affecting the Cartesian impedance control.

The controller is implemented as a ROS package, utilizing the controller interface and hardware interface frameworks. The robot's URDF model is parsed to obtain the kinematic chain and calculate the Jacobian matrix. Since the offset of the probe is included in the URDF model, the Cartesian controller allows for precise adjustment of the tool tip. Dynamic Reconfigure is used to adjust the stiffness and damping matrices online, along with other parameters such as nullspace control gains and assistance settings. An action server allows for sending Cartesian trajectory goals to the controller. For registration the initial purpose is to carefully point to different fiducials on

the target phantom. Here, to achieve this, the Cartesian stiffness could be set to zero using Dynamic Reconfigure. By setting the stiffness matrix K to zero, the robot can be moved freely in Cartesian space with minimal resistance using the internal gravity compensation methods provided by the KUKA iiwa driver ROS node.

2.6. Multi-Sensor Data Fusion

A surgical robotic navigation system requires to be accurate consistently throughout the procedure. When individual sensors fall short, for example due to a blocked line-of-sight in optical tracking, integrating multiple sensors through data fusion methods might be beneficial. By combining multiple sensor inputs, sensor fusion potentially provides a more accurate and robust state estimate [36] [37]. This integration can surpass the individual accuracy and reliability of each sensor, making it a logical choice for enhancing surgical robotic navigation systems, where accuracy and system reliability are important.

Various methods exist for fusing multiple sensors, with the objective of estimating the next state of a tracked object [38]. In all cases, the sensor fusion method necessitates a mathematical model to link measurements to state transitions. While this can be highly simplified, effective results can still be achieved by considering the noise properties of the system [39]. Generally, the requirements are similar: sensors should either provide additional or redundant information for state estimation, be spatially aligned, and be time-synchronized. For instance, in tracking a patient's movements in six degrees of freedom, position and orientation data from different sensors can be combined into a single state estimation. Alternatively, two sensors providing the same position estimate can be integrated into a sensor fusion model, resulting in a more robust and accurate state estimation. In the Haply System, redundant sensor information is present in both the patient and instrument tracking system. The patient is tracked by both the Haply and OptiTrack systems, while the instrument is tracked by the KUKA robot joint encoders through forward kinematics, as well as the OptiTrack system. Two different sensor fusion models have been implemented to create a fused estimation of both the patient orientation and the probe state, as illustrated in Figure 2.9.

The patient tracking systems, Haply Inverse3 and OptiTrack, do not track the exact same position because the Dynamic Reference Frame (DRF) and the attachment of the Haply device are at different positions on the skull. Therefore, for effective 6DOF patient state fusion, a transformation is required to ensure that both measurements represent the same tracked reference on the skull. However, this transformation was not feasible since the Haply device lacks an open kinematic model, and the exact measurement point at the end-effector is unclear. Despite this, the VerseGrip IMU and the orientation estimates from OptiTrack were consistent when both were initialized to zero orientation. From this starting pose, relative orientation could be accurately measured. Therefore, in the patient estimation model, only the orientation measurements were fused.

2.6.1. Kalman Filter Sensor Fusion for Surgical Instrument State Estimation

The TCP of the instrument is redundantly tracked through the forward kinematics of the robotic manipulator and the OptiTrack system. In sensor fusion, numerous methods exist for fusing redundant sensor information, dependent on the application, available data, models of the tracked object or sensors, computational complexity of the method, and the sensors' noise characteristics [37]. Initially, the noise characteristics of both the KUKA and the OptiTrack systems were examined and compared. With the tool's position stabilized, data was recorded through ROS, under the assumption that the probe is stationary. The gathered position estimates from the KUKA and OptiTrack systems are shown in Figure 2.15.

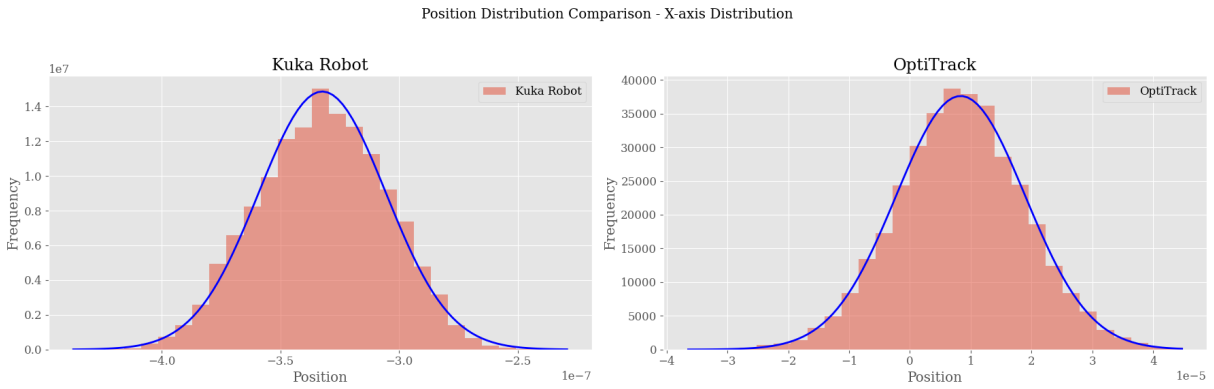

Figure 2.15: Noise distribution of the KUKA and OptiTrack systems along the x-axis.

The error distribution for both the KUKA and the OptiTrack systems exhibited Gaussian-like noise. The OptiTrack samples at a rate of 240 Hz, while the robot is set to a control rate of 500 Hz. Considering the impedance control directed by unpredictably applied forces at various parts, and the increased complexity in implementing a model for the instrument tracking system, a simple constant velocity model was employed. Given these characteristics, and the need for real-time sensor fusion with minimal delays, a Kalman Filter approach was deemed a reasonable choice. The Kalman Filter is an optimal sensor fusion algorithm under the assumption of Gaussian distributed noise and a linear state transition function, it is highly computationally efficient and proved to be effective in many applied robotics cases [37] [40] [41].

The Kalman Filter operates in two main steps: prediction and update. In the prediction step, the filter projects the current state estimate forward in time. In the update step, the filter adjusts the projected estimate by incorporating the new measurements.

Mathematical Explanation of the Kalman Filter
The state of the system is represented by the state vector $\mathbf{x}_k$, and the state transition model is given by:

$$\mathbf{x}_k = \mathbf{A}\mathbf{x}_{k-1} + \mathbf{B}\mathbf{u}_k + \mathbf{w}_k \tag{2.6}$$

where $\mathbf{A}$ is the state transition matrix, $\mathbf{B}$ is the control input matrix, $\mathbf{u}_k$ is the control input, and $\mathbf{w}_k$ is the process noise, assumed to be Gaussian with covariance matrix $\mathbf{Q}$.

The measurement model is given by:

$$\mathbf{z}_k = \mathbf{H}\mathbf{x}_k + \mathbf{v}_k \tag{2.7}$$

where $\mathbf{H}$ is the measurement matrix, and $\mathbf{v}_k$ is the measurement noise, assumed to be Gaussian with covariance matrix $\mathbf{R}$.

Prediction Step
The predicted state estimate $\hat{\mathbf{x}}_{k|k-1}$ and the predicted estimate covariance $\mathbf{P}_{k|k-1}$ are calculated as:

$$\hat{\mathbf{x}}_{k|k-1} = \mathbf{A}\hat{\mathbf{x}}_{k-1|k-1} + \mathbf{B}\mathbf{u}_k \tag{2.8}$$

$$\mathbf{P}_{k|k-1} = \mathbf{A}\mathbf{P}_{k-1|k-1}\mathbf{A}^\top + \mathbf{Q} \tag{2.9}$$

Update Step
When a new measurement $\mathbf{z}_k$ is received, the Kalman gain $\mathbf{K}_k$ is computed as:

$$\mathbf{K}_k = \mathbf{P}_{k|k-1}\mathbf{H}^\top(\mathbf{H}\mathbf{P}_{k|k-1}\mathbf{H}^\top + \mathbf{R})^{-1} \tag{2.10}$$

The updated state estimate $\hat{\mathbf{x}}_{k|k}$ and the updated estimate covariance $\mathbf{P}_{k|k}$ are then given by:

$$\hat{\mathbf{x}}_{k|k} = \hat{\mathbf{x}}_{k|k-1} + \mathbf{K}_k(\mathbf{z}_k - \mathbf{H}\hat{\mathbf{x}}_{k|k-1}) \tag{2.11}$$

$$\mathbf{P}_{k|k} = (\mathbf{I} - \mathbf{K}_k\mathbf{H})\mathbf{P}_{k|k-1} \tag{2.12}$$

Process Noise and Measurement Noise
The process noise covariance matrix **Q** and the measurement noise covariance matrix **R** play crucial roles in the performance of the Kalman Filter. The process noise covariance matrix **Q** represents the uncertainty in the system model, while the measurement noise covariance matrix **R** represents the uncertainty in the measurements. These matrices influence how much the filter relies on the model predictions versus the actual measurements. A larger **Q** indicates more trust in the measurements, while a larger **R** indicates more trust in the model predictions.

In this implementation, the state dimensions include both position and velocity, resulting in a 6-dimensional state vector $\mathbf{x} = [x, y, z, vx, vy, vz]^\top$. The measurement vector includes positions from both the robot and OptiTrack, as well as the velocity from the robot, resulting in a 9-dimensional measurement vector. The measurement noise has been initially tuned to resemble the noise characteristics from the KUKA robot and OptiTrack system as depicted in Figure 2.15.

Effective sensor fusion requires the measurements to be time-synchronized. Additionally, data from the sensors must be spatially aligned. The sensor fusion model incorporated position measurements from OptiTrack and position and velocity measurements of the same TCP from the robot. To achieve this, a data synchronization algorithm was initially employed, using the ApproximateTimeSynchronizer from the ROS message filters package to align the measurements from the robot and OptiTrack in time [42]. When a time-synchronized message is received, the model extracts the position from the VRPN client node of OptiTrack, and computes the end-effector position and velocity through forward kinematics. The end-effector velocity is obtained through:

$$\mathbf{v}_{ee} = \mathbf{J}(\mathbf{q}) \cdot \dot{\mathbf{q}} \tag{2.13}$$

The computed end-effector positions and velocities, and OptiTrack received positions are spatially aligned and published to a new topic. The algorithm is depicted in Algorithm 3.

Algorithm 3: Data Synchronization and Velocity Computation

Data: Joint states stream **q**, VRPN Pose stream **V**
Result: Synchronized Data with Relative Positions and End-Effector Velocity
Initialize robot and VRPN models
Initialize subscribers for joint states and VRPN pose
Initialize publisher for synchronized data
Define synchronization callback function
Setup Time Synchronizer with appropriate parameters
On receiving synchronized data (callback function): **begin**
    Extract positions from Joint States and VRPN Pose
    robot_position ← get_cartesian_position(**q**)
    vrpn_position ← extract_vrpn_position(**V**)
    Transform VRPN coordinates to robot's frame
    transformed_vrpn_position ← transform_coordinates(**vrpn_position**)
    Compute relative positions
    relative_robot_position, **relative_vrpn_position** ←
     compute_relative_positions(**robot_position**, **transformed_vrpn_position**)
    Compute end-effector velocity
    end_effector_velocity ← compute_end_effector_velocity(**q**)
    Publish synchronized data
    publish_synchronized_data(relative_robot_position, relative_vrpn_position, end_effector_velocity)
end

After data synchronization, the Kalman filter predict - update cycle is implemented through a FilterPy Kalman Filter implementation shown in Algorithm 4:

Algorithm 4: Position and Velocity Data Fusion using Kalman Filter

Data: Synchronized robot data including position and velocity.
Result: Fused position and velocity estimation.
State dimensions (position + velocity) $dim_x \leftarrow 6$ // x, y, z, vx, vy, vz
Measurement dimensions (positions + velocity) $dim_z \leftarrow 9$ `// robot position, optitrack position, robot velocity`
Initialize the Kalman Filter with dimensions dim_x *and* dim_z
Initialize state vector $\mathbf{x} \leftarrow \mathbf{0}_{dim_x}$
State transition matrix (constant velocity model)
Measurement matrix $\mathbf{H} \leftarrow \mathbf{0}_{dim_z \times dim_x}$ with appropriate identity blocks
Measurement noise covariance $\mathbf{R} \leftarrow$ block diagonal with sensor noise variances
Process noise covariance $\mathbf{Q} \leftarrow \mathbf{I}_{dim_x} \times 0.1$
while *true* **do**
    Receive new synchronized robot data message
    Extract position and velocity data from message
    Combine measurements to form a single vector
    Perform Kalman Filter predict step
    Perform Kalman Filter update step with combined measurements
    Publish fused position and velocity data
end

2.6.2. Sensor Fusion for Patient State Estimation

The OptiTrack system, through its data streaming options, provides updates on the orientation and position of both the end-effector and the tracked phantom at a maximum rate of 240 Hz. Orientation data is provided in quaternions. Similarly, the Haply VerseGrip offers orientation estimates in quaternions at 200Hz. As Kalman Filters are not able to handle non-linear relations such as quaternions well, an Unscented Kalman Filter was chosen to manage the non-linear quaternion relationships [37] [43].

The primary difference between the standard Kalman Filter and the Unscented Kalman Filter lies in how they handle non-linear transformations of the state and measurement vectors. In the standard Kalman Filter, linear approximations are made through the use of Jacobian matrices in both the prediction and update steps. This can be problematic when dealing with highly non-linear systems, as the linear approximation may not be accurate enough.

The Unscented Kalman Filter, on the other hand, uses a deterministic sampling technique known as the Unscented Transform to handle non-linear transformations [44]. This involves the generation of a set of sample points, called sigma points, which capture the mean and covariance of the state distribution. These sigma points are then propagated through the non-linear functions, and the resulting transformed points are used to compute the predicted mean and covariance. The FilterPy Unscented Kalman Filter is used and the implementation of this algorithm can be found in Algorithm 5.

Algorithm 5: Unscented Kalman Filter (UKF) for Orientation Fusion

Data: Initial state estimate $\mathbf{x}$, process noise covariance $\mathbf{Q}$, measurement noise covariance $\mathbf{R}$, synchronized orientation data.
Result: Updated state estimate $\hat{\mathbf{x}}$ and covariance estimate $\mathbf{P}$
State dimension $n \leftarrow 4$
Measurement dimension $m \leftarrow 4 \times 2$ `// Two quaternion measurements`
Initialize state vector $\mathbf{x}$ `// State vector:` $[q_0, q_1, q_2, q_3]^T$
Initialize measurement vector $\mathbf{z}$ `// Measurement vector: Concatenation of quaternions from two sensors`
Process noise covariance $\mathbf{Q} \leftarrow n \times n$ diagonal matrix with 0.1 on the diagonals
Measurement noise covariance $\mathbf{R} \leftarrow m \times m$ block diagonal matrix with sensor variances
while *true* **do**
    Wait for new synchronized data message
    Extract quaternion data from message to form $\mathbf{z}$
    Perform UKF prediction
    Perform UKF update with $\mathbf{z}$
    Extract updated state from UKF
    Publish fused orientation
end

2.7. Performance Evaluation

All components and methods utilized in a surgical robotic navigation system can influence performance and thereby overall accuracy. As indicated by the systematic review in Appendix A, many articles fail to address critical components contributing to the system's overall performance. Surgical robotic navigation systems consists out of multiple components and software components to realize the transformation from the robotic end-effector to the patients imaging data and preoperative plan. To understand the total performance of a surgical robotic navigation system, it is fundamentally important to assess individual components and acknowledge different sources of error. According to Widmann et al., in image-guided surgery, major errors can be categorized as technical error, imaging error, registration error, application error, and human error [45]. These errors are not independent but integrative, collectively affecting the accuracy of image-guided surgery.

Technical error refers to the inherent hardware and software inaccuracies in the position measurement of the surgical navigation system. Imaging error is the inaccuracy of the imaging modality in accurately depicting anatomical structures. Registration error is the inaccuracy in linking image data to the patient's position in the operating room. Application error refers to the discrepancy between the actual position of the navigated surgical tool during the procedure and the real position of the surgical target, encompassing the registration error and additional factors. This error also reflects the accuracy of the achieved surgical result compared to the initial plan. Human error contributes to and compounds all these error types [45].

Depending on the type of research, different requirements can be set for the performance reporting of a surgical robotic navigation system. To systematically assess the proposed systems from this research, it is suggested to decompose performance into the technical accuracy of the individual components, registration accuracy in a static context, and registration accuracy in dynamic situations. In basic clinical research, where cadaverous experiments are conducted, or at more advanced levels where actual clinical experiments are performed, it is highly insightful to compare the registration accuracy *in vivo* against an *ex-vivo* baseline. This comparison reflects how much the system influences performance.

Technical Accuracy Assessment

Technical accuracy can be interpreted at different levels within the system. For instance, the technical accuracy can refer to the individual 3D accuracy of each OptiTrack camera, as presented in the system specifications in Section 2.1. However, this does not necessarily reflect the technical accuracy of the OptiTrack system as a whole. The extent to which the entire camera system can accurately map distances can be viewed as the technical accuracy of the system. This demonstrates what is maximally achievable with the used kinematic model of the robotic manipulator or calibration setup of OptiTrack. To evaluate this, measurements can be taken against an object with a known spatial reference. The Euclidean distance can be calculated using Equation (2.14), and the individual error can be computed by comparing the measured distance against the ground truth using Equation (2.15).

$$d_{AB} = \sqrt{(x_B - x_A)^2 + (y_B - y_A)^2 + (z_B - z_A)^2} \tag{2.14}$$

The accuracy of the measurements can be determined by comparing the computed distances with the actual distances. The error is defined as:

$$e_{XY} = |d_{XY}^{\text{(ground-truth)}} - d_{XY}^{\text{(measured)}}| \tag{2.15}$$

Registration Accuracy Assessment

The registration algorithm computes the transformation to map the patient in the operating room to the preoperative imaging data. This process is known to introduce significant errors that can impact overall performance [34, 46, 45]. Errors in the registration process are categorized as Fiducial Localization Error (FLE) as indicated in Section 2.4, Fiducial Registration Error (FRE), and Target Registration Error (TRE), which are visually explained in Figure 2.16. To evaluate the effectiveness of the registration and in-vitro navigation, one should compare the registration error against known values, referred to as the Target Registration Error (TRE). The Fiducial Registration Error (FRE) is the difference between the measured target and the registration target, which is uncorrelated with the TRE and a less relevant metric [47].

After employing the Procrustes algorithm, which provides the rotation matrix R and translation vector T that transform measured points to the image space, as explained in Section 2.4, the target measurements are converted to the image frame as follows:

$$\mathbf{P}_{\text{image}} = \mathbf{R} \cdot \mathbf{P}_{\text{instrument}} + \mathbf{T} \tag{2.16}$$

where $\mathbf{P}_{\text{image}}$ represents the point transformed into the image frame, $\mathbf{R}$ is the rotation matrix, $\mathbf{P}_{\text{instrument}}$ is the position vector of the point in the instrument's frame (from the robot, OptiTrack, or fused system), and $\mathbf{T}$ is the translation vector.

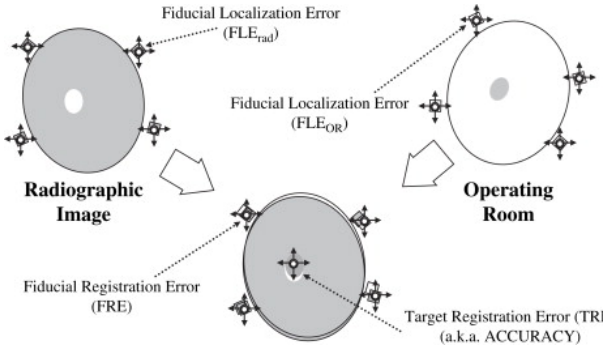

Figure 2.16: Visualization of different errors in point-based registration. Fiducial Localization Error (FLE) occurs during the localization of the registration fiducials in the imaging dataset. Fiducial Registration Error (FRE) occurs when aligning the fiducials in the operating room with the registration fiducials. Target Registration Error (TRE) is the difference between the target on the patient in image space and the measurement by the instrument at which the algorithm is not trained. Adapted from [33].

The TRE is calculated as the Euclidean distance between the transformed point and the known target point in the image frame:

$$\text{TRE} = \|\mathbf{P}_{\text{image}} - \mathbf{P}_{\text{target}}\| \tag{2.17}$$

where $\mathbf{P}_{\text{target}}$ is the position vector of the known target point in the image frame.

Algorithm 2 computes the Fiducial Registration Error (FRE) and the transformation. The FRE quantifies the discrepancy between the known registration targets and the registration fiducial measurements transformed into the image frame [48]. The FRE is uncorrelated with the Target Registration Error (TRE), as illustrated in Figure 2.17. TRE measures the error at target points not used in the registration process [47].

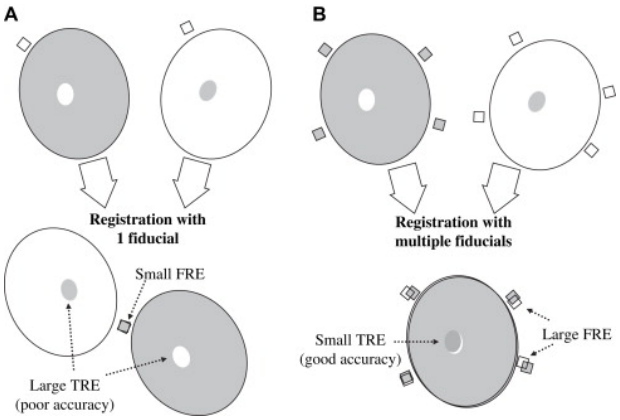

Figure 2.17: Comparison of TRE and FRE. (A) Registration with a single fiducial shows a small FRE but a large TRE, indicating poor accuracy. (B) Registration with multiple fiducials shows a larger FRE but a much smaller TRE, indicating better accuracy. This demonstrates that a high FRE does not correlate to a high TRE. Adapted from [33].

Evaluation

After individually assessing different components and the overall system accuracy, the gathered results should be presented properly. If the distribution of the results does not resemble a normal distribution, the mean and standard deviation might not provide a holistic picture of the performance. To check the normality condition, the Shapiro-Wilk test can be employed. The Shapiro-Wilk test assesses whether a dataset is normally distributed by comparing the order statistics of the sample to those expected under a normal distribution, providing insightful information about the data distribution [49]. In the case of a non-normally distributed surgical robotic system that consistently performs around 1 mm but has a few outliers at 5 mm, the mean and standard deviation might not fully capture the performance characteristics. These outliers, however, are clinically significant as they may indicate potential severe performance issues. Outliers in the *in-vitro* evaluation provide critical insight into how the system might perform in clinical scenarios, where the source of errors can be more ambiguous due to various clinical factors. Therefore, the entire range, mean, median, and standard deviation of the results when evaluating the navigation performance should be presented.

3

Experiments and Results

This chapter outlines the experimental design and presents the results. In Section 3.1 the design of the four different sets of experiments are outlined where in 3.2 all corresponding results are given.

3.1. Experiment Design

As discussed in Section 2.7, there are various sources of error in a surgical robotic navigation system. A key aspect is that the registration algorithm introduces significant uncertainty to the navigation system, making it unclear whether the total error originates from the registration method or the technical accuracy of the tracking system. Moreover, performing rigid registration and evaluation on a target phantom does not reflect the system's capabilities in dynamic scenarios, which are more likely in clinical environments where the patient is often not fixated to the operating table. To understand the different sources of error, the experiments are designed to gradually include more sources of error: starting with technical accuracy, then incorporating registration error, and finally evaluating the registration error in dynamic configurations.

3.1.1. Experiments 1: Technical Accuracy

The first experiment is designed to provide an overview of the technical accuracy of the separate components. The technical accuracy in the surgical robotic navigation system refers to the inherent soft- and hardware errors in position measurement [45]. For robotic manipulators, it includes the errors from the encoder sensor readings, errors deviating in the kinematic model, and errors in the tool definition within the robotic model. The technical errors in optical tracking systems include inaccuracies in optical triangulation due to factors such as thermal noise causing jitter, angle-dependent errors when the tracking elements are not optimally aligned, and the need for careful calibration and correct placement of tracking elements to minimize errors. Additionally, the system's accuracy can be compromised by incorrect positioning of the dynamic reference frame (DRF) [45]. This all comes together in positioning error, to evaluate this the measured Euclidean distance across specified movements and comparing the measured distance against the known ground truth. This provides an indication of the absolute accuracy of the systems, with the calculated error showing how well the systems align with the real-world dimensions they are supposed to measure.

To assess the technical accuracy of the robotic manipulator, the Digitizer Probe was mounted on the KUKA LBR iiwa 14 robot, 3.1 with the dimensions of the tool added to the Unified Robot Description Format (URDF). The instrument was simultaneously tracked by the OptiTrack system. The Kalman Filter and data synchronizer module (see Section 2.6) synchronize the relative displacements of the OptiTrack and KUKA tool measurements, which are then separately recorded as another tracking modality alongside the robotic manipulator and OptiTrack. The robots were manually navigated using gravity compensation control (see Section 2.5) across predefined slots on the OptiTrack Calibration Block.

Due to intellectual property protections, the Haply firmware imposes restrictions, including a closed kinematic model that is inaccessible. Furthermore, the Haply end-effector, designed to accommodate a VerseGrip IMU handle, features a ball socket construction, tracking the center position of the sphere held within the end-effector. These constraints necessitated the design of a validation fixture for Haply to facilitate accuracy measurements comparable to those of the OptiTrack and KUKA robots, as illustrated in Figure 3.2.

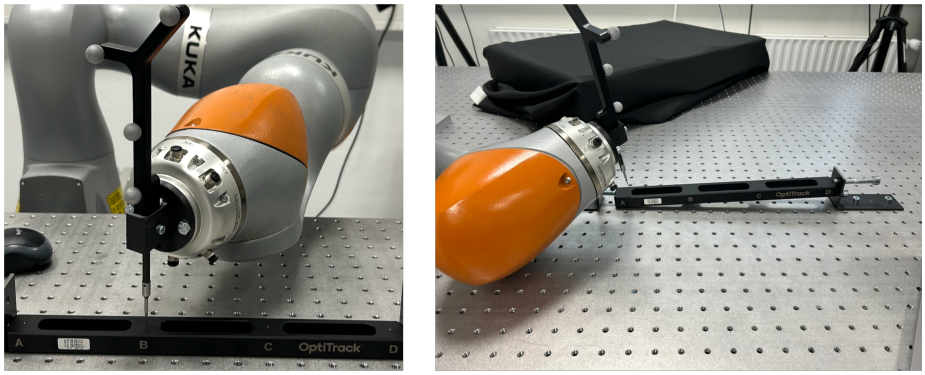

Figure 3.1: KUKA robotic manipulator on the calibration block in different orientations.

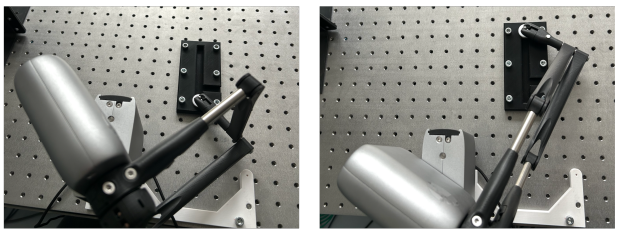

Figure 3.2: 3D-printed validation fixture to assess the technical accuracy of the Haply Inverse3. The fixture consists of a sliding mechanism with a ball on top, which fits into the Haply's socket.

This experiment aims to demonstrate the highest achievable accuracy of the individual components with the active kinematic models and calibration settings, excluding large factors like registration inaccuracies. By providing a controlled environment, it reveals the technical limits of each component and how well their internal kinematic models or triangulation align with the ground truth, offering insights for further system improvement. The results are presented in Section 3.2.1.

3.1.2. Experiments 2: Registration Accuracy

To assess registration accuracy, the target skull is securely clamped to the table, as depicted in Figure 3.3. In this experiment, patient tracking is disregarded, and only fixed registration is evaluated using the KUKA iiwa 14, the OptiTrack system, and these sensors in fusion. Before recording the registration and target fiducials, the sensor fusion system is initialized by aligning the frames of the OptiTrack and KUKA LBR iiwa 14 robots and synchronizing their measurements. The relative movements are then fed into the sensor fusion model as described in Section 2.6. Gravity compensation is used as detailed in Section 2.5 to manually navigate the KUKA LBR iiwa 14, equipped with the surgical instrument, to all six registration fiducials, followed by the target fiducials. The fiducial sets, captured by the robot, OptiTrack, and estimated by the sensor fusion model, are represented in their respective frames. During the experiments, the Haply and OptiTrack systems were attached to monitor and verify the absence of any minor perturbations in the movement of the skull.

The orthogonal Procrustes algorithm, described in Section 2.4, is employed to determine the transformations from the frame of the localization method to the image frame. The TRE is calculated for each target anatomical landmark, with the mean, standard deviation, median, range, and boxplot presented in Section 3.2.2.

3.1.3. Experiments 3: Dynamic Registration Accuracy in the Haply System

In many surgical disciplines, there is a need to reposition the patient or targeted anatomy during surgical navigation. As shown in Figure 2.2, a head mount was developed to simulate the movement of the head relative to the neck. Tracking the patient while continuously updating the registration may introduce additional inaccuracies into the surgical robotic navigation system. Different tracking methods and systems can impact the overall accuracy in various ways. This series of experiments aimed to evaluate the TRE after certain patient movements. Prior to the experiment, all components were activated, including tracking the probe with the OptiTrack, robot, and fused sensor systems, while the patient's position is tracked by the OptiTrack system using the attached reference array, along with the Haply system and orientation fusion.

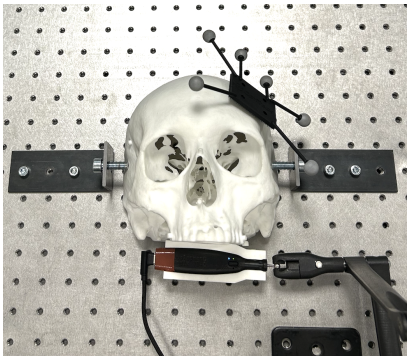

Figure 3.3: The 3D-printed phantom skull rigidly clamped to the table for the registration accuracy experiment in a controlled environment. The Dynamic Reference Frame (DRF) tracked by OptiTrack and Haply Inverse3 is attached to the phantom.

Initially, the phantom is rigidly fixed in its starting position and orientation (see Figure 3.4). All registration fiducials, followed by all target fiducials, are recorded. The phantom is then moved to a new pose, and all target fiducials are recorded again. The updated transformation from the initial registration is determined, allowing for the calculation of the TRE at the moved location. This process yields both an initial TRE and a moved TRE based on a single initial registration using the tracking information obtained from the patient tracking devices. After recording the targets at the moved position, the phantom is returned to the initial position, and the process is repeated.

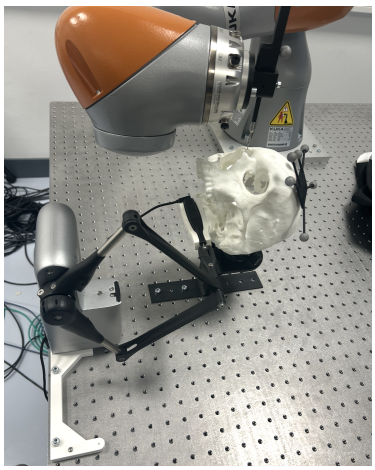

Figure 3.4: Robot with tracked surgical instrument located at nasal bone registration fiducial on the skull phantom in fixed starting orientation.

Simulated movements included lateral bending, neck flexion, and rotation, corresponding to rotation around the z-, x-, and y-axis, respectively (see Figure 2.2). This resulted in six different movements, indicated as P, Q, R, S, T, and U. Each movement involved registering fiducials, recording target points, subsequent movement, and a second recording of target points. In total, 12 target fiducials and six registration fiducials were recorded, including the positional information of the trackers for each movement. For each movement and tracking system, the TRE is computed according to the equation described in Section 2.7. As the Haply system consists of two subsystems, combinations were analyzed using the Haply IMU and end-effector separately. The results are summarized in Table 3.6.

3.1.4. Experiments 4: Dynamic Registration Accuracy in the Dual-Robot System

The final set of experiments evaluated the dynamic registration accuracy in the Dual-Robot system. The phantom was attached to the KUKA iiwa 7 robot, which was controlled with low stiffness using impedance control, allowing for controlled elasticity and mimicking natural movement. The robotic manipulator holding the target was initialized to a reference point with very low stiffness, ensuring high flexibility. The second robotic manipulator, equipped with a tracked probe, moved to the registration and target points via gravity compensation control (impedance

control with zero stiffness), enabling accurate tracking and recording of the target points. The OptiTrack system was active, tracking the DRF on the phantom and the instrument attached to the KUKA. After recording all points in the patient tracker frame, the registration algorithm was executed, and the TRE was calculated according to the equations described in Section 2.7. After sampling the registration and target fiducials, the Fiducial Registration Error (FRE) and Target Registration Error (TRE) were directly evaluated. Recordings with abnormally high FRE and TRE values, exceeding far above 1 mm, indicated a failed registration and were subsequently rejected.

3.2. Results

The results of all four experiments are presented in the tables and figures below. Normality was assessed using the Shapiro-Wilk test, which indicated that the data did not follow a normal distribution. Consequently, the mean, standard deviation, median, and range are reported for all outcomes. Additionally, boxplots are provided to offer a visual representation of the data distribution and variability. Each boxplot illustrates the middle 50% of the error values, extending from the first quartile (Q1, 25th percentile) to the third quartile (Q3, 75th percentile). The line inside each box marks the median error value, indicating the central tendency. Whiskers extend from the box to the maximum and minimum values that are not outliers, providing a visual representation of the data spread. Outliers are shown as separate circles.

3.2.1. Results Experiments Technical Accuracy

In experiment 1, the technical accuracy of the KUKA LBR iiwa 14, OptiTrack optical tracking system, and Haply Inverse3 was evaluated over spatial distances. Two different sets of experiments were conducted due to the design requirements of the Haply, and the results are presented separately below in Experiments 1a and 1b.

Experiment 1a

A total of 90 movements were recorded by the three modalities on the OptiTrack calibration block, resulting in 270 measurements. Among these, 18 movements (20%) the fusion method performed the best.

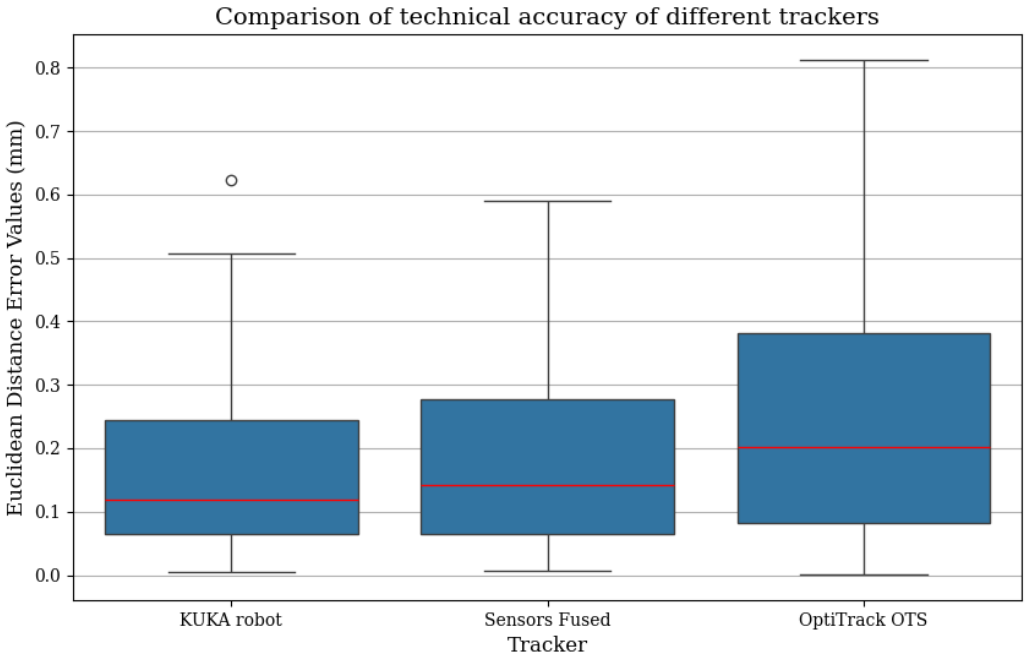

Figure 3.5: Boxplot comparing the technical accuracy of three different trackers: KUKA Robot, Sensors Fused Tracker, and OptiTrack OTS.

The results are summarized in Table 3.1, comparing the absolute accuracy of KUKA, OptiTrack, and the fused results on movements recorded on the calibration block.

Metric	OptiTrack (mm)	KUKA (mm)	Fused (mm)
Median	0.201	0.119	0.141
Mean ± SD	0.247 ± 0.201	0.164 ± 0.137	0.177 ± 0.143
Range	0.001 - 0.812	0.005 - 0.623	0.006 - 0.590

Table 3.1: KUKA and OptiTrack absolute accuracy comparison on movements on the calibration block including fused results.

Experiment 1b
Due to design restrictions of the Haply device, a different measurement setup was required. A total of 59 measurements were taken using the Haply, and the results are presented in Table 3.4.

Metric	Haply error (mm)
Median	0.556
Mean ± SD	0.502 ± 0.270
Range	0.023 - 1.074

Table 3.2: Haply technical accuracy measurements from 3D printed calibration block. Distance computed by Haply and evaluated against ground truth for error computation.

Additionally, the average error across different axes of movement for the Haply is presented in Table 3.3.

Movement	Haply error (mm)
X	0.597 ± 0.089
Y	0.843 ± 0.119
Z	0.032 ± 0.050

Table 3.3: Haply technical accuracy average error across different axes of movement.

Metric	Haply error (mm)
Median	0.556
Mean ± SD	0.502 ± 0.270
Range	0.023 - 1.074

Table 3.4: Haply technical accuracy measurements from 3D printed calibration block. Distance computed by Haply and evaluated against ground truth for error computation.

3.2.2. Results Experiments Registration Accuracy
A total of 15 rigid registrations were performed, gathering 90 target points measured by three different tracking modalities, resulting in 270 measurements. Sensor fusion outperformed the two other modalities in 28 out of these recordings, accounting for 31.11% of the measurements. The comparison of the different registrations is shown in Figure 3.5.

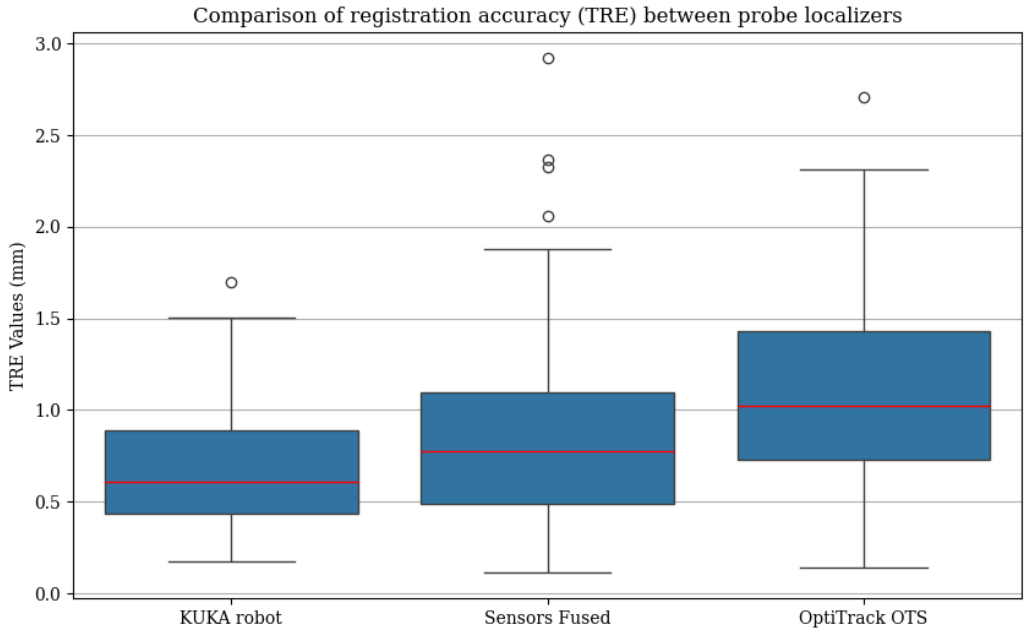

Figure 3.6: Boxplot illustrating the distribution of Target Registration Error (TRE) for different instrument tracking methods used in the registration accuracy evaluation experiment.

Metric	KUKA LBR iiwa 14 TRE (mm)	OptiTrack TRE (mm)	Fused TRE (mm)
Median	0.588	1.018	0.705
Mean ± SD	0.645 ± 0.290	1.085 ± 0.509	0.840 ± 0.521
Range	0.172 - 1.505	0.143 - 2.708	0.114 - 2.922

Table 3.5: Resulting Target Registration Error (TRE) calculations from the registration accuracy experiment on a static rigid skull phantom using different instrument trackers.

3.2.3. Results Experiments Dynamic Registration Accuracy in the Haply System

The experiment evaluated various system combinations under different movements. The different predefined movements as visualized in Figure 2.2 were measured three times. During the process, registrations with unusually high FRE were identified and reattempted. Despite these efforts, some target points were still not recorded correctly resulting in a total of 100 recorded target points and 300 TRE measurements. The results are displayed in Table 3.6 and a comparison is visualized Figure 3.6.

TRE (mm)									
Metric	OptiTrack - OptiTrack	OptiTrack - Haply	OptiTrack - Fused	KUKA - OptiTrack	KUKA - Haply	KUKA - Fused	Fused - OptiTrack	Fused - Haply	Fused - Fused
Median	1.340	5.821	1.395	1.888	5.868	1.853	1.992	6.135	2.045
Mean	1.405	6.519	1.543	1.944	6.384	2.019	2.227	6.657	2.288
SD	0.685	3.376	0.985	0.794	3.404	1.054	1.639	3.533	1.757
Min	0.116	1.798	0.249	0.426	0.979	0.381	0.483	0.950	0.486
Max	3.583	16.359	6.350	4.195	17.083	5.995	12.222	17.059	12.297

Table 3.6: Detailed Target Registration Error (TRE) metrics for different tracking combinations, calculated from 100 TRE calculations per patient and instrument tracking combination. OptiTrack - Haply denotes OptiTrack instrument tracking method and Haply patient tracking method.

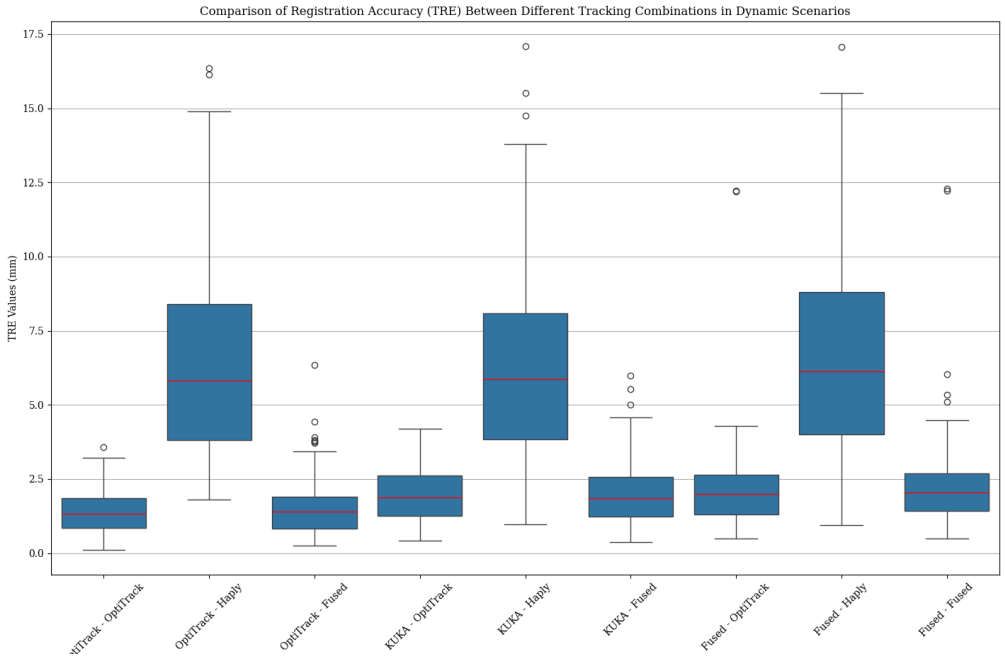

Figure 3.7: Boxplot showing the results from the third experiment, which evaluated the Target Registration Error among nine different patient and instrument tracking combinations.

3.2.4. Results of Dynamic Registration Accuracy Experiments in the Dual-Robot System

This experiment evaluated the Target Registration Error (TRE) of the Dual-Robot System in a dynamic navigation context. In total, 54 points were recorded by both the OptiTrack system and the Dual-Robot System, resulting in 108 TRE calculations, 54 for each individual patient and instrument tracker.

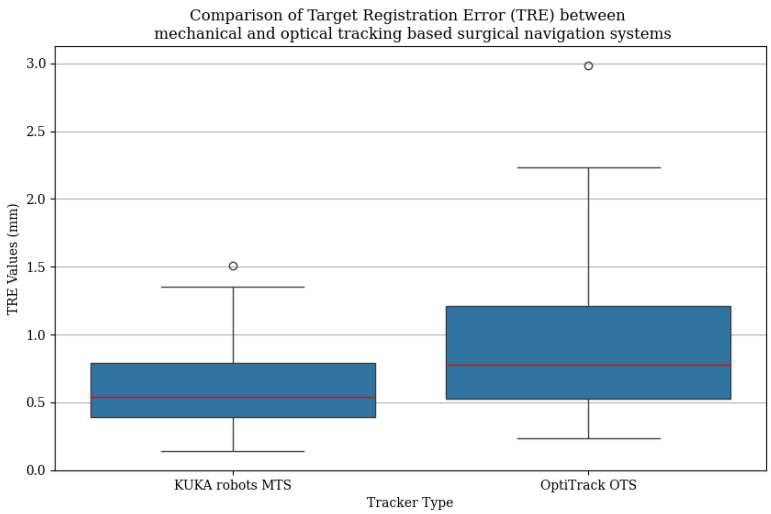

Figure 3.8: Boxplot illustrating the Target Registration Error (TRE) for two tracking systems during navigation on a phantom skull. The KUKA robots Mechanical Tracking System (MTS) uses mechanical tracking by synchronizing two KUKA robots for patient and instrument tracking, whereas the OptiTrack Optical Tracking System (OTS) employs optical tracking.

Figure 3.8 displays the boxplot visualization of the TRE data for the KUKA robot and the OptiTrack system.

Metric	KUKA MTS TRE (mm)	OptiTrack OTS TRE (mm)
Median	0.542	0.776
Mean ± SD	0.629 ± 0.301	0.894 ± 0.518
Range	0.141 - 1.512	0.239 - 2.985

Table 3.7: Comparison of the accuracy performance measured as Target Registration Error (TRE) of the KUKA Mechanical Tracking System (MTS) utilizing two KUKA robots, iiwa 7 and iiwa 14, and the OptiTrack Optical Tracking System (OTS)

4

Discussion, Future Work, and Conclusion

4.1. Discussion

This thesis aimed to take the first steps towards developing a benchmark-performing surgical robotic navigation system. The goal was to compare different patient and instrument tracking methods, systematically evaluate various sources of error in the system, and assess sensor fusion methods for performance enhancement. For this objective, the following main research question was established:

"How can a benchmark surgical robotic navigation system be established utilizing tracking methods suitable for robotic technology and systematically assessed in a reproducible manner to serve as a model for future developments?"

This main question was subdivided into the following sub-questions:

- *How do different tracking devices compare in terms of accuracy, compatibility and reliability for surgical navigation within robotic systems?*
- *How can accuracy errors be systematically assessed in surgical robotic navigation systems?*
- *To what extent can the performance of surgical robotic navigation systems be further enhanced using algorithms such as sensor fusion technology?*

Hardware Compatibility and Validation

To address the research questions, a systematic selection of hardware was undertaken to evaluate various tracking systems, leading to the selection of the Haply Inverse3 as an alternative non-optical method for patient tracking. The need for an alternative tracking system arises from the limitations of Optical Tracking Systems (OTS), which are often impractical due to their reliance on line-of-sight (LOS) and lower update frequencies. In dynamic and crowded operating room environments, LOS between the camera and the patient's dynamic reference frame (DRF) is frequently obstructed by the movement of staff and equipment. Mehbodniya et al. [6] reported 81 LOS errors over 15 neurosurgical procedures, causing significant delays that sometimes consumed up to 56% of the procedure time. Aside from OTS, other commercially available solutions are systems using electromagnetic tracking that mitigate LOS issues. However, they are significantly less accurate and are highly affected by electromagnetic interference [4] [5]. Additionally, current surgical navigation systems typically exhibit low update frequencies and high latency [5], making the systems inapt for applications in surgical robotics that require high update frequencies and low latency to ensure safe procedures. For effective motion capture in OTS, the update rate should be higher than the maximum velocity of the marker divided by the marker spacing in meters, often resulting in frequencies over 100 Hz for fast movements [50]. To ensure the robotic system can both measure and respond to patient movement effectively, the update rate should be significantly higher than the minimum required to measure the movement. The Haply Inverse3 device, with its compact design, addresses LOS issues and features a light end-effector that minimizes resistive forces at the attachment point, necessary for avoiding bone damage or splint deformation during patient movement [17]. The device's ability to update its end-effector position at 4 kHz makes it suitable for rapid responses in robotic setups. The Haply is intended for haptic applications, specifically for rendering forces from virtual objects at the end-effector location with high resolution. It was hypothesized that if the Haply could render 3D objects in space with high resolution, it might also be able to accurately determine the position of its end-effector in space. Additionally, the Haply is cost-effective compared to other mechanical alternatives such as Coordinate Measuring Machines (CMM) and robotic manipulators, as detailed in Appendix C. This combination of potentially accurate end-effector tracking, minimal back-drivability, sufficient workspace, high update frequency,

the absence of the LOS requirement, and its cost-effectiveness motivated the evaluation of the Haply as a patient tracking system.

The limitations of optical tracking surgical navigation systems and their inadequacy for robotic applications do not inherently disqualify optical tracking technology from use in surgical robotic navigation. For instance, the OptiTrack tracking system, commonly employed in robotic research, is known for its high accuracy and sufficient update frequencies above 200 Hz [51]. Unlike typical surgical optical navigation devices that often use a dual camera system mounted on a wheeled base [52], the OptiTrack system is equipped with multiple cameras positioned around the entire tracking volume, which significantly reduces LOS errors. To address the research objective to evaluate various tracking solutions, the OptiTrack camera system was selected to compare the Haply Inverse3 against an established tracking system.

Before actual experimentation, the individual components of the Haply System were validated to investigate the presence of systemic errors and indicate performance. This process was complex as systemic errors are often hidden in the firmware and are not readily apparent. Specifications such as camera resolution, 3D accuracy, or encoder resolution do not necessarily indicate the actual technical accuracy of the devices.

The Haply performed adequately only in certain configurations and movements, while its performance was significantly less reliable in other areas within its workspace. The VerseGrip orientation measurement device exhibited inconsistent behavior, sometimes accurately conveying the rotation of the skull while at other times being completely inaccurate. The device's measurement method and performance specifications were unclear, other than having a 16-bit quaternion resolution and an update rate of about 200 Hz. Upon inspection, it was found that while the VerseGrip sampled at 200 Hz, it actually only updated at 25 Hz, as it sampled the same eight points consecutively before updating with new values, impacting its accuracy performance in higher-speed movements. Moreover, after gathering an indication of the technical accuracy of the Haply end-effector, many systemic errors became evident due to firmware issues as well as initialization and calibration problems. Haply Robotics acknowledged the systemic error behavior and noted they had not experienced this issue before. They provided methods to resolve the issues, resulting in an improvement from a 10 mm slope downwards on a flat surface over the device's reach to 1 mm.

The OptiTrack manufacturer stated that results below 0.1 mm were obtained with setups similar to those used in this research. However, the performance of OptiTrack is highly dependent on camera configuration, lighting conditions, exposure, focus settings, and even temperature. Small disturbances or rearrangements of individual cameras can heavily impact accuracy when aiming for measurements far below 1 mm. Configuring the OptiTrack system and the calibration process is time-consuming and impractical, making it unlikely to be feasible in clinical environments. Moreover, the optimal conditions needed to achieve the manufacturer's stated results are hard to replicate in operating rooms due to reflections, LOS requirements of each camera, and camera positioning. OptiTrack provided assistance with configuration and calibration, resulting in a residual error (the error in ray convergence of the marker reconstruction [53]) averaging 0.5 mm. This was the highest achievable with the current conditions and setup; however, better conditions might allow for significantly lower residual error and potentially increased technical accuracy of the system.

After the process of optimizing calibration settings and validating components, the performance indications were sufficient to proceed with actual experiments using the hardware. As highlighted by the hardware validation process in this research, it is important to test the components when developing custom integrations using systems from different manufacturers, to validate manufacturers' reported performances, assess systemic errors, and gather an indication of actual performance within an applicable environment.

Systematic Accuracy Evaluation

The first set of experiments explained in Section 3.1.1 aimed to evaluate the technical accuracy of the selected hardware components. By measuring spatial distances against the ground truth of the OptiTrack calibration block, the alignment of the system's measured dimensions could be compared with the real world. The measurements in this setup showed that the OptiTrack system was less reliable and more inaccurate than the KUKA robot. Robotic manipulators are generally known to be very repeatable but not highly accurate when uncalibrated. Typically, the repeatability of a robotic manipulator is around 0.1 - 0.2 mm, while the accuracy can be within several millimeters [54]. Therefore, it was unexpected to see that the uncalibrated robot achieved accurate positional readouts below the millimeter, attaining higher accuracies than the OptiTrack system. Using an industrial robot as a passive, gravity-compensated measurement device, differs from its intended use as an active manipulator. Besset et al. [55] showed in experimental work that the maximum active absolute pose error of an uncalibrated KUKA LBR iiwa robotic manipulator is up to 2.5 mm. By creating a geometric model using Denavit-Hartenberg (DH) parameters

and modeling the joints as rotary springs, Besset et al. developed a comprehensive representation of the robot. They calibrated this model by taking measurements using a laser tracker. Through this calibration, Besset et al. were able to achieve a maximum pose accuracy of 0.4 mm. The obtained values in the first experiment with the KUKA suggest the robot's inherent technical accuracy has a median positioning error of 0.119 mm. This implies in general an accurate kinematic model, however it does not suggest that other significant factors such as joint compliance are accurately modeled in the system and that through active robot control the robot can achieve similar results.

The second set of experiments (Section 3.1.2) was designed to evaluate the registration accuracy of different instrument tracking methods. The Target Registration Error (TRE) was assessed for the KUKA LBR iiwa 14, OptiTrack, and a fused system, using the skull phantom rigidly attached to the mounting table. The KUKA robotic manipulator demonstrated the lowest median TRE (0.588 mm), followed by the fused system (0.705 mm), with the OptiTrack system having the highest median TRE (1.018 mm). This indicates that the KUKA system, which relies on its joint encoders and kinematic model, provides more accurate positional estimates compared to the optical tracking system.

When comparing these results with the third set of experiments for dynamic navigation accuracy (Section 3.1.3), the performance of these systems during dynamic movements varied significantly based on the combination of patient and instrument tracking methods. Among the different combinations, using OptiTrack for both patient and instrument tracking exhibited the least amount of error and variability. However, the performance of all systems degraded compared to static conditions, illustrating the impact of dynamic movements on tracking accuracy. In the Haply System, because the kinematic model of the Haply was not known and the transformation from tool to Haply was absent, relative distances to a DRF were not sampled. Instead, registration was performed first, and then the registration transformation matrix was updated by measuring relative changes. This additional transformation step of updating the initial patient-to-image transformation with a global transformation matrix likely introduced cumulative errors and uncertainties. To ensure similar system comparisons, OptiTrack tracked the patient in the same manner, likely degrading its performance. In contrast, the Dual-Robot System maintained higher accuracy by directly sampling relative distances from the dynamic reference frame (DRF), thereby reducing transformation steps and minimizing error propagation. OptiTrack showed better and less variable results in the final experiments with the Dual-Robot System compared to its performance in the Haply System. This improvement may be attributed to reduced transformations and error propagation, but other environmental and calibration factors are also at play, as OptiTrack was re-calibrated and reconfigured in the final experiments.

Evaluating surgical robotic navigation systems in dynamic scenarios with realistic human movements still requires further investigation. From the reviewed articles in Appendix A, over 57% of the initiatives fixated the subject during the experiments, while 40% did not report information about subject fixation. Rigidly fixating a patient is not always a practical clinical solution and is often invasive. Therefore, robotic systems are likely to be integrated with patients whose anatomy is not rigidly fixed, allowing for movements such as spasms or adjustments by surgeons. The results from the dynamic registration experiment indicated that movement of the skull significantly impacted overall navigation accuracy, thereby affecting system performance. Current literature often fails to address the effects of dynamic movements on tracking accuracy; hence, it is recommended to incorporate dynamic conditions in the evaluation of surgical robotic navigation systems.

The Haply device as a patient tracker performed significantly below acceptable values for clinical applications in Cranio-Maxillofacial (CMF) Surgery, with an average TRE of 6.519 mm and a maximum value of 16.359 mm. This demonstrates that the Haply Inverse3 is not a viable alternative for patient tracking. The high inaccuracies and discrepancies observed, especially when comparing results from from the technical accuracy experiment, can largely be attributed to the poor performance of the Haply Inverse3 orientation measurement device, the VerseGrip. When tracking only the position of the skull with the Haply end-effector and handling orientation with OptiTrack, the performance ranged below 2 mm and proved to be more stable. The VerseGrip device updated measurements at a very low rate and often caused significant orientation estimation errors. There are higher quality orientation measurement devices available on the market like Inertial Measurement Units (IMUs) that can be effective in combination with other tracking modalities [56][36]; however, they might not be suitable as the primary tracking modality in surgical applications due to their drifting properties and inherent unreliability.

Sensor Fusion

Throughout the first three experiments, sensor fusion models were active for both instrument tracking and patient tracking. The primary expectation of employing sensor fusion in the surgical robotic navigation system was to achieve more accurate and robust state estimation by integrating data from multiple sensors. Specifically, it was

anticipated that the Kalman filter-based fusion of instrument data and Unscented Kalman Filter (UKF) for patient tracking data would provide smoother and more reliable tracking than individual sensors alone, compensating for outliers and reducing overall errors.

The results varied across different experiments, with sensor fusion sometimes improving performance over individual systems and sometimes not. In the first set of experiments to evaluate the individual technical accuracy, sensor fusion provided a median error between the individual errors of the KUKA and OptiTrack systems. In the second experiments to evaluate the registration accuracy, sensor fusion improved the Target Registration Error (TRE) for 31,11% of the measurements but also introduced extra outliers. The Kalman Filter employed to fuse the sensor measurements of OptiTrack with the robotic manipulator uses a measurement noise covariance matrix and a process noise covariance matrix. The process noise covariance matrix determines the trust of the system in the dynamic model, while the measurement noise covariance matrix is constructed based on the noise characteristics of the sensors and tells the system how much to rely on each measurement source. Essentially, it guides the filter on which measurement distribution to trust more. In the first set of experiments, the noise characteristics from Figure 2.15 were used, which were obtained by analyzing the noise when keeping the surgical instrument stable. This configuration made the system heavily rely on KUKA's measurements, rather than effectively fusing the measurements from both systems. After evaluation, the measurement noise covariance matrix was adjusted to give the KUKA a slightly higher value, ensuring OptiTrack's measurements were also considered. This adjustment resulted in more instances of better performance in the second set of experiments compared to the first experiments but also caused more significant outliers. Further tuning of the process and measurement noise in the Kalman Filter model might yield more reliable results.

In the instrument position estimation model, the noise proved to be Gaussian distributed, thereby justifying the use of a Kalman Filter, which is optimal for Gaussian noise environments. The model was simplified to a constant velocity assumption, making the Kalman Filter the computationally most efficient choice. For patient orientation estimation, the inherent non-linear nature of the quaternions provided by the sensors motivated the choice for an Unscented Kalman Filter (UKF), as the UKF is more adept at handling non-linearities. However, in both cases, the mixed results could be attributed to the lack of a comprehensive dynamic model. Developing a detailed model of the robot that considers multiple perspectives and dynamic behaviors could significantly improve the effectiveness of sensor fusion. Additionally, modeling the patient's movement could enhance patient estimation, although creating a model of a tracked patient poses significant challenges due to inter-patient variation and the complexity of biomechanical modeling of human movement.

While sensor fusion can potentially enhance performance, the clinical relevance of these improvements is debatable. Implementing a fusion model requires multiple sensors and introduces additional latency, particularly with advanced filtering approaches like the Unscented Kalman Filter (UKF). With ongoing hardware improvements, the technical accuracy might be nearing the device's resolution or repeatability limits. Further enhancements, potentially on the order of microns, may not translate into significant functional or aesthetic benefits postoperatively. A more advantageous application of sensor fusion could be to increase system reliability or serve as a fallback in case of sensor failure. For instance, sensor fusion can address line-of-sight (LOS) issues, as demonstrated in the research by Yang et al. [39]. They implemented an Error-State Kalman Filter (ESKF) using gyroscope and optical tracking orientation data, which significantly improved orientation accuracy and handled LOS occlusions for periods of 20 to 30 seconds. Sensor fusion might serve robotic navigation systems more effectively as a means of enhancing safety and managing errors rather than solely improving performance.

The Dual-Robot System

Since the Haply and the OptiTrack system, whether used separately or in combination, did not prove to be the most optimal for surgical navigation, and the setup constrained dynamic registration, it was considered insightful to explore another system using different transformations and tracking methods. One system was completely tracked mechanically through two robots and their encoders, while the other used the OptiTrack optical tracking system. The Dual-Robot system represents a first effort in evaluating a complete mechanical tracking system in surgical robotic navigation, and the results show that, among all efforts, the mechanical Dual-Robot System was the best-performing tracking system in both Target Registration Error as in performance specifications such as update rate and latency. However, the Dual-Robot System is far from clinically feasible. Operating rooms are crowded and dynamic places that do not have sufficient space around the patient to accommodate two industrial collaborative robots. Moreover, despite the suitability of the robots' collaborative features for sensitive environments, their substantial weight and strength introduce significant resistive forces at the end-effector. Additionally, the results obtained with the Dual-Robot system have been achieved in an *in-vitro* setup, where many potential sources of error are minimized. Consequently, these results may not be as favorable in clinical environments due to the

introduction of factors such as Fiducial Localization Error, imaging error, and clinical variabilities. Nonetheless, the mechanical robotic system illustrates that two robots can effectively navigate when the transformation between their bases is known. This sets a benchmark for what can be achieved with currently available hardware and highlights potential for further development in the field.

The Haply System has been identified as possible clinically interesting tracking method, but it falls short of the accuracy requirements necessary for clinical implementation. Conversely, the Dual-Robot system demonstrates potential in meeting accuracy standards but is hindered by its bulky, heavy design and the possibility of resistive forces at the end-effector, making it impractical for clinical use. A mechanical tracking system could offer advantages over an optical tracking system in surgical robotic navigation. However, it is essential to develop a design that is both clinically practical and suitable for robotic applications. This design should provide a sufficient workspace and maintain low resistive forces. The YOMI dental implant robot utilizes a mechanical tracking arm, yet there is limited information on the system's operation or the performance of its navigation system, as noted in Appendix A and evident in [57] and [58]. Research on the development of mechanical surgical navigation systems is sparse. Sin et al. [17] have presented a 6DOF motion capture system for dental implant robots, highlighting significant design challenges and providing a performance evaluation focused on technical accuracy. Their research demonstrated the feasibility of such a device, achieving accuracy below 0.15mm. However, limitations included an insufficient workspace and excessive resistive force at the end-effector. Moreover, the performance has not been addressed in an *in-vitro* surgical robotic navigation system. To address these challenges, a collaborative effort among biomechanical engineers, roboticists, and clinicians is essential for designing a 6DOF mechanical tracker arm that meets the necessary clinical and technical requirements.

Performance Reporting
Throughout this research, it has become evident that there is a need for a standardized protocol to evaluate surgical robotic navigation systems, along with a benchmark that includes recommended minimal performance requirements. Surgical navigation systems are subject to various sources of error, which are integrative and include technical, imaging, registration, application and human error [45]. The application error refers to the deviation of the surgical outcome from the initial plan. The systematic review in Appendix A indicates that while 70% of the reviewed articles report on the application error of surgical robotic systems, only 5% provide data on both technical and application errors. This lack of comprehensive reporting creates ambiguity, as the total application error is difficult to reproduce and does not clearly highlight areas for improvement within the system. For instance, if the technical error of a robotic manipulator is significant and the total application error closely matches this figure, robot calibration methods could potentially lead to substantial improvements. Therefore, the experiments conducted in this research are designed to isolate and evaluate different sources of error. The systematic review shows that among the 159 articles included, only 54 reported on the performance of the surgical navigation systems used in robotic setups. Furthermore, these 54 articles employed 32 different reporting methods (Appendix A). This inconsistency underscores the need for a unified reporting standard to better assess and compare the performance of these systems.

4.2. Future Work

In Appendix A, it was found that current performance reporting on navigation systems in surgical robotics is unstructured and often insufficient for adequate clinical research. Therefore, in the near future, we intend to publish the results of the systematic review in a scientific journal, accompanied by a framework that provides recommendations on how and what to report regarding the employed navigation system based on the research category.

During the development of a surgical robotic navigation system, this research aimed to systematically assess the different sources of error within the system. However, establishing certain results, selecting appropriate equipment and tools, determining relevant metrics, and deciding the number of experimental repetitions were often unclear. Additionally, the variability in assessment methods complicates comparisons with other research. For instance, in this research, a phantom skull was 3D-printed incorporating 6 registration fiducials and 6 target fiducials distributed around the skull. Other studies often use their own phantom implementations with varying numbers of registration and target fiducials. However, increasing the number of registration fiducials or positioning the targets in close proximity to the registration fiducials can significantly impact the registration error. For manufacturers creating a new robotic manipulator, ISO 9283 offers procedures to properly measure robot position accuracy, repeatability, and path accuracy [59] [14]. Alongside the results and the framework from the systematic review, we intend to develop a test protocol that guides researchers on how to gather the required performance metrics recommended by the

framework. Such a protocol would standardize performance reporting and facilitate comparisons between different manufacturers. A similar protocol for surgical navigation systems would provide direction in this research field and foster future developments. Therefore, alongside the developed framework that specifies what to report on surgical robotic navigation performance based on the type of research, we aim to develop a protocol that establishes guidelines on how to obtain the required performance measures in different scenarios.

The protocol established will be used in continued research to develop a benchmark surgical robotic navigation system. Our findings suggest that mechanical tracking could be as accurate as, or even more accurate than, the optical tracking systems currently used in surgical navigation. This advantage, combined with the ability to address line-of-sight issues and the constraints of a surgical workspace, supports further investigation and development in this area. However, the bulky robotic manipulator employed as a patient tracker may not be suitable for clinical scenarios. Alternative commercially available hardware is very limited. Appendix C provides an overview of the available hardware options. Haptic devices, such as the Haply Inverse3, offer low backdrivability but suffer from insufficient orientation tracking accuracy due to reliance on orientation measurement devices rather than high-speed encoders. Articulated coordinate measuring machine arms provide high accuracy but exhibit resistive forces and require handling with both hands. Collaborative robotic manipulators like the KUKA LBR series can minimize resistance but are too bulky for crowded operating theaters. Smaller manipulators, such as the MECA 500, offer high accuracy and minimal space occupation but lack the collaborative features needed to respond to patient movements. Given these limitations, there is a clear need to develop a new mechanical patient tracking arm. Previous initiatives, as mentioned in [17], demonstrated sufficient accuracy but high backdrivability and complex, fragile designs. Future research should focus on redesigning a collaborative patient tracker arm that is accurate, has low backdrivability, and is suitable for clinical use. Collaboration with clinicians to evaluate intraoperative requirements, biomechanical specialists to assess potential patient movement, workspace, and fixation, and robotic and mechanical engineers for hardware and software design is essential. This interdisciplinary approach would help develop a low-resistance, clinically adaptable arm. Once developed, this arm should be tested according to the established protocol, evaluating its accuracy and establishing a benchmark that can be used in future research.

In this research, we minimized the Fiducial Localization Error (FLE) and imaging error by directly printing the registration fiducials around the skull. Despite nearly optimal conditions, significant registration errors persisted. In clinical settings, it is unlikely to have six registration fiducials equally distributed around the skull, and fiducial localization errors, errors in the 3D printed registration splint, and human errors in identifying the fiducials during registration can occur. Improving registration remains an open challenge in both surgical navigation as surgical robotic navigation, both in terms of practicality and accuracy [60]. Collaborative robots, equipped with advanced force-torque sensing capabilities, can accurately perceive and respond to their environments, enhancing their ability to perform precise and adaptive tasks in dynamic settings. The sensory information provided by the robotic manipulator during surgery could be effectively used to continuously update the transformation data obtained from the registration method. Using gathered intraoperative positional and force sensory data can be incorporated in a feedback system to update the registration and provide error correction.

To the authors' knowledge, limited research has been conducted on error correction during surgical navigation. Wittmann et al. [46] utilized an error identification technique based on the assumption that the surgical instrument cannot penetrate the bone. By using bone density information from CT data and predicting the location of the surgical instrument, their method corrects the registration whenever the instrument is detected within the bone, significantly improving the overall Target Registration Error (TRE). However, this research was conducted solely on a phantom in an in-vitro setup and was not further investigated, despite its promising potential. Similar methods could be employed to update the registration using force sensors on robotic manipulators, leveraging the resistive forces encountered during interaction with the patient that indicate material properties of different anatomical structures and thereby, update the registration accordingly.

The robotic manipulators used in this research, as stated in the discussion, were not calibrated and were only used as passive measurement tools under gravity compensation control. If the navigation system is established and accurate navigation is ensured, robotic manipulators can be employed to guide surgeons using haptic feedback, reposition bones or implants, and stabilize them in the correct positions. To achieve this, not only the measurement accuracy but also the pose accuracy of the robotic manipulator should be considered. As noted in the discussion, the accuracy of the kinematic model used by both robots is already quite precise, with errors far below 1 mm.

In future work, the authors will aim to develop a dynamic model of the KUKA LBR iiwa robots, which includes modeling any kinematic errors and, more importantly, the joint compliance of the robotic manipulator. This, in combination with a positional feedback loop, can improve the pose accuracy of the robotic manipulator. Prior

to this, the accuracy of the robotic manipulator should be assessed to measure any improvements. Dynamic parameters are critical in the design of control laws based on the dynamics model or in implementing human-robot interaction algorithms such as collision detection and reaction control, and impedance control.

Successfully establishing the dynamic model of the robotic manipulator will enable more effective methods of sensor fusion and safety management. The model can incorporate the sensing features of the robotic manipulator and positional information, allowing for enhanced registration accuracy. Additionally, equipping the robotic manipulator with a depth stereo RGB camera could allow it to detect the patient and automatically adjust its stiffness when interacting with them. This integration of the dynamic model with force sensory information and a depth camera can make the system more compliant with its environment and ensure safer and more effective collaborative patient handling.

As a final remark, the future of surgical robotics should not be envisioned as completely autonomous but rather as a shared control environment. Surgeons should be trained and collaborate with specialists to understand the systems they are using. Robotic manipulators can offer potentially remarkable guidance capabilities, improve the surgeon's workflow, and reduce the intraoperative workload. However, due to inter-patient variability and dynamic operating environments, operators should maintain control and exercise judgment. It is also essential to continue this research in environments that closely resemble real clinical settings. This involves using clinical equipment and conducting studies with cadavers to establish a baseline for comparing the effectiveness of optical navigation systems.

4.3. Conclusion

Current surgical navigation systems used in surgical robotic research exhibit both practical and performance limitations. This research aimed to develop a surgical robotic navigation system to investigate how a benchmark can be set for surgical robotic navigation. By investigating sensor fusion algorithms, the goal was to enhance performance. Two systems were employed: the Haply System, which uses a compact haptic controller for surgical navigation, and the Dual-Robot System, which comprises two robotic manipulators, one tracking the patient and the other tracking the instrument. Both systems used OptiTrack for comparison and sensor fusion integration in the Haply System. The sensor fusion models did not significantly improve the results due to the lack of dynamical models. The Dual-Robot System proved to be the most reliable in terms of accuracy and performance, achieving sub-millimeter Target Registration Error. However, it was also deemed the most clinically impractical due to its operational constraints. In contrast, the Haply Inverse3 system did not meet the necessary accuracy requirements for future clinical research. Together, these findings indicate that further improvement is required before the system can be considered a viable alternative for surgical robotic navigation. Overall, the establishment of the two surgical robotic navigation systems marks the first steps toward creating a benchmark for performance evaluation in surgical robotic navigation. The development of a clinically practical and accurate system continues to be an ongoing effort.

References

[1] G. Eggers et al. “Image-to-patient registration techniques in head surgery”. In: *Int J Oral Maxillofac Surg* 35.12 (2006). Eggers, G Mühling, J Marmulla, R Journal Article Review Denmark 2006/11/11 Int J Oral Maxillofac Surg. 2006 Dec;35(12):1081-95. doi: 10.1016/j.ijom.2006.09.015., pp. 1081–95. DOI: 10.1016/j.ijom.2006.09.015.

[2] M. R. DeLong et al. “Intraoperative Image-Guided Navigation in Craniofacial Surgery: Review and Grading of the Current Literature”. In: *J Craniofac Surg* 30.2 (2019). 1536-3732 DeLong, Michael R Gandolfi, Brad M Barr, Meaghan L Datta, Neha Willson, Thomas D Jarrahy, Reza Journal Article Systematic Review United States 2019/01/15 J Craniofac Surg. 2019 Mar/Apr;30(2):465-472. doi: 10.1097/SCS.0000000000005130., pp. 465–472. DOI: 10.1097/scs.0000000000005130.

[3] N. Demian et al. “Surgical Navigation for Oral and Maxillofacial Surgery”. In: *Oral Maxillofac Surg Clin North Am* 31.4 (2019). 1558-1365 Demian, Nagi Pearl, Craig Woernley, Timothy Charles 3rd Wilson, James Seaman, Justin Journal Article Review United States 2019/08/11 Oral Maxillofac Surg Clin North Am. 2019 Nov;31(4):531-538. doi: 10.1016/j.coms.2019.06.001. Epub 2019 Aug 7., pp. 531–538. DOI: 10.1016/j.coms.2019.06.001.

[4] Florian Kral et al. “Comparison of optical and electromagnetic tracking for navigated lateral skull base surgery”. In: *The International Journal of Medical Robotics and Computer Assisted Surgery* 9.2 (2013), pp. 247–252. DOI: https://doi.org/10.1002/rcs.1502. eprint: https://onlinelibrary.wiley.com/doi/pdf/10.1002/rcs.1502. URL: https://onlinelibrary.wiley.com/doi/abs/10.1002/rcs.1502.

[5] A. Sorriento et al. “Optical and Electromagnetic Tracking Systems for Biomedical Applications: A Critical Review on Potentialities and Limitations”. In: *IEEE Reviews in Biomedical Engineering* 13 (2020), pp. 212–232. DOI: 10.1109/RBME.2019.2939091.

[6] Amir H Mehbodniya et al. “Frequency and causes of line of sight issues during neurosurgical procedures using optical image-guided systems”. In: *World neurosurgery* 122 (2019), e449–e454.

[7] S. Baron et al. “Percutaneous inner-ear access via an image-guided industrial robot system”. In: *Proc Inst Mech Eng H* 224.5 (2010). 2041-3033 Baron, S Eilers, H Munske, B Toennies, J L Balachandran, R Labadie, R F Ortmaier, T Webster, R J 3rd R21 EB006044/EB/NIBIB NIH HHS/United States R21 EB006044-01A1/EB/NIBIB NIH HHS/United States Journal Article Research Support, N.I.H., Extramural Research Support, Non-U.S. Gov’t England 2010/08/20 Proc Inst Mech Eng H. 2010;224(5):633-49. doi: 10.1243/09544119JEIM781., pp. 633–49. DOI: 10.1243/09544119jeim781.

[8] Wolfram M.H. Kaduk et al. “Surgical Navigation in Reconstruction”. In: *Oral and Maxillofacial Surgery Clinics of North America* 25.2 (2013). Maxillofacial Reconstruction, pp. 313–333. DOI: https://doi.org/10.1016/j.coms.2013.01.003. URL: https://www.sciencedirect.com/science/article/pii/S1042369913000150.

[9] Theophilos S Paleologos et al. “Clinical utility and cost-effectiveness of interactive image-guided craniotomy: clinical comparison between conventional and image-guided meningioma surgery”. In: *Neurosurgery* 47.1 (2000), pp. 40–48.

[10] Neal Luther et al. “Comparison of navigated versus non-navigated pedicle screw placement in 260 patients and 1434 screws: screw accuracy, screw size, and the complexity of surgery”. In: *Clinical Spine Surgery* 28.5 (2015), E298–E303.

[11] M. Ebeling et al. “First-Hand Experience and Result with New Robot-Assisted Laser LeFort-I Osteotomy in Orthognathic Surgery: A Case Report”. In: *J Pers Med* 13.2 (2023). 2075-4426 Ebeling, Marcel Scheurer, Mario Sakkas, Andreas Wilde, Frank Schramm, Alexander Journal Article Switzerland 2023/02/26 J Pers Med. 2023 Feb 3;13(2):287. doi: 10.3390/jpm13020287. DOI: 10.3390/jpm13020287.

[12] Mary Downes Gastrich et al. “Robotic surgery: review of the latest advances, risks, and outcomes”. In: *Journal of robotic surgery* 5 (2011), pp. 79–97.

[13] Tom CT van Riet et al. “Robot technology in dentistry, part one of a systematic review: literature characteristics”. In: *Dental materials* 37.8 (2021), pp. 1217–1226.

[14] International Organization for Standardization. *ISO 9283: Manipulating industrial robots – Performance criteria and related test methods*. ISO Standard ISO 9283. Geneva, Switzerland: International Organization for Standardization, 1998.

[15] KUKA AG. *KUKA LBR iiwa*. https://www.kuka.com/products/robotics-systems/industrial-robots/lbr-iiwa. Accessed: 2023-10-10.

[16] Vinay Chawda et al. “Toward controlling a kuka lbr iiwa for interactive tracking”. In: *2017 IEEE International Conference on Robotics and Automation (ICRA)*. IEEE. 2017, pp. 1808–1814.

[17] Minki Sin et al. “Development of a Real-Time 6-DOF Motion-Tracking System for Robotic Computer-Assisted Implant Surgery”. In: *Sensors* 23.5 (2023), p. 2450. URL: https://www.mdpi.com/1424-8220/23/5/2450.

[18] Samuel Gilman et al. “Measurement of head movement during auditory localization”. In: *The Journal of the Acoustical Society of America* 11 (1979), pp. 37–41. DOI: 10.3758/BF03205429.

[19] Natural Point (INC). *Optical Tracking System*. https://optitrack.com/cameras/primex-13/specs.html.

[20] Natural Point (INC). *Digitizer Probe Optitrack*. https://optitrack.com/accessories/measurement-tools/.

[21] Jia-Qing Xuan et al. “Review on kinematics calibration technology of serial robots”. In: *International journal of precision engineering and manufacturing* 15 (2014), pp. 1759–1774.

[22] ZVIS Roth et al. “An overview of robot calibration”. In: *IEEE Journal on Robotics and Automation* 3.5 (1987), pp. 377–385.

[23] Stanford Artificial Intelligence Laboratory et al. *Robotic Operating System*. Version ROS Noetic. May 23, 2018. URL: https://www.ros.org.

[24] Konstantinos Chatzilygeroudis et al. *iiwa_ros: A ROS Stack for KUKA’s IIWA Robots Using the Fast Research Interface*. EPFL-LASA, 2019. URL: http://github.com/epfl-lasa/iiwa_ros.

[25] Stephen Thompson et al. “SciKit-Surgery: compact libraries for surgical navigation”. In: *International journal of computer assisted radiology and surgery* 15 (2020), pp. 1075–1084.

[26] Dassault Systèmes. *SolidWorks*. URL: %5Curl%7Bhttps://www.solidworks.com/%7D.

[27] Blender Foundation. *Blender*. Version Blender 4.0. URL: https://www.blender.org.

[28] Peter Corke et al. “Not your grandmother’s toolbox – the Robotics Toolbox reinvented for Python”. In: *2021 IEEE International Conference on Robotics and Automation (ICRA)*. May 2021, pp. 11357–11363. DOI: 10.1109/ICRA48506.2021.9561366.

[29] A.F. de Geer et al. “Registration methods for surgical navigation of the mandible: a systematic review”. In: *International Journal of Oral and Maxillofacial Surgery* 51.10 (2022), pp. 1318–1329. DOI: https://doi.org/10.1016/j.ijom.2022.01.017. URL: https://www.sciencedirect.com/science/article/pii/S0901502722000340.

[30] Fakhre Alam et al. “A Review on Extrinsic Registration Methods for Medical Images”. In: *Technical Journal University of Engineering and Technology Taxila* 21 (Oct. 2016), pp. 110–119.

[31] Reuben R. Shamir et al. “Geometrical analysis of registration errors in point-based rigid-body registration using invariants”. In: *Medical Image Analysis* 15.1 (2011), pp. 85–95. DOI: https://doi.org/10.1016/j.media.2010.07.010. URL: https://www.sciencedirect.com/science/article/pii/S1361841510001027.

[32] K Somani Arun et al. “Least-squares fitting of two 3-D point sets”. In: *IEEE Transactions on pattern analysis and machine intelligence* 5 (1987), pp. 698–700.

[33] Ento Key. *Image-Guided Technique in Neurotology*. Accessed: 2024-05-31. 2017. URL: https://entokey.com/image-guided-technique-in-neurotology/.

[34] Wenbin Zhang et al. "Effect of fiducial configuration on target registration error in image-guided craniomaxillofacial surgery." In: *Journal of cranio-maxillo-facial surgery : official publication of the European Association for Cranio-Maxillo-Facial Surgery* 39 6 (2011), pp. 407–11. DOI: 10.1016/j.jcms.2010.10.008.

[35] Christian Ott. *Cartesian impedance control of redundant and flexible-joint robots*. Springer, 2008.

[36] C. He et al. "An Inertial and Optical Sensor Fusion Approach for Six Degree-of-Freedom Pose Estimation". In: *Sensors (Basel)* 15.7 (2015). 1424-8220 He, Changyu Kazanzides, Peter Sen, Hasan Tutkun Kim, Sungmin Liu, Yue Journal Article Research Support, Non-U.S. Gov't Switzerland 2015/07/18 Sensors (Basel). 2015 Jul 8;15(7):16448-65. doi: 10.3390/s150716448., pp. 16448–65. DOI: 10.3390/s150716448.

[37] J.Z. Sasiadek. "Sensor fusion". In: *Annual Reviews in Control* 26.2 (2002), pp. 203–228. DOI: https://doi.org/10.1016/S1367-5788(02)00045-7. URL: https://www.sciencedirect.com/science/article/pii/S1367578802000457.

[38] Ren C. Luo et al. "Multisensor Fusion and Integration: Theories, Applications, and its Perspectives". In: *IEEE Sensors Journal* 11.12 (2011), pp. 3122–3138. DOI: 10.1109/JSEN.2011.2166383.

[39] Zhicheng Yang et al. "Improvement of Optical Tracking-Based Orientation Estimation by Fusing Gyroscope Information". In: *IEEE Transactions on Instrumentation and Measurement* PP (2021), pp. 1–1. DOI: 10.1109/TIM.2021.3073293.

[40] Kjartan Halvorsen et al. "Using an extended Kalman filter for rigid body pose estimation". In: (2005).

[41] Claudio Urrea et al. "Kalman filter: historical overview and review of its use in robotics 60 years after its creation". In: *Journal of Sensors* 2021 (2021), pp. 1–21.

[42] *ROS Message Filters Documentation*. https://docs.ros.org/en/lunar/api/message_filters/html/python/index.html. Accessed: 01-01-2024.

[43] Alberto Vaccarella et al. "Unscented Kalman Filter Based Sensor Fusion for Robust Optical and Electromagnetic Tracking in Surgical Navigation". In: *IEEE Transactions on Instrumentation and Measurement* 62.7 (2013), pp. 2067–2081. DOI: 10.1109/TIM.2013.2248304.

[44] Eric A Wan et al. "The unscented Kalman filter for nonlinear estimation". In: *Proceedings of the IEEE 2000 adaptive systems for signal processing, communications, and control symposium (Cat. No. 00EX373)*. Ieee. 2000, pp. 153–158.

[45] Gerlig Widmann et al. "Errors and error management in image-guided craniomaxillofacial surgery". In: *Oral Surgery, Oral Medicine, Oral Pathology, Oral Radiology, and Endodontology* 107.5 (2009), pp. 701–715.

[46] Wolfgang Wittmann et al. "Automatic correction of registration errors in surgical navigation systems". In: *IEEE transactions on biomedical engineering* 58.10 (2011), pp. 2922–2930.

[47] J Michael Fitzpatrick. "Fiducial registration error and target registration error are uncorrelated". In: *Medical Imaging 2009: Visualization, Image-Guided Procedures, and Modeling*. Vol. 7261. SPIE. 2009, pp. 21–32.

[48] J. M. Fitzpatrick et al. "The distribution of target registration error in rigid-body point-based registration". In: *IEEE Trans Med Imaging* 20.9 (2001). Fitzpatrick, J M West, J B Journal Article Research Support, Non-U.S. Gov't Research Support, U.S. Gov't, Non-P.H.S. United States 2001/10/05 IEEE Trans Med Imaging. 2001 Sep;20(9):917-27. doi: 10.1109/42.952729., pp. 917–27. DOI: 10.1109/42.952729.

[49] Nornadiah Mohd Razali et al. "Power comparisons of shapiro-wilk, kolmogorov-smirnov, lilliefors and anderson-darling tests". In: *Journal of statistical modeling and analytics* 2.1 (2011), pp. 21–33.

[50] Min-Ho Song et al. "How fast is your body motion? Determining a sufficient frame rate for an optical motion tracking system using passive markers". In: *PloS one* 11.3 (2016), e0150993.

[51] Joshua S Furtado et al. "Comparative analysis of optitrack motion capture systems". In: *Advances in Motion Sensing and Control for Robotic Applications: Selected Papers from the Symposium on Mechatronics, Robotics, and Control (SMRC'18)-CSME International Congress 2018, May 27-30, 2018 Toronto, Canada*. Springer. 2019, pp. 15–31.

[52] Brainlab. *Curve — Image Guided Surgery*. Accessed: 2024-05-28. 2024. URL: https://www.brainlab.com/surgery-products/overview-platform-products/curve-image-guided-surgery/.

[53] OptiTrack. *Quick Start Guide: Precision Capture*. Accessed: 2024-05-24. 2024. URL: https://docs.optitrack.com/quick-start-guides/quick-start-guide-precision-capture.

[54] Adel Olabi et al. "Improving the accuracy of industrial robots by offline compensation of joints errors". In: *2012 IEEE International Conference on Industrial Technology*. Mar. 2012, pp. 492–497. DOI: 10.1109/ICIT.2012.6209986.

[55] Pierre Besset et al. "Advanced calibration applied to a collaborative robot". In: *2016 IEEE International Power Electronics and Motion Control Conference (PEMC)*. Sept. 2016, pp. 662–667. DOI: 10.1109/EPEPEMC.2016.7752073.

[56] M Salerno et al. "Magnetic and inertial sensor fusion for the localization of endoluminal diagnostic devices". In: *Int. J. Comput. Assist. Radiol. Surgery (CARS)* 7.S1 (2012), pp. 229–235.

[57] Sundeep Rawal et al. "Robotic-Assisted Prosthetically Driven Planning and Immediate Placement of a Dental Implant." In: *Compendium of Continuing Education in Dentistry (15488578)* 41.1 (2020).

[58] Huzefa S Talib et al. "Flapless dental implant placement using a recently developed haptic robotic system". In: *British Journal of Oral and Maxillofacial Surgery* 60.9 (2022), pp. 1273–1275.

[59] RoboDK. *Robot Validation - ISO 9283*. Accessed: 2024-05-27. 2024. URL: https://robodk.com/doc/en/Robot-Validation-ISO9283.html.

[60] Bojan Jerbić et al. "35 - RONNA G4—Robotic Neuronavigation: A Novel Robotic Navigation Device for Stereotactic Neurosurgery". In: *Handbook of Robotic and Image-Guided Surgery*. Ed. by Mohammad H. Abedin-Nasab. Elsevier, 2020, pp. 599–625. DOI: https://doi.org/10.1016/B978-0-12-814245-5.00035-9. URL: https://www.sciencedirect.com/science/article/pii/B9780128142455000359.

A

Systematic Review Surgical Robotic Navigation in the Human Skull

This section is a short summary of the review search strategy, data extraction and its preliminary findings. To evaluate the current methods used by robotic surgical navigation systems the following research question was established:

"How do robotic surgical navigation systems navigate during surgery performed on the skull?"

Which is deconstructed into the following sub-questions:

- *How do robotic surgical navigation systems determine and track the subject's position?*
- *How do robotic surgical navigation systems determine and track the end effector position?*
- *How is the performance of robotic surgical navigation systems reported?*

In Section A.1, the search strategy, criteria, and data extraction methods are discussed. The results of this review are presented in Section A.2 and discussed in Section A.3. This appendix provides a short summary of some preliminary interesting findings made during the review but does not represent the article intended for publication. For specific details on the papers, additional references are included in this appendix.

A.1. Materials and Methods

A.1.1. Information sources and search strategy

This review was structured according to guidelines from the Preferred Reporting Items for Systematic Reviews (PRISMA) and the Joanna Briggs Institute (JBI). The bibliographic databases Medline (through PubMed), Embase, and Scopus were searched on 18 december 2023. The search strategies for each database were carefully designed in collaboration with a search specialist (FJ). Additionally, reference lists of included full texts and previously excluded reviews were examined for further relevant studies. An overview of the search strategy for all three databases can be found in Table A.2, Table A.1, and Table A.3.

	Embase Search Terms
#1	(TITLE-ABS-KEY (robot*))
#2	(TITLE-ABS-KEY ((surge*) AND (skull OR mouth OR ear OR ears OR nose OR eye OR eyes OR maxilla OR mandible OR zygoma OR ”frontal bone” OR ”occipital bone” OR ”parietal bone” OR ”temporal bone” OR ”sphenoid bone” OR ”ethmoid bone” OR ”skull base” OR orbit* OR ”nasal bone” OR jaw OR mastoid OR head OR cranium OR cranial OR brain)) OR neurosurg* OR neuro-surg* OR ophthalmolog* OR otorhinolaryngolog* OR otolaryngolog* OR maxillofacial* OR ”maxillo facial*” OR orthognath* OR dentist* OR ent OR ”ear nose and throat”))
#3	(TITLE-ABS-KEY (collaborative OR interact* OR active* OR automatic* OR autonomous* OR manipulat* OR cobot OR complian* OR semi-autonomous* OR impedance OR navigat* OR track* OR ”dynamic guid*” OR ”image-guid*” OR haptic OR stereotax* OR stereotac*))
#4	LIMIT-TO (DOCTYPE ”ar”)

Table A.1: Embase Search Strategy, number of articles found 2060.

	Pubmed Search Terms
#1	”Robotic Surgical Procedures”[Mesh] OR ”Robotics”[Mesh] OR robot*[tiab]
#2	(”Specialties Surgical”[Mesh] OR ”Surgical Procedures Operative”[Mesh] OR surge*[tiab]) AND (”Skull”[Mesh] OR ”Mouth”[Mesh] OR ”Sense Organs”[Mesh] OR ”Brain”[Mesh] OR skull[tiab] OR mouth[tiab] OR ear[tiab] OR ears[tiab] OR nose[tiab] OR eye[tiab] OR eyes[tiab] OR maxilla[tiab] OR mandible[tiab] OR zygoma[tiab] OR frontal bone[tiab] OR occipital bone[tiab] OR parietal bone[tiab] OR temporal bone[tiab] OR sphenoid bone[tiab] OR ethmoid bone[tiab] OR skull base[tiab] OR orbit*[tiab] OR nasal bone[tiab] OR jaw[tiab] OR mastoid[tiab] OR head[tiab] OR cranium[tiab] OR cranial[tiab] OR brain[tiab])
#3	Neurosurgical Procedures”[Mesh] OR ”Ophthalmologic Surgical Procedures”[Mesh] OR ”Otorhinolaryngologic Surgical Procedures”[Mesh] OR ”Dentistry”[Mesh] OR neurosurg*[tiab] OR neuro-surg*[tiab] OR ophthalmolog*[tiab] OR otorhinolaryngolog*[tiab] OR otolaryngolog*[tiab] OR maxillofacial*[tiab] OR maxillo facial*[tiab] OR orthognath*[tiab] OR dentist*[tiab] OR ENT[tiab] OR ”ear nose and throat”[tiab]
#4	#2 OR #3
#5	”Surgical Navigation Systems”[Mesh] OR collaborative[tiab] OR interact*[tiab] OR active*[tiab] OR automatic*[tiab] OR autonomous*[tiab] OR manipulat*[tiab] OR cobot[tiab] OR complian*[tiab] OR semi-autonomous*[tiab] OR impedance[tiab] OR navigat*[tiab] OR track*[tiab] OR dynamic guid*[tiab] OR image-guid*[tiab] OR haptic[tiab] OR stereotax*[tiab] OR stereotac*[tiab]
#6	#1 AND #4 AND #5
#7	”Review” [Publication Type] OR ”Meta-Analysis” [Publication Type] OR ”Systematic Review” [Publication Type] OR ”Letter” [Publication Type] OR ”Comment” [Publication Type] OR ”Editorial” [Publication Type] OR letter[ti] OR editorial[ti] OR comment*[ti] OR systematic review[ti] OR meta-anal*[ti] OR metaanal*[ti]
#8	#6 NOT #7
#9	”Spine”[Mesh] OR ”Laparoscopy”[Mesh] OR laparoscop*[tiab]
#10	#8 NOT #9

Table A.2: Pubmed Search Strategy, number of articles found 1751.

	Scopus Search Terms
#1	exp robot assisted surgery/ OR exp robotics/ OR robot*.tiabkf.
#2	(exp surgery/ OR surge*.tiabkf.) AND (exp skull/ OR exp mouth/ OR sense organ/ OR exp brain/ OR (skull OR mouth OR ear OR ears OR nose OR eye OR eyes OR maxilla OR mandible OR zygoma OR frontal bone OR occipital bone OR parietal bone OR temporal bone OR sphenoid bone OR ethmoid bone OR skull base OR orbit* OR nasal bone OR jaw OR mastoid OR head OR cranium OR cranial OR brain).tiabkf.)
#3	exp neurosurgery/ OR exp eye surgery/ OR exp ear nose throat surgery/ OR exp dentistry/ OR (neurosurg* OR neuro-surg* OR ophthalmolog* OR otorhinolaryngolog* OR otolaryngolog* OR maxillofacial* OR maxillo facial* OR orthognath* OR dentist* OR ENT OR "ear nose and throat").tiabkf.
#4	#2 OR #3
#5	exp surgical navigation system/ OR (collaborative OR interact* OR active* OR automatic* OR autonomous* OR manipulat* OR cobot OR complian* OR semi-autonomous* OR impedance OR navigat* OR track* OR dynamic guid* OR image-guid* OR haptic OR stereotax* OR stereotac*).tiabkf.
#6	#1 AND #4 AND #5
#7	exp "review"/ OR "systematic review"/ OR exp meta analysis/ OR letter/ OR editorial/ OR note/ OR (letter OR comment* OR editorial OR systematic review OR meta-anal* OR metaanal*).ti.
#8	#6 NOT #7
#9	exp spine/ OR exp laparoscopy/ OR laparoscop*.tiabkf.
#10	#8 NOT #9

Table A.3: Scopus Search Strategy, number of articles found 2141.

A.1.2. Eligibility Criteria

For this review, a clear set of eligibility criteria was established to determine which articles would be included. The term "robot" was defined according to each author's designation in their study. If the technology was explicitly referred to as a robot in the text, it was deemed suitable. Furthermore, the robotic system had to employ a method of surgical navigation. While surgical navigation is a broad term, in this review it was defined as: a system where 3D pre-operative imaging of a patient, the location of the patient, and the location of a surgical tool are combined into real-time spatial information. In a robotic surgical navigation system, the surgical tool is (attached to) the end-effector of the robot; therefore, the robot must have a clearly defined end-effector.

The anatomical region of interest was defined as the skull (both the neurocranium and the viscerocranium) [1]. Robotic systems interacting with the soft tissue in and around the skull were also included, with the notable exceptions of brain surgery and ocular surgery. These fields have developed robotic systems with very specific characteristics that are not suitable for surgery on the rest of the skull [2] [3].

Any study describing the use of a robot in surgery using surgical navigation with an end-effector working within the skull was deemed eligible for inclusion. Articles that did not feature robotic systems, did not feature surgical navigation, or focused on a different anatomical area than the skull were excluded. Robotic systems working on the eye and brain were also excluded. Only publications available in full text were considered; abstracts, technical notes, and conference papers were excluded. Articles had to be in English; all other languages were excluded. Publications that had been retracted or were duplicates of already included studies were also excluded to maintain data integrity. These criteria are summarized in Table A.4.

Inclusion Criteria	Exclusion Criteria
Robot with end-effector	No robot used
Navigation used *	No end-effector present on the robot
Location in or on the skull	No navigation used
Primary research	Working outside the skull
	Language other than English
	Format other than full-text article
	Full text not available
	Non-primary research
	Brain surgery
	Ocular surgery

Table A.4: Inclusion and exclusion criteria for the study. * Navigation used refers to navigation that includes 3D imaging, patient, and end-effector localization.

A.1.3. Study Selection

All articles identified using the described search strategy were imported into a web application for systematic reviews (Rayyan, Qatar Computing Research Institute, Doha, Qatar). Duplicate articles were identified and removed using an in-house application beforehand. Two independent reviewers (WM, NR) screened all titles and abstracts for relevance. The results of both reviewers were compared, and in case of disagreement, a discussion was held to reach a decision. A full-text screening was then performed, and any article without a full-text version available was excluded. The reference lists of included articles were screened for additional articles matching the inclusion criteria.

A.1.4. Data Extraction

The following features were extracted: type of research, level of autonomy, Technology Readiness Level (TRL), name of the robot system, name of the robotic arm, navigation system used for subject tracking, navigation system used for end-effector tracking, method of subject tracking, method of end-effector tracking, subject used, subject fixation, reported errors on system performance, and navigation speed.

A modified classification of study types in medical research was used to describe the type of research, as depicted in Table A.5. The TRL was estimated using the descriptions from the National Aeronautics and Space Administration (NASA), consisting of 9 stages and 4 groups of development levels in which technology can be categorized as shown in Table A.7. Data registration and analysis were performed using Microsoft Office Excel (version 2019, Microsoft Corporation, USA). Finally, the level of autonomy was evaluated based on the description by Yang et al. [4], which is based on the levels defined by the Society of Automotive Engineers (SAE) [5].

Figure A.1 illustrates the five levels of autonomy in robotic surgery, interpreted from the SAE levels of driving automation. At Level 0, there is no autonomy, and the operator performs all tasks, including monitoring, generating performance options, selecting the option, and executing the decision, without any robotic assistance. At Level 1, the robot provides assistance in specific tasks while the operator maintains continuous control. At Level 2, task autonomy is introduced where the robot can perform specific, operator-initiated tasks autonomously, reducing the need for direct control by the operator. At Level 3, the system reaches conditional autonomy; the operator selects and approves a surgical plan, and the robot executes the procedure autonomously but under the supervision of a qualified operator who can intervene if necessary. Level 4 represents high autonomy, where the robot can make decisions and execute tasks independently, with the operator in a supervisory role, not needing to intervene during the procedure. Finally, at Level 5, full autonomy is achieved, with the robot capable of performing the entire surgery without any human intervention. This framework provides a comprehensive assessment of the progression from full human control to complete robotic autonomy in surgical applications.

Figure A.1: Different levels of autonomy in robotic surgery as presented by Yang et al. [4], based on the SAE levels of driving automation.

Main classification of study design	**Examples**
Basic research – theoretical	Method development (no experiments) Experiments on models, animals, cadavers, or humans
Basic research – applied	Material development
Clinical research – observational	Therapy study, case series, case reports, prognostic studies
Clinical research – experimental	Clinical intervention studies Case control studies
Epidemiological research – observational	Observational studies Comparative studies
Epidemiological research – experimental	Field/group studies

Table A.5: Main classification of study design and examples.

Group	Technology readiness levels	Description
Discovery	TRL 1	Basic principles of the technology are observed.
	TRL 2	Technological concept is formulated.
	TRL 3	After laboratory tests a proof of concept is made.
Development	TRL 4	Proof of concept is validated in laboratory with prototypes.
	TRL 5	Technology is tested and validated in the relevant environment.
	TRL 6	Technology is demonstrated in relevant environment; the prototype is not yet optimized for operational environment.
	TRL 7	Technology is integrated in operational environment.
Demonstration	TRL 8	The system is completed and qualified; the technology performs properly.
Deployment	TRL 9	Actual system is proven in operational environment; technology is commercially ready.

Table A.6: Technology Readiness Levels (TRL) and their descriptions.

A.2. Results

A.2.1. Study Selection

A total of 3,722 articles were identified as eligible for title and abstract screening, after excluding duplicates. From this, 296 articles were considered for inclusion. During the full-text screening, 145 articles were excluded for reasons specified in Figure A.2. An additional 7 articles were found through reference lists, resulting in a total of 158 articles included in this review.

A.2.2. Type of Research, Level of Autonomy, Technical Readiness Level

The results for the type of research are shown in Table A.7, the level of autonomy in Table A.8, and the Technical Readiness Level (TRL) in Table A.6.

Most of the articles described basic applied research (65%), while the remaining articles were clinical research (35%). No theoretical or epidemiological research was found.

In 35 articles, the authors could not determine the level of autonomy of the robot system based on the description of the system and workflow. Most robot systems were classified as having task autonomy (42%), while only 11% could be considered to have conditional autonomy. 10% was considered level 0, demonstrating no autonomous capabilities and 11% could only assists in actions of the surgeon. These results are shown in A.8. No higher levels of autonomy were reported.

The technological readiness level of all described robot systems was estimated, and the results are summarized in Table A.6. In 32 articles (20.3%), a commercially available robot system (TRL 9) was described. The majority of the described systems were below TRL 7 and therefore not tested in an operational environment. Specifically, 34.8% of systems were estimated to have a TRL of 4, 6.9% a TRL of 5, and 11.4% a TRL of 6.

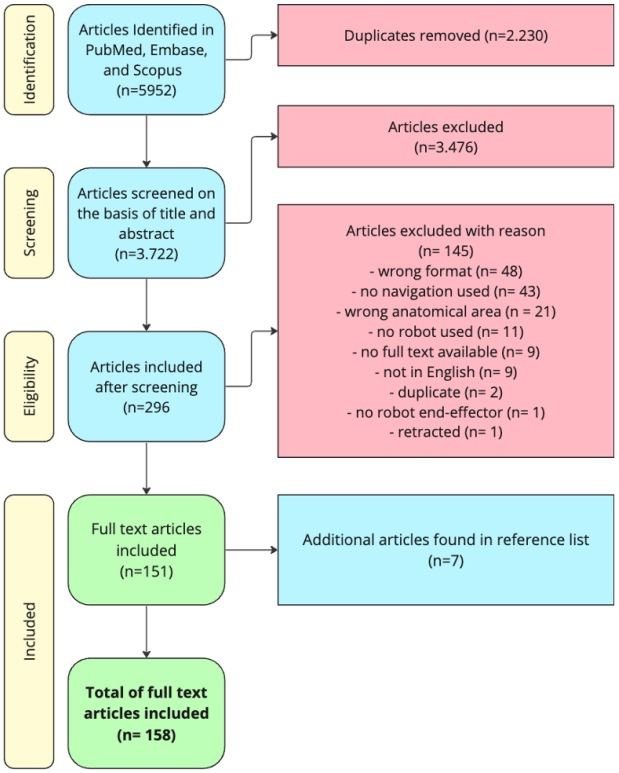

Figure A.2: Diagram of the search process and resulting included items.

Type of research	Number of articles
Non specifiable/other	0
Basic research - theoretical	0
Basic research - applied	101
Clinical research - observational	12 [6, 7, 8, 9, 10, 11, 12, 13, 14, 15, 16, 17]
Clinical research - experimental	45
Epidemiological research - observational	0
Epidemiological research - experimental	0
Total	**158**

Table A.7: Summary of types of research.

Level of autonomy	Number of articles
level 0 no automation	16
level 1 robots assistance	17
Level 2 task autonomy	71
Level 3 Conditional autonomy	18
Level 4 High autonomy	0
Level 5 full autonomy	0
Not reported/not reconstructable	35
Multiple robots, different levels (1/2/3)	1[18]
Total	**158**

Table A.8: Summary of levels of autonomy.

TRL	Number of articles
0	Not reconstructable (0)
TRL 1	0
TRL 2	0
TRL 3	4
TRL 4	55
TRL 5	29
TRL 6	11
TRL 7	18
TRL 8	9
TRL 9	32

Table A.9: TRL-scores of different systems.

Robotsystems, robot arms and subjects used

In Table A.10 the robot systems are presented, Table A.11 shows the type of robotic manipulator employed in the research. In total, 29 different robot systems were described. In 58 papers (36.7%) the robot system was assembled by the authors, while in 22 papers (13.9%) the authors build a new robot or used a robot previously build by the authors. In 16 papers (10.1%) the name of the robot system was unclear. 55 of the articles (34.8%) describe robot systems used on humans, either awake or under general anesthesia. In the other articles 43 (28.8%) used a plastic skull, 35 (26.3%) used an animal or human cadaver, 11 (6.6%) used animals either awake or under general anesthesia. The subject was fixated in 91 papers (56.6%), in 3 papers (1.9%) the robot was directly attached to the robot and in 1 paper (0.6%) the subject was not fixated. In the remaining 63 papers (39.8%) it was unclear whether the subject was fixated.

Name of robot system	Number of references
Not reported	34
Assembled by authors	59
Cyberknife	20
Remebot	8 [19, 20, 21, 22, 23, 24, 25, 26]
HEARO	8 [27, 28, 29, 30, 31, 32, 33, 34]
CARLO	6 [35, 36, 37, 38, 39, 40]
Yomi	4 [41, 42, 43, 44]
CMF-robot system	3 [45, 46, 47]
RobOtol	3 [48, 49, 50]
ADIR	2 [9, 51]
THETA	2 [52, 53]
HRCDIS	2 [54, 55]
RobaCKa	2 [56, 57]
CRANIO	2 [58, 59]
HRS-DIS (is not the same as HRCDIS)	2 [60, 61]
CARLO primo+	2 [62, 63]
A73	2 [64, 65]
Otto	1 [66]
RONAF	1 [67]
Pathfinder	1 [68]
TMR-MRS	1 [69]
Languye	1 [70]
auditory implant manipulator	1 [71]
RM200	1 [72]
ROBIN	1 [73]
ROSA	1 [74]
sa-RASS	1 [75]
Remebot + Dentrobot + Yekebot	1 [18]
Hyperarc (HA) & cyberknife	1 [76]
Maxillofacial Surgical Robotic System (MSRS)	1 [77]

Table A.10: Summary of robot systems used.

Name of robot arm	Number of references
Not reported, commercially available robot system	39
Not reported	34
Assembled by authors	22
The Fifth Generation Robots of Universal Robots (prototype)	9 [54, 55, 78, 79, 80, 77, 81, 23, 82]
KUKA Lightweight medical grade robot (LBR Med)	6 [35, 37, 38, 39, 40, 83]
DaVinci	5 [84, 85, 86, 87, 88]
KUKA iiwa800	5 [89, 90, 91, 92, 93]
KUKA lightweight robot LWR4+	4 [36, 94, 95, 96]
Cyborg-lab	3 [97, 98]
C8L Epson robots, Long Beach CA	3 [45, 46, 47]
CRIGOS	2 [58, 59]
Mitsubishi RV-1a	2 [64, 65]
KUKA LWR	2 [99, 100]
Cobot model 3, universal robots	2 [70, 53]
Universal Robot	2 [101, 102]
UR 3	1 [52]
iSYS-1	1 [103]
KUKA KR3 and Mitsubishi RV-3S	1 [104]
Mitsubishi RV-3S	1 [105]
Staubli Tx 40	1 [106]
UR10	1 [107]
IBM 7576	1 [108]
MRSMR	1 [109]
CPSR-1 surgical robot	1 [110]
KUKA (undefined which arm)	1 [111]
Staubli RX90CR	1 [112]
AdeptSix 300	1 [73]
KUKA KR3	1 [66]
MELFA RV-3S, Mitsubishi	1 [69]
KUKA lightweight medical grade Robot (LBR iiwa)	1 [59]
Staubli RX90	1 [67]
CASPAR (integrated in RobaCKA)	1 [57]
MSS SurgiScope robot (ELEKTA)	1 [113]

Table A.11: Summary of robot arms used.

Subjects of study

Figure A.3 visualizes the subjects studied in the included articles. The largest group, comprising 27% of the subjects, consists of models of the head or parts of the head, made from either plastic or plaster. Other significant groups include humans operated under general anesthesia (27%), human cadaver heads (20%), and humans who were awake during the procedure (13%).

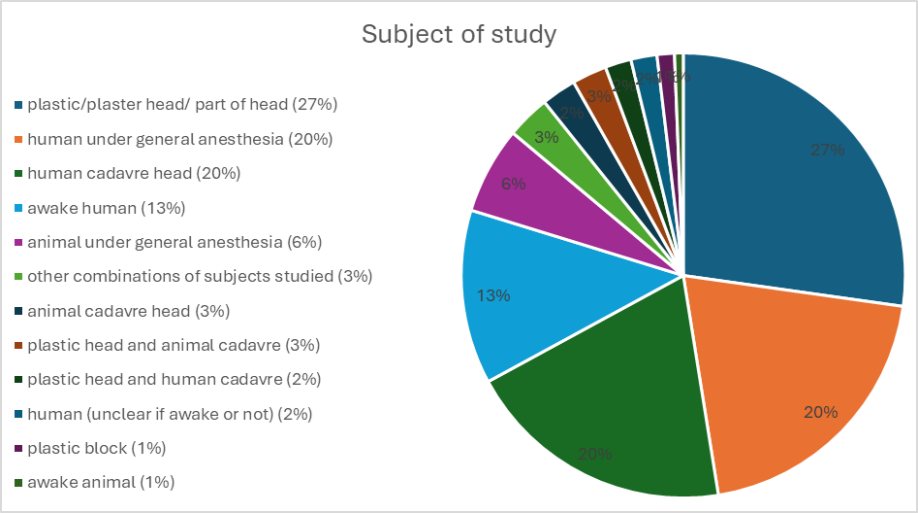

Figure A.3: Pie chart showing the distribution of different subjects studied in the included articles.

Subject Fixation

The fixation of the subject was considered ”fixated” if this was explicitly stated in the text or if the fixation was clearly visible in a photograph or figure demonstrating the setup. This was reported in 57% of the studies. If the absence of fixation was clearly described or if the authors described moving the subject, it was considered ”not fixated,” which was reported in 1% of the studies. Another 3% described a robot directly attached to the subject, leaving 40% of studies without a clear record of subject fixation. These findings are illustrated in Figure A.4.

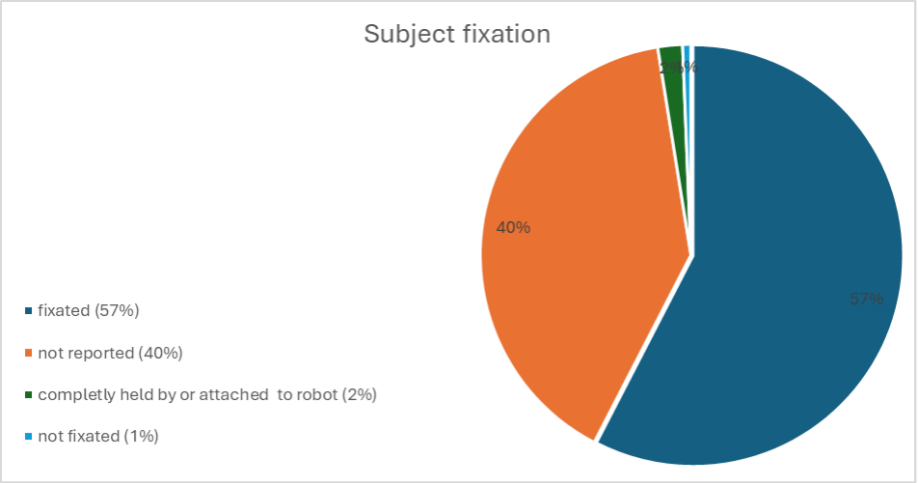

Figure A.4: Pie chart showing the reporting on the fixation methods used for subjects in the included studies.

Navigation of Subject and End-Effector

The most commonly used tracking method for both the subject and the end-effector is an optical tracking system, utilized in 46% and 43% of cases, respectively. Electromagnetic tracking was used in only 2% of subject tracking and 8% of end-effector tracking. Internal coordination of the robot arm was used for tracking the end-effector in 10% of cases, while in 4% of cases, the subject was tracked with a mechanical arm. The tracking method used for subject tracking and end-effector tracking was unreported in 25% and 33% of cases, respectively. These findings are visualized in Figures A.5 and A.6.

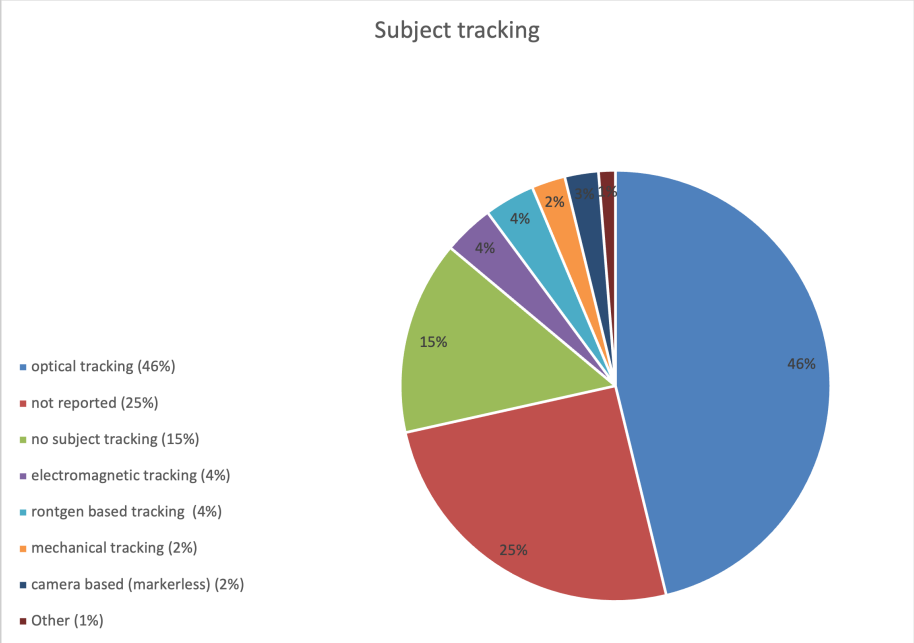

Figure A.5: Pie chart showing the distribution of different subject tracking methods reported. "Other subject tracking" includes laser-based tracking and multiple robots compared using different methods.

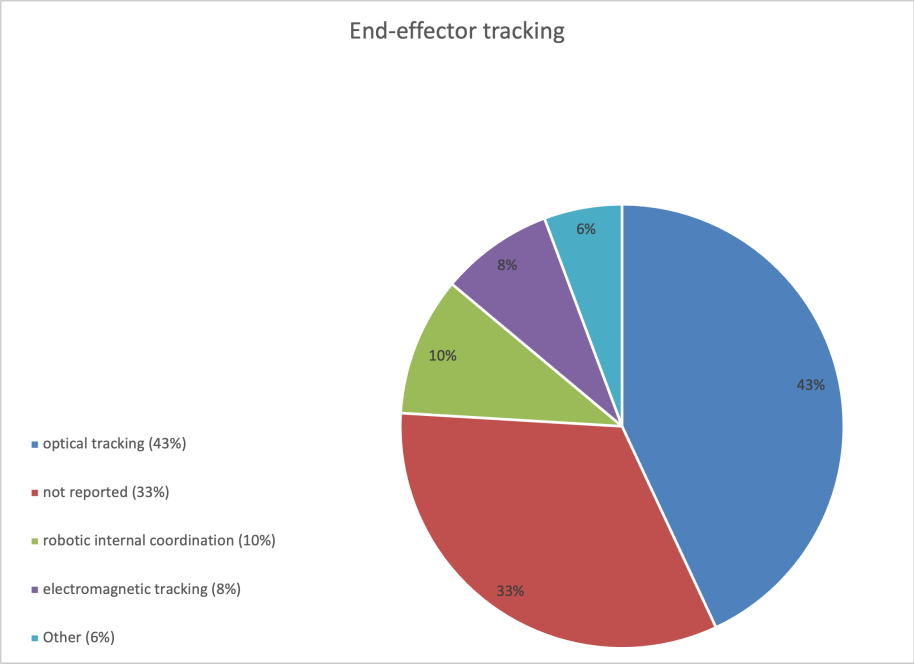

Figure A.6: Pie chart showing end-effector tracking methods reported in research. "Other" includes laser-based tracking, camera-based (markerless), mechanical tracking, sensor fusion (optical and mechanical), multiple robots compared using different methods/materials, Hall effect-based linear encoder, robotic internal coordination, and optical tracking (without sensor fusion).

Navigation Systems Used

A total of 41 different descriptions of navigation systems were identified, with considerable overlap between subject and end-effector tracking. The systems and the number of articles reporting the use of these systems are listed in Tables A.12 and A.13. For both subject and end-effector tracking, the most commonly used system was Polaris NDI.

In 67 articles (42.4%), the system used for subject tracking was unclear and therefore scored as not reported. A total of 23 articles reported not using subject tracking.

Navigation system (subject tracking)	Number of articles
not reported	67
no subject tracking	23
Polaris NDI (not specified which system)	11[101, 114, 105, 115, 56, 98, 67, 116, 66, 57, 117]
CamBar B1, Axios GmbH, Germany	6[118, 119, 120, 121, 122, 123]
part of commercially available robot system	6[44, 24, 75, 62, 31, 26]
NDI (not specified which system)	5[124, 97, 109, 102, 87]
X-spine (cyberknife)	4[6, 7, 125, 16]
POLARIS SPECTRA, Northern Digital Inc., Ontario, Canada	4[126, 46, 127, 82]
Aurora (NDI)	3[103, 128, 78]
Polaris Vicra (NDI)	3[60, 45, 47]
OPTOTRAK 3020 (NDI, Waterloo, Canada)	2[58, 71]
Micron Tracker (Claron)	2[110, 83]
camera (brand)	2[129, 130]
The FusionTrack 500 tracking camera (Atracsys)	1[51]
Cambar B2, Axios 3D, Germany	1[131]
ARTtrack2 and Polaris Spectra	1[104]
CAPPA (Cas innovations AG, Germany)	1[132]
ARTtrack2 GmbH	1[133]
RGB-D (Intel RealSense SR300)	1[91]
Polaris Vega (NDI)	1[80]
Aurora V3 (NDI)	1[77]
BeiDou-SNS navigation system V1.0.0	1[61]
Oqus, Qualisys, Gothenburg, Sweden	1[95]
FasTrak electromagnetic tracking system (Polhemus, Colchester, VT)	1[48]
Eltrotec LT-100	1[73]
Claron	1[23]
spryTrack 180, Atracsys, Switzerland	1[53]
Multiple robots compared, different methods/materials	1[18]
CAPPA ENT	1[65]
BFS-U3-32S4C-C	1[93]
Robotic arm (part of robot system)	1[43]
fusionTrack 250, Atracsys LLC	1[51]
ImageGuided PixSys 3000	1[113]

Table A.12: Summary of navigation systems used for subject tracking.

Navigation system (end effector tracking)	Number of articles
Not reported	69
Robot internal coordination	15 [134, 54, 19, 108, 90, 102, 74, 70, 64, 111, 21, 68, 135, 88, 69]
Polaris NDI	11 [101, 114, 59, 105, 115, 98, 67, 116, 136, 66, 117]
CamBar B1, Axios GmbH, Germany	7 [118, 137, 119, 120, 121, 122, 123]
Micron Tracker (Claron)	5 [89, 110, 83, 92, 138]
Polaris Vicra (NDI)	4 [107, 60, 45, 47]
FasTrak electromagnetic tracking system (Polhemus, Colchester, VT)	4 [139, 48, 49, 50]
part of commercially available robot system	4 [24, 25, 31, 26]
Aurora (NDI)	3 [103, 128, 78]
Brainlab	3 [84, 97, 87]
POLARIS SPECTRA, Northern Digital Inc., Ontario, Canada	3 [126, 46, 127]
OPTOTRAK 3020 (NDI, Waterloo, Canada)	2 [58, 71]
NDI (not specified which)	2 [124, 109]
Polaris Vega (NDI)	2 [80, 22]
Oqus, Qualisys, Gothenburg, Sweden	2 [95, 82]
Camera (brand)	2 [129, 130]
The FusionTrack 500 tracking camera (Atracsys)	1 [35]
Cambar B2, Axios 3D, Germany	1 [131]
ARTtrack2 (Gmbh, Germany) and Polaris Spectra (NDI)	1 [104]
CAPPA (Cas innovations AG, Germany)	1 [132]
Leica Laser Tracker LTD800 (Leica Geosystems, Switzerland)	1 [96]
ARTtrack2 GmbH	1 [133]
IRIS-100 EPED inc. Kaohsiun City Taiwan	1 [79]
RGB-D (Intel RealSense SR300)	1 [91]
Aurora V3 (NDI)	1 [77]
BeiDou-SNS navigation system V1.0.0	1 [61]
Fiagon Tracey Navigation System (Fiagon GmBH, Hennigsdorf, Germany)	1 [85]
TRACKER Position Sensor (New Scale Technologies, Victor, NY)	1 [140]
Image-Guided Surgery Toolkit (IGSTK) framework	1 [141]
Claron	1 [23]
spryTrack 180, Atracsys, Switzerland	1 [53]
Multiple robots compared, different methods/materials	1 [18]
CAPPA ENT	1 [65]
BFS-U3-32S4C-C	1 [93]
Robot internal coordination en Polaris NDI (no sensorfusion)	1 [57]
ImageGuided PixSys 3000	1 [113]

Table A.13: Summary of navigation systems used for end effector tracking.

Reported Errors

In Table A.14 the reported errors of the robotic navigation system are scored. This is divided in 4 categories defined by Widman et al. [142] The technical error of the robot arm was rarely reported, 95.5% of articles did not clearly report this. The registration error was unclear in 83.5% of the papers, in 2.5% it was reported with a reference and in 1.3% it was reported without reference. In 12.7% it was reported as a result of the experiment described in the

paper. The technical error of the navigation system was not clearly reported in 78.4%. The application error was reported in 70.9%, making this the most reported error.

Reported error	Technical Error Robot Arm	Technical Error Navigation System	Registration Error	Application Error
not reported/unclear	151	124	132	46
reported without reference	4	21	2	1
reported with reference to manufacturer reports	0	0	0	0
reported with reference to an article	2	3	4	6
reported as result of experiment	0	9	20	96
reported with reference to earlier article & reported as result of experiment	0	0	0	9
reported with ISO number	1	0	0	0
reported without reference & reported as result of experiment	0	1	0	0

Table A.14: Summary of reported errors in various categories.

Types of technical error navigation system

The technical error of the navigation system was reported in 34 of articles (21.5%). In these articles 21 different definitions were used as seen in Table A.15. 17 of these definitions were only used once.

Definition of technical error navigation system	Number of articles
without definition	5[105, 108, 70, 39, 122]
(TVA) Tracking volume accuracy (RMS)	4[35, 131, 104, 120]
spatial accuracy	3[137, 46, 45]
positioning accuracy	4[114, 115, 107, 116]
repeat measurement accuracy and absolute measurement accuracy	2[109, 67]
back-projection error of reff. point	1[94]
absolute and relative accuracy	1[58]
position and joint accuracy	1[90]
End to end accuracy E2E	1[143]
distance error	1[127]
absolute error	1[73]
resolution	1[140]
image resolution (camera)	1[130]
repetitive positioning accuracy	1[138]
Mean position error & max position error	1[135]
Target Localisation Error (TLE)	1[88]
technical accuracy	1[66]
95% confidence interval of accuracy	1[53]
stereotactic error	1[65]
standard deviation	1[93]
positioning error	1[116]
space positioning accuracy	1[117]

Table A.15: Definition of technical error navigation system.

Type of registration error reported
In only 4.6% of all papers TRE and FRE were reported, in 3.9% only TRE was reported and in 3.9% only FRE. Other definitions that were occasionally used are: registration error, landmark registration error and registration accuracies.

Update rate
The update rate of the navigation system was reported in 20 articles (12.7%), while the majority of the studies (87.3%) did not report this. Most often the update rate was reported in Hz (9.5%). With 3 articles using Frames Per Second, 1 article using interval in milliseconds, and 1 article reporting both update rate in Hz and latency.

A.3. Discussion

The aim of this study was to describe how robotic surgical navigation systems operate during surgeries performed on the skull, providing a transparent view of the current and developing methods of robotic surgical navigation. The following research questions were formulated:

"How do robotic surgical navigation systems navigate during surgery performed on the skull?"

Which was deconstructed into the following sub-questions:

- *How do robotic surgical navigation systems determine and track the subject's position?*
- *How do robotic surgical navigation systems determine and track the end effector position?*
- *How is the performance of robotic surgical navigation systems reported?*

In this review, a total of 3,722 articles eligible for title and abstract screening were identified, with 296 articles included for full-text screening, resulting in 158 studies being included. The most frequent reason for exclusion was "wrong format," accounting for 48 exclusions, most of which were congress abstracts. Often, the authors

of congress abstracts submit articles for publication in journals after further development. Therefore, many of the systems described in these abstracts are likely included in full-text articles published later. The number of exclusions due to ”no surgical navigation” was also relatively large, with 43 exclusions. This was because the description of the navigation was sometimes vague in the abstract, and upon full-text screening, it was determined that it did not meet our criteria. With a total of 158 studies included in this review, a broad evaluation of robotic surgical navigation on the skull could be conducted.

Most articles (63.9%) were classified as basic research, while 36.1% were classified as clinical research. No theoretical work was found, suggesting that authors commonly do not submit articles for publication before having built or assembled a robot system.

Robotic systems in the included studies were found to have a level of autonomy up to level 3, with no higher levels described. Most robotic systems were found to have level 2: task autonomy (42%), while only a small portion was found to have level 3: conditional autonomy (11%). Given the many possible variables and disrupting factors in surgery, the authors do not suspect that higher levels of autonomy will be achieved in this field in the near future. In 35 articles (22.2%), the level of autonomy could not be determined based on the described functions of the robotic system. Without insight into the functions and the level of autonomy, both the benefits and risks of a robotic system cannot be properly understood.

In this review, a TRL (Technology Readiness Level) ranging from 3 to 9 was found. TRL 4 was the largest group, consisting of 34.8% of all papers. Only four commercially available navigating surgical robots (TRL 9) were found: Cyberknife, Yomi, Rosa, and Remebot [74]. Cyberknife is utilized in various anatomical regions and Rosa is employed in neurosurgery. Because of the anatomical exclusion criteria, most of the articles published on these systems were not included in this review. Both Yomi and Remebot are used in dental implant surgery, so all publications about these systems should fall within the scope of this review. Remarkably, although 25.3% of the total number of articles focused on these commercially available systems, only four articles (2.53%) described the Yomi robotic system, all of which involved clinical experiments. Even more concerning is that none of these four articles referenced earlier studies on the performance of the Yomi robotic system. Additionally, the working mechanism of the mechanical tracking arm used in this system remains unclear in these studies, a concern previously reported by other authors. Existing studies on the Yomi system show a mean and standard deviation of 1.04 ± 0.70 mm of coronal deviation in application error, with a maximum value of 3.86 mm [41]. The absence of any studies reporting the technical and registration performance of the navigation system makes it unclear whether this maximum value is due to clinical errors or the system itself. While the existing studies may suggest acceptable levels of application accuracy and the system ensures that the surgeon remains in control of the surgery, the existence of a commercially available robotic system operating in direct contact with human patients without clear reports on its working mechanisms and with little scientific substantiation should be considered alarming.

A total of 29 different robotic systems and 30 robot arms were identified. In Table A.10, it is clear that many of these systems and robot arms have only been described once or twice. This indicates either a newly developed system or an arrested development. Moreover, 22 studies assembled a new robotic system, and 21 studies describe a robot arm built by the authors themselves. It is clear that there is great interest in researching robots using surgical navigation, yet no universal way of reporting on these systems can be found.

Most of the navigation systems for both subject and end-effector tracking used optical tracking (46% and 43%, respectively), while mechanical tracking and electromagnetic tracking are sparsely used. In a large number of articles, no clear report on the method of tracking could be identified for both subject and end-effector tracking (25% and 33%, respectively). Moreover, the majority of the articles do not report the navigation system used for tracking either the subject or the end-effector. If the navigation system is reported, one system is most often used for both subject and end-effector tracking, explaining the similarities between Table A.12 and Table A.13. The most reported navigation system is ”Polaris NDI.” However, NDI is a company with different optical systems all starting with ”Polaris” (Lyra, Vicra, Vega ST, Vega VT, and Vega XT). Each of these systems has distinctly different performance characteristics reported by the manufacturer. This makes the performance characteristics of the navigation system used unclear, especially since their technical error and update rate are rarely reported. Also, other optical tracking systems by NDI were reported; these are no longer commercially available and are no longer published on the manufacturer’s site (Optotrak, Polaris Spectra). Even with the full name and manufacturer reported, it is now no longer possible to easily find the manufacturer-reported performance characteristics. This reinforces the need for a complete and transparent report of the systems used and the corresponding performance measures.

From the included studies, 57% reported that the subject was fixated during the experiments, while 40% did not provide information about subject fixation. The movement of the subject can have a considerable impact on both

the navigation system and the robotic system employed. The robotic system needs to respond to the movement, which may present challenges related to latency. In optical tracking systems, the angle at which the dynamic reference frame is viewed by the camera can affect the overall performance of the navigation. Therefore, it is not sufficient to test the registration performance of the system solely in static, controlled environments, as this does not accurately reflect the dynamic conditions that may be encountered in practical applications.

The performance of the robotic system as a whole, measured by the application error, was reported in most articles (71.1%). Most frequently, it was reported as the result of experiments described in the study (66.7%), while 9.4% of the studies reported an application error described in earlier research. The application error is clinically most relevant and is therefore essential information for any robotic system. However, to better understand the performance and potential error of the robotic system, additional information about the different components and registration is necessary. The technical error of the robot arm, the technical error of the navigation system, and the registration error were not reported in most articles (95.5%, 83.6%, and 79.2%, respectively). Moreover, the technical error of the navigation system was reported with 21 different definitions. For those without a technical background, it can be difficult to understand these terms, let alone compare different systems. A clear and transparent way of reporting on robotic surgical navigation systems is lacking and should be constructed in future endeavors.

Limitations
While this review was conducted with detailed and systematic methods, there are certain limitations. Although our broad search terms generated many articles, it is possible that some were missed. Variations in how surgical navigation robots are described over time and across different medical specialties may have contributed to this. However, given the high number of included studies, the authors believe that a small number of missed articles would not significantly alter the review's results.

Additionally, the assessment of the autonomy level and Technical Readiness Level was based on the information provided in the papers. In some cases, the information was limited, which might have led to misjudgments of these levels. Furthermore, despite clear descriptions of these levels, differences in interpretation could lead to minor discrepancies.

Finally, several areas of interest within robotic surgical navigation in the human skull were not reviewed in this study, such as registration methods, imaging errors, and the use of software. Due to the abundance of available information, the authors focused on providing a clear overview of the hardware and performance of robotic surgical navigation systems. Additional research could yield more valuable insights into these areas.

References Systematic Review

[1] Bradley W Anderson et al. “Anatomy, head and neck, skull”. In: (2018).

[2] Roomasa Channa et al. “Robotic vitreoretinal surgery”. In: *Retina* 37.7 (2017), pp. 1220–1228.

[3] Rami Elsabeh et al. “Cranial neurosurgical robotics”. In: *British journal of neurosurgery* 35.5 (2021), pp. 532–540.

[4] Guang-Zhong Yang et al. *Medical robotics—Regulatory, ethical, and legal considerations for increasing levels of autonomy*. 2017.

[5] On-Road Automated Driving (ORAD) Committee. *Taxonomy and Definitions for Terms Related to Driving Automation Systems for On-Road Motor Vehicles*. SAE International, 2021.

[6] F. Crop et al. “Treatment and technical intervention time analysis of a robotic stereotactic radiotherapy system”. In: *Technol Cancer Res Treat* 13.1 (2014), pp. 29–35. DOI: doi:http://dx.doi.org/10.7785/tcrt.2012.500359.

[7] I. Desideri et al. “Efficacy and Tolerability of CyberKnife Stereotactic Robotic Radiotherapy for Primary or Secondary Orbital Lesions: A Single-Center Retrospective Experience”. In: *Technol Cancer Res Treat* 18 (2019), p. 1533033818818561. DOI: doi:http://dx.doi.org/10.1177/1533033818818561.

[8] G. Guler Avci et al. “Robotic stereotactic radiotherapy results and treatment compliance of patients aged 65 and over”. In: *Turkiye Klinikleri Journal of Medical Sciences* 33.5 (2013), pp. 1302–1307. DOI: doi:http://dx.doi.org/10.5336/medsci.2013-33897. URL: http://www.turkiyeklinikleri.com/pdf/?pdf=89c96324a5f270af828e281a5d629a8chttp://ovidsp.ovid.com/ovidweb.cgi?T=JS&PAGE=reference&D=emed14&NEWS=N&AN=370329489.

[9] S. Jia et al. “Accuracy of an autonomous dental implant robotic system versus static guide-assisted implant surgery: A retrospective clinical study”. In: *J Prosthet Dent* (2023). DOI: doi:http://dx.doi.org/10.1016/j.prosdent.2023.04.027.

[10] G. Ozyigit et al. “Robotic stereotactic radiosurgery in patients with nasal cavity and paranasal sinus tumors”. In: *Technol Cancer Res Treat* 13.5 (2014), pp. 409–413. DOI: doi:http://dx.doi.org/10.7785/tcrtexpress.2013.600264.

[11] G. Ozyigit et al. “A retrospective comparison of robotic stereotactic body radiotherapy and three-dimensional conformal radiotherapy for the reirradiation of locally recurrent nasopharyngeal carcinoma”. In: *Int J Radiat Oncol Biol Phys* 81.4 (2011), e263–e268. DOI: doi:http://dx.doi.org/10.1016/j.ijrobp.2011.02.054.

[12] Y. Seo et al. “Robotic system-based fractionated stereotactic radiotherapy in locally recurrent nasopharyngeal carcinoma”. In: *Radiother Oncol* 93.3 (2009), pp. 570–574. DOI: doi:http://dx.doi.org/10.1016/j.radonc.2009.10.018.

[13] İ Tosun et al. “Robotic radiosurgery of head and neck paragangliomas: a single institution experience”. In: *Asia Pac J Clin Oncol* 14.2 (2018), e3–e7. DOI: doi:http://dx.doi.org/10.1111/ajco.12695.

[14] H. Yamazaki et al. “Comparison of re-irradiation outcomes for charged particle radiotherapy and robotic stereotactic radiotherapy using cyberknife for recurrent head and neck cancers: A multi-institutional matched-cohort analysis”. In: *Anticancer Research* 36.10 (2016), pp. 5507–5514. DOI: doi:http://dx.doi.org/10.21873/anticanres.11132. URL: http://ar.iiarjournals.org/content/36/10/5507.full.pdfhttp://ovidsp.ovid.com/ovidweb.cgi?T=JS&PAGE=reference&D=emed17&NEWS=N&AN=612866854.

[15] H. Yamazaki et al. “Reirradiation using robotic image-guided stereotactic radiotherapy of recurrent head and neck cancer”. In: *J Radiat Res* 57.3 (2016), pp. 288–293. DOI: doi:http://dx.doi.org/10.1093/jrr/rrw004.

[16] F. Ehret et al. “Single-session image-guided robotic radiosurgery and quality of life for glomus jugulare tumors”. In: *Head Neck* 42.9 (2020), pp. 2421–2430. DOI: doi:https://doi.org/10.1002/hed.26231.

[17] E. Uysal et al. “Robotic stereotactic body radiotherapy for recurrent nasopharyngeal carcinoma”. In: *Indian J Cancer* 60.3 (2023), pp. 353–358. DOI: doi:https://doi.org/10.4103/ijc.ijc_1414_20.

[18] Z. Xu et al. “Accuracy and efficiency of robotic dental implant surgery with different human-robot interactions: An in vitro study”. In: *J Dent* 137 (2023), p. 104642. DOI: doi:https://doi.org/10.1016/j.jdent.2023.104642. URL: https://www.sciencedirect.com/science/article/pii/S0300571223002282?via%3Dihub.

[19] H. Deng et al. “Autonomous dental robotic surgery for zygomatic implants: A two-stage technique”. In: *J Prosthet Dent* (2023). DOI: doi:http://dx.doi.org/10.1016/j.prosdent.2023.05.033.

[20] C. Li et al. “Autonomous robotic surgery for zygomatic implant placement and immediately loaded implant-supported full-arch prosthesis: a preliminary research”. In: *Int J Implant Dent* 9.1 (2023), p. 12. DOI: doi:http://dx.doi.org/10.1186/s40729-023-00474-2.

[21] S. Yang et al. “Accuracy of autonomous robotic surgery for single-tooth implant placement: A case series”. In: *J Dent* 132 (2023), p. 104451. DOI: doi:http://dx.doi.org/10.1016/j.jdent.2023.104451.

[22] S. Yang et al. “Autonomous Robotic Surgery for Immediately Loaded Implant-Supported Maxillary Full-Arch Prosthesis: A Case Report”. In: *J Clin Med* 11.21 (2022), p. 6594. DOI: doi:http://dx.doi.org/10.3390/jcm11216594.

[23] H. Deng et al. “Semi-autonomous two-stage dental robotic technique for zygomatic implants: An in vitro study”. In: *J Dent* 138 (2023), p. 104687. DOI: doi:https://doi.org/10.1016/j.jdent.2023.104687. URL: https://www.sciencedirect.com/science/article/pii/S0300571223002737?via%3Dihub.

[24] H. Deng et al. “Feasibility and accuracy of a task-autonomous robot for zygomatic implant placement”. In: *J Prosthet Dent* (2023). DOI: doi:https://doi.org/10.1016/j.prosdent.2023.10.029. URL: https://www.sciencedirect.com/science/article/pii/S0022391323007102?via%3Dihub.

[25] M. Fanhao et al. “A new multimodal, image-guided, robot-assisted, interstitial brachytherapy for the treatment of head and neck tumors-A preliminary study”. In: *Int J Med Robot* 16.5 (2020), pp. 1–5. DOI: doi:https://doi.org/10.1002/rcs.2133.

[26] P. Li et al. “Accuracy of autonomous robotic surgery for dental implant placement in fully edentulous patients: A retrospective case series study”. In: *Clin Oral Implants Res* 34.12 (2023), pp. 1428–1437. DOI: doi:https://doi.org/10.1111/clr.14188.

[27] J. Abari et al. “True keyhole cochlear implant surgery”. In: *Am J Otolaryngol* 44.4 (2023), p. 103926. DOI: doi:http://dx.doi.org/10.1016/j.amjoto.2023.103926.

[28] M. Al Saadi et al. “Robotic cochlear implantation in post-meningitis ossified cochlea”. In: *Am J Otolaryngol* 44.1 (2023), p. 103668. DOI: doi:http://dx.doi.org/10.1016/j.amjoto.2022.103668.

[29] D. Schneider et al. “Robotic cochlear implantation: feasibility of a multiport approach in an ex vivo model”. In: *Eur Arch Otorhinolaryngol* 276.5 (2019), pp. 1283–1289. DOI: doi:http://dx.doi.org/10.1007/s00405-019-05318-7.

[30] V. Topsakal et al. “First Study in Men Evaluating a Surgical Robotic Tool Providing Autonomous Inner Ear Access for Cochlear Implantation”. In: *Front Neurol* 13 (2022), p. 804507. DOI: doi:http://dx.doi.org/10.3389/fneur.2022.804507.

[31] J. Hermann et al. “Robotic Milling of Electrode Lead Channels During Cochlear Implantation in an ex-vivo Model”. In: *Front Surg* 8 (2021), p. 742147. DOI: doi:https://doi.org/10.3389/fsurg.2021.742147. URL: https://www.ncbi.nlm.nih.gov/pmc/articles/PMC8631814/pdf/fsurg-08-742147.pdf.

[32] E. Heuninck et al. “Audiological outcomes of robot-assisted cochlear implant surgery”. In: *Eur Arch Otorhinolaryngol* 280.10 (2023), pp. 4433–4444. DOI: doi:https://doi.org/10.1007/s00405-023-07961-7. URL: https://link.springer.com/content/pdf/10.1007/s00405-023-07961-7.pdf.

[33] A. M. Tekin et al. “Evaluation of a Less Invasive Cochlear Implant Surgery in OPA1 Mutations Provoking Deafblindness”. In: *Genes (Basel)* 14.3 (2023). DOI: doi:https://doi.org/10.3390/genes14030627. URL: https://mdpi-res.com/d_attachment/genes/genes-14-00627/article_deploy/genes-14-00627.pdf?version=1677745676.

[34] A. M. Tekin et al. “A new pathogenic variant in POU3F4 causing deafness due to an incomplete partition of the cochlea paved the way for innovative surgery”. In: *Genes* 12.5 (2021), p. 613. DOI: doi:https://doi.org/10.3390/genes12050613. URL: https://www.mdpi.com/2073-4425/12/5/613/pdfhttp://ovidsp.ovid.com/ovidweb.cgi?T=JS&PAGE=reference&D=emed22&NEWS=N&AN=2007092397%20https://mdpi-res.com/d_attachment/genes/genes-12-00613/article_deploy/genes-12-00613-v2.pdf?version=1619053753.

[35] M. Augello et al. “Performing partial mandibular resection, fibula free flap reconstruction and midfacial osteotomies with a cold ablation and robot-guided Er:YAG laser osteotome (CARLO(®)) - A study on applicability and effectiveness in human cadavers”. In: *J Craniomaxillofac Surg* 46.10 (2018), pp. 1850–1855. DOI: doi:http://dx.doi.org/10.1016/j.jcms.2018.08.001.

[36] K. W. Baek et al. “Comparing the Bone Healing After Cold Ablation Robot-Guided Er:YAG Laser Osteotomy and Piezoelectric Osteotomy-A Pilot Study in a Minipig Mandible”. In: *Lasers Surg Med* 53.3 (2021), pp. 291–299. DOI: doi:http://dx.doi.org/10.1002/lsm.23281.

[37] M. Ebeling et al. “First-Hand Experience and Result with New Robot-Assisted Laser LeFort-I Osteotomy in Orthognathic Surgery: A Case Report”. In: *J Pers Med* 13.2 (2023), p. 287. DOI: doi:http://dx.doi.org/10.3390/jpm13020287.

[38] D. Holzinger et al. “First-in-man application of a cold ablation robot guided laser osteotome in midface osteotomies”. In: *J Craniomaxillofac Surg* 49.7 (2021), pp. 531–537. DOI: doi:http://dx.doi.org/10.1016/j.jcms.2021.01.007.

[39] M. Ureel et al. “Cold Ablation Robot-Guided Laser Osteotome (CARLO(®)): From Bench to Bedside”. In: *J Clin Med* 10.3 (2021), pp. 1–14. DOI: doi:http://dx.doi.org/10.3390/jcm10030450.

[40] F. Winter et al. “Navigated, Robot-Driven Laser Craniotomy for SEEG Application Using Optical Coherence Tomography in an Animal Model”. In: *Frontiers in Robotics and AI* 8 (2021). DOI: doi:http://dx.doi.org/10.3389/frobt.2021.695363. URL: https://www.scopus.com/inward/record.uri?eid=2-s2.0-85110259140&doi=10.3389%2ffrobt.2021.695363&partnerID=40&md5=a8f686b11493d8eb0e70463b5cdd4ddb.

[41] S. L. Bolding et al. “Accuracy of haptic robotic guidance of dental implant surgery for completely edentulous arches”. In: *J Prosthet Dent* 128.4 (2022), pp. 639–647. DOI: doi:http://dx.doi.org/10.1016/j.prosdent.2020.12.048.

[42] P. S. Mozer. “Accuracy and Deviation Analysis of Static and Robotic Guided Implant Surgery: A Case Study”. In: *Int J Oral Maxillofac Implants* 35.5 (2020), e86–e90. DOI: doi:http://dx.doi.org/10.11607/jomi.8231.

[43] S. Rawal et al. “Robotic-Assisted Prosthetically Driven Planning and Immediate Placement of a Dental Implant”. In: *Compend Contin Educ Dent* 41.1 (2020), 26–30, quiz 31. DOI: doi:.

[44] M. Ali. “Flapless dental implant surgery enabled by haptic robotic guidance: A case report”. In: *Clin Implant Dent Relat Res* (2023). DOI: doi:https://doi.org/10.1111/cid.13279.

[45] J. Wu et al. “Error Analysis of Robot-Assisted Orthognathic Surgery”. In: *J Craniofac Surg* 31.8 (2020), pp. 2324–2328. DOI: doi:http://dx.doi.org/10.1097/scs.0000000000006767.

[46] J. Wu et al. “The Feasibility of Robot-Assisted Chin Osteotomy on Skull Models: Comparison with Surgical Guides Technique”. In: *J Clin Med* 11.22 (2022), p. 6807. DOI: doi:http://dx.doi.org/10.3390/jcm11226807.

[47] J. Wu et al. "Collaborative Control Method and Experimental Research on Robot-Assisted Craniomaxillofacial Osteotomy Based on the Force Feedback and Optical Navigation". In: *J Craniofac Surg* 33.7 (2022), pp. 2011–2018. DOI: doi:http://dx.doi.org/10.1097/scs.0000000000008684.

[48] R. Torres et al. "Atraumatic Insertion of a Cochlear Implant Pre-Curved Electrode Array by a Robot-Automated Alignment with the Coiling Direction of the Scala Tympani". In: *Audiology and Neurotology* 27.2 (2022), pp. 148–155. DOI: doi:http://dx.doi.org/10.1159/000517398. URL: https://www.scopus.com/inward/record.uri?eid=2-s2.0-85111587463&doi=10.1159%2f000517398&partnerID=40&md5=50465c801e722004aa9aeeff70df72af.

[49] R. Torres et al. "An Optimized Robot-Based Technique for Cochlear Implantation to Reduce Array Insertion Trauma". In: *Otolaryngol Head Neck Surg* 159.5 (2018), pp. 900–907. DOI: doi:http://dx.doi.org/10.1177/0194599818792232.

[50] R. Torres et al. "Improvement of the insertion axis for cochlear implantation with a robot-based system". In: *Eur Arch Otorhinolaryngol* 274.2 (2017), pp. 715–721. DOI: doi:http://dx.doi.org/10.1007/s00405-016-4329-2.

[51] Zhiwen Li et al. "Implant placement with an autonomous dental implant robot: A clinical report". In: *The Journal of Prosthetic Dentistry* (2023). DOI: https://doi.org/10.1016/j.prosdent.2023.02.014. URL: https://www.sciencedirect.com/science/article/pii/S0022391323001245%20https://www.sciencedirect.com/science/article/pii/S0022391323001245?via%3Dihub.

[52] J. Chen et al. "Comparison the accuracy of a novel implant robot surgery and dynamic navigation system in dental implant surgery: an in vitro pilot study". In: *BMC Oral Health* 23.1 (2023), p. 179. DOI: doi:http://dx.doi.org/10.1186/s12903-023-02873-8.

[53] J. Y. Shi et al. "Improved positional accuracy of dental implant placement using a haptic and machine-vision-controlled collaborative surgery robot: A pilot randomized controlled trial". In: *J Clin Periodontol* (2023). DOI: doi:https://doi.org/10.1111/jcpe.13893.

[54] K. J. Cheng et al. "Accuracy of dental implant surgery with robotic position feedback and registration algorithm: An in-vitro study". In: *Comput Biol Med* 129 (2021), p. 104153. DOI: doi:http://dx.doi.org/10.1016/j.compbiomed.2020.104153.

[55] T. S. Kan et al. "Evaluation of a custom-designed human-robot collaboration control system for dental implant robot". In: *Int J Med Robot* 18.1 (2022), e2346. DOI: doi:http://dx.doi.org/10.1002/rcs.2346.

[56] G. Eggers et al. "Robot-assisted craniotomy". In: *Minim Invasive Neurosurg* 48.3 (2005), pp. 154–158. DOI: doi:http://dx.doi.org/10.1055/s-2005-870908.

[57] W. Korb et al. "Development and first patient trial of a surgical robot for complex trajectory milling". In: *Comput Aided Surg* 8.5 (2003). Korb, Werner Engel, Dirk Boesecke, Robert Eggers, Georg Kotrikova, Bibiana Marmulla, Rüdiger Raczkowsky, Jörg Wörn, Heinz Mühling, Joachim Hassfeld, Stefan Clinical Trial Journal Article Research Support, Non-U.S. Gov't England 2004/11/09 Comput Aided Surg. 2003;8(5):247-56. doi: 10.3109/10929080309146060., pp. 247–56. DOI: 10.3109/10929080309146060.

[58] P. Bast et al. "Robot- and computer-assisted craniotomy: resection planning, implant modelling and robot safety". In: *Int J Med Robot* 2.2 (2006), pp. 168–178. DOI: doi:http://dx.doi.org/10.1002/rcs.85.

[59] V. Cunha-Cruz et al. "Robot- and computer-assisted craniotomy (CRANIO): from active systems to synergistic man-machine interaction". In: *Proc Inst Mech Eng H* 224.3 (2010), pp. 441–452. DOI: doi:http://dx.doi.org/10.1243/09544119jeim596.

[60] B. Tao et al. "The accuracy of a novel image-guided hybrid robotic system for dental implant placement: An in vitro study". In: *Int J Med Robot* 19.1 (2023), e2452. DOI: doi:http://dx.doi.org/10.1002/rcs.2452.

[61] B. Tao et al. "Accuracy of dental implant surgery using dynamic navigation and robotic systems: An in vitro study". In: *J Dent* 123 (2022), p. 104170. DOI: doi:http://dx.doi.org/10.1016/j.jdent.2022.104170.

[62] M. Gottsauner et al. "Geometric Cuts by an Autonomous Laser Osteotome Increase Stability in Mandibular Reconstruction With Free Fibula Grafts: A Cadaver Study". In: *Journal of oral and maxillofacial surgery : official journal of the American Association of Oral and Maxillofacial Surgeons* (2023). DOI: doi:https://doi.org/10.1016/j.joms.2023.10.008. URL: http://ovidsp.ovid.com/ovidweb.cgi?T=

JS&PAGE=reference&D=emexb&NEWS=N&AN=642790053%20https://www.sciencedirect.com/science/article/pii/S0278239123012284?via%3Dihub.

[63] T. Wojcik et al. "Robotic calvarial bone sampling". In: *J Craniomaxillofac Surg* 51.10 (2023), pp. 603–608. DOI: doi:https://doi.org/10.1016/j.jcms.2023.09.004. URL: https://www.sciencedirect.com/science/article/pii/S101051822300166X?via%3Dihub.

[64] H. Steinhart et al. "Surgical application of a new robotic system for paranasal sinus surgery". In: *Annals of Otology, Rhinology and Laryngology* 113.4 (2004), pp. 303–309. DOI: doi:http://dx.doi.org/10.1177/000348940411300409. URL: https://www.scopus.com/inward/record.uri?eid=2-s2.0-4744368453&doi=10.1177%2f000348940411300409&partnerID=40&md5=b2ba6507eefb2021fc6a89d6468ecf6e.

[65] J. Wurm et al. "Increased safety in robotic paranasal sinus and skull base surgery with redundant navigation and automated registration". In: *Int J Med Robot* 1.3 (2005), pp. 42–48. DOI: doi:http://dx.doi.org/10.1002/rcs.26.

[66] O. Majdani et al. "A robot-guided minimally invasive approach for cochlear implant surgery: preliminary results of a temporal bone study". In: *Int J Comput Assist Radiol Surg* 4.5 (2009), pp. 475–486. DOI: doi:https://doi.org/10.1007/s11548-009-0360-8. URL: https://link.springer.com/content/pdf/10.1007/s11548-009-0360-8.pdf.

[67] P. J. Stolka et al. "First 3D ultrasound scanning, planning, and execution of CT-free milling interventions with a surgical robot". In: *Conference proceedings : ... Annual International Conference of the IEEE Engineering in Medicine and Biology Society. IEEE Engineering in Medicine and Biology Society. Conference* 2008 (2008), pp. 5605–5610. DOI: doi:. URL: http://ovidsp.ovid.com/ovidweb.cgi?T=JS&PAGE=reference&D=emed10&NEWS=N&AN=354567149.

[68] J. Brodie et al. "Evaluation of a neurosurgical robotic system to make accurate burr holes". In: *International Journal of Medical Robotics and Computer Assisted Surgery* 7.1 (2011), pp. 101–106. DOI: doi:https://doi.org/10.1002/rcs.376. URL: http://ovidsp.ovid.com/ovidweb.cgi?T=JS&PAGE=reference&D=emed12&NEWS=N&AN=361306743.

[69] X. Sun et al. "Automated dental implantation using image-guided robotics: registration results". In: *Int J Comput Assist Radiol Surg* 6.5 (2011), pp. 627–634. DOI: doi:https://doi.org/10.1007/s11548-010-0543-3. URL: https://link.springer.com/content/pdf/10.1007/s11548-010-0543-3.pdf.

[70] S. C. Qiao et al. "Accuracy and safety of a haptic operated and machine vision controlled collaborative robot for dental implant placement: A translational study". In: *Clin Oral Implants Res* 34.8 (2023), pp. 839–849. DOI: doi:http://dx.doi.org/10.1111/clr.14112.

[71] C. Stieger et al. "Development of an auditory implant manipulator for minimally invasive surgical insertion of implantable hearing devices". In: *J Laryngol Otol* 125.3 (2011), pp. 262–270. DOI: doi:http://dx.doi.org/10.1017/s0022215110002185.

[72] J. J. Han et al. "Accurate Mandible Reconstruction by Mixed Reality, 3D Printing, and Robotic-Assisted Navigation Integration". In: *J Craniofac Surg* 33.6 (2022), e701–e706. DOI: doi:http://dx.doi.org/10.1097/scs.0000000000008603.

[73] D. Malthan et al. "Automated registration of partially defective surfaces by local landmark identification". In: *Comput Aided Surg* 8.6 (2003), pp. 300–309. DOI: doi:http://dx.doi.org/10.3109/10929080309146068.

[74] M. Olivetto et al. "Zygomatic implant placement using a robot-assisted flapless protocol: proof of concept". In: *Int J Oral Maxillofac Surg* 52.6 (2023), pp. 710–715. DOI: doi:http://dx.doi.org/10.1016/j.ijom.2022.12.002.

[75] Y. Ding et al. "Accuracy of a novel semi-autonomous robotic-assisted surgery system for single implant placement: A case series". In: *Journal of Dentistry* 139 (2023), p. 104766. DOI: doi:https://doi.org/10.1016/j.jdent.2023.104766. URL: https://www.scopus.com/inward/record.uri?eid=2-s2.0-85175821109&doi=10.1016%2fj.jdent.2023.104766&partnerID=40&md5=f67e2fe0ae8b007cda3b2701aa62ee3b%20https://www.sciencedirect.com/science/article/pii/S0300571223003524?via%3Dihub.

[76] H. W. Ho et al. “The feasibility and efficacy of new SBRT technique HyperArc for recurrent nasopharyngeal carcinoma: noncoplanar cone-based robotic system vs. noncoplanar high-definition MLC based Linac system”. In: *Med Dosim* 46.2 (2021), pp. 164–170. DOI: doi:http://dx.doi.org/10.1016/j.meddos.2020.10.007.

[77] M. Sun et al. “Robot-assisted mandibular angle osteotomy using electromagnetic navigation”. In: *Ann Transl Med* 9.7 (2021), p. 567. DOI: doi:http://dx.doi.org/10.21037/atm-20-6305.

[78] B. S. Kim et al. “Feasibility of a Robot-Assisted Surgical Navigation System for Mandibular Distraction Osteogenesis in Hemifacial Microsomia: A Model Experiment”. In: *J Craniofac Surg* 34.2 (2023), pp. 525–531. DOI: doi:http://dx.doi.org/10.1097/scs.0000000000009028.

[79] T. Y. Linn et al. “Accuracy of implant site preparation in robotic navigated dental implant surgery”. In: *Clin Implant Dent Relat Res* (2023). DOI: doi:http://dx.doi.org/10.1111/cid.13224.

[80] L. Shao et al. “Robot-assisted augmented reality surgical navigation based on optical tracking for mandibular reconstruction surgery”. In: *Med Phys* (2023). DOI: doi:http://dx.doi.org/10.1002/mp.16598.

[81] T. Sun et al. “Accuracy and Security Analysis of a Cranio-Maxillofacial Plastic Surgery Robot Equipped With Piezosurgery in Genioplasty”. In: *The Journal of craniofacial surgery* 33.5 (2022), pp. 1533–1536. DOI: doi:http://dx.doi.org/10.1097/scs.0000000000008617. URL: http://ovidsp.ovid.com/ovidweb.cgi?T=JS&PAGE=reference&D=emed23&NEWS=N&AN=637488389.

[82] J. Wang et al. “Image-guided cochlear access by non-invasive registration: a cadaveric feasibility study”. In: *Sci Rep* 10.1 (2020), p. 18318. DOI: doi:https://doi.org/10.1038/s41598-020-75530-7. URL: https://www.nature.com/articles/s41598-020-75530-7.pdf.

[83] C. Xu et al. “A Preliminary Study on Animal Experiments of Robot-Assisted Craniotomy”. In: *World Neurosurg* 149 (2021), e748–e757. DOI: doi:http://dx.doi.org/10.1016/j.wneu.2021.01.108.

[84] S. C. Desai et al. “Transoral robotic surgery using an image guidance system”. In: *Laryngoscope* 118.11 (2008), pp. 2003–2005. DOI: doi:http://dx.doi.org/10.1097/mlg.0b013e3181818784. URL: http://ovidsp.ovid.com/ovidweb.cgi?T=JS&PAGE=reference&D=emed10&NEWS=N&AN=355035114.

[85] R. K. Tsang et al. “Adapting Electromagnetic Navigation System for Transoral Robotic-Assisted Skull Base Surgery”. In: *Laryngoscope* 130.8 (2020), pp. 1922–1925. DOI: doi:http://dx.doi.org/10.1002/lary.28220.

[86] H. G. Zalzal et al. “Robotic-assisted transmaxillary approach for removal of juvenile nasopharyngeal angiofibroma of the pterygopalatine and infratemporal fossa”. In: *Head Neck* 42.9 (2020), pp. 2745–2749. DOI: doi:http://dx.doi.org/10.1002/hed.26236.

[87] G. K. Austin et al. “Image-guided robotic skull base surgery”. In: *J Neurol Surg B Skull Base* 75.4 (2014), pp. 231–235. DOI: doi:https://doi.org/10.1055/s-0033-1363172.

[88] W. P. Liu et al. “Intraoperative image-guided transoral robotic surgery: pre-clinical studies”. In: *Int J Med Robot* 11.2 (2015), pp. 256–267. DOI: doi:https://doi.org/10.1002/rcs.1602.

[89] Z. M. Aung et al. “Model Experimental Study of Man-Machine Interactive Robot-Assisted Craniotomy”. In: *J Craniofac Surg* 32.3 (2021), pp. 925–930. DOI: doi:http://dx.doi.org/10.1097/scs.0000000000007308.

[90] I. J. Kwon et al. “Development of autonomous robot osteotomy for mandibular ramal bone harvest and evaluation of its accuracy: A phantom mandible-based trial”. In: *Applied Sciences (Switzerland)* 11.6 (2021). DOI: doi:http://dx.doi.org/10.3390/app11062885. URL: https://www.scopus.com/inward/record.uri?eid=2-s2.0-85103267255&doi=10.3390%2fapp11062885&partnerID=40&md5=18cfdd434c03d4c0c09780f3961e4f96.

[91] S. Liu et al. “Automated Implant Resizing for Single-Stage Cranioplasty”. In: *IEEE Robot Autom Lett* 6.4 (2021), pp. 6624–6631. DOI: doi:http://dx.doi.org/10.1109/lra.2021.3095286.

[92] C. Xu et al. “Research on spatial motion safety constraints and cooperative control of robot-assisted craniotomy: Beagle model experiment verification”. In: *Int J Med Robot* 17.2 (2021), e2231. DOI: doi:http://dx.doi.org/10.1002/rcs.2231.

[93] L. Liu et al. “Realization and Control of Robotic Injection Prototype with Instantaneous Remote Center of Motion Mechanism”. In: *IEEE Transactions on Biomedical Engineering* (2023), pp. 1–13. DOI: doi:https://doi.org/10.1109/tbme.2023.3306555. URL: https://www.scopus.com/inward/record.uri?eid=2-s2.0-85168722806&doi=10.1109%2fTBME.2023.3306555&partnerID=40&md5=712a5e7c10a51afd338c1e68e4c39e75%20https://ieeexplore.ieee.org/stampPDF/getPDF.jsp?tp=&arnumber=10224338&ref=.

[94] K. W. Baek et al. “Clinical applicability of robot-guided contact-free laser osteotomy in cranio-maxillo-facial surgery: in-vitro simulation and in-vivo surgery in minipig mandibles”. In: *Br J Oral Maxillofac Surg* 53.10 (2015), pp. 976–981. DOI: doi:http://dx.doi.org/10.1016/j.bjoms.2015.07.019.

[95] S. Tauscher et al. “High-accuracy drilling with an image guided light weight robot: autonomous versus intuitive feed control”. In: *Int J Comput Assist Radiol Surg* 12.10 (2017), pp. 1763–1773. DOI: doi:http://dx.doi.org/10.1007/s11548-017-1638-x.

[96] A. A. Vorotnikov et al. “Criteria for comparison of robot movement trajectories and manual movements of a doctor for performing maxillofacial surgeries”. In: *International Journal of Mechanical Engineering and Robotics Research* 7.4 (2018), pp. 361–366. DOI: doi:http://dx.doi.org/10.18178/ijmerr.7.4.361-366. URL: https://www.scopus.com/inward/record.uri?eid=2-s2.0-85049741009&doi=10.18178%2fijmerr.7.4.361-366&partnerID=40&md5=f3b3d34bcc86325c59eb12efb9eebf0e.

[97] J. J. Han et al. “A robot arm and image-guided navigation assisted surgical system for maxillary repositioning in orthognathic surgery: A phantom skull-based trial”. In: *Applied Sciences (Switzerland)* 10.4 (2020). DOI: doi:http://dx.doi.org/10.3390/app10041549. URL: https://www.scopus.com/inward/record.uri?eid=2-s2.0-85080939828&doi=10.3390%2fapp10041549&partnerID=40&md5=31e7f845b4a53890be0ef3676547c0ab.

[98] J. J. Han et al. “Robot-Assisted Maxillary Positioning in Orthognathic Surgery: A Feasibility and Accuracy Evaluation”. In: *J Clin Med* 10.12 (2021), p. 2596. DOI: doi:http://dx.doi.org/10.3390/jcm10122596.

[99] S. Müller et al. “Workflow assessment as a preclinical development tool : Surgical process models of three techniques for minimally invasive cochlear implantation”. In: *Int J Comput Assist Radiol Surg* 14.8 (2019), pp. 1389–1401. DOI: doi:http://dx.doi.org/10.1007/s11548-019-02002-3.

[100] J. Burgner et al. “Ex vivo accuracy evaluation for robot assisted laser bone ablation”. In: *Int J Med Robot* 6.4 (2010). 1478-596x Burgner, J Müller, M Raczkowsky, J Wörn, H Journal Article Research Support, Non-U.S. Gov’t England 2010/11/26 Int J Med Robot. 2010 Dec;6(4):489-500. doi: 10.1002/rcs.366. Epub 2010 Nov 11., pp. 489–500. DOI: 10.1002/rcs.366.

[101] Z. Cao et al. “Pilot study of a surgical robot system for zygomatic implant placement”. In: *Med Eng Phys* 75 (2020), pp. 72–78. DOI: doi:http://dx.doi.org/10.1016/j.medengphy.2019.07.020.

[102] Y. Li et al. “Automatic robot-world calibration in an optical-navigated surgical robot system and its application for oral implant placement”. In: *Int J Comput Assist Radiol Surg* 15.10 (2020), pp. 1685–1692. DOI: doi:http://dx.doi.org/10.1007/s11548-020-02232-w.

[103] Z. Bárdosi et al. “CIGuide: in situ augmented reality laser guidance”. In: *Int J Comput Assist Radiol Surg* 15.1 (2020), pp. 49–57. DOI: doi:http://dx.doi.org/10.1007/s11548-019-02066-1.

[104] S. Baron et al. “Percutaneous inner-ear access via an image-guided industrial robot system”. In: *Proceedings of the Institution of Mechanical Engineers. Part H, Journal of engineering in medicine* 224.5 (2010), pp. 633–649. DOI: doi:http://dx.doi.org/10.1243/09544119jeim781. URL: http://ovidsp.ovid.com/ovidweb.cgi?T=JS&PAGE=reference&D=emed11&NEWS=N&AN=360290932.

[105] A. Danilchenko et al. “Robotic mastoidectomy”. In: *Otology neurotology : official publication of the American Otological Society, American Neurotology Society [and] European Academy of Otology and Neurotology* 32.1 (2011), pp. 11–16. DOI: doi:http://dx.doi.org/10.1097/mao.0b013e3181fcee9e. URL: http://ovidsp.ovid.com/ovidweb.cgi?T=JS&PAGE=reference&D=emed12&NEWS=N&AN=360279666.

[106] K. W. Eichhorn et al. “Robot-assisted endoscope guidance versus manual endoscope guidance in functional endonasal sinus surgery (FESS)”. In: *Acta Oto-Laryngologica* 137.10 (2017), pp. 1090–1095. DOI: doi:http://dx.doi.org/10.1080/00016489.2017.1336284. URL: http://ovidsp.ovid.com/ovidweb.cgi?T=JS&PAGE=reference&D=emed18&NEWS=N&AN=616783725.

[107] G. Liu et al. “Space calibration of the cranial and maxillofacial robotic system in surgery”. In: *Computer Assisted Surgery* 21 (2016), pp. 55–61. DOI: doi:http://dx.doi.org/10.1080/24699322.2016.1240314. URL: https://www.scopus.com/inward/record.uri?eid=2-s2.0-85015386002&doi=10.1080%2f24699322.2016.1240314&partnerID=40&md5=feed3ed6eefff12cfa658fa9aa0f572f.

[108] K. T. Kavanagh. “Applications of image-directed robotics in otolaryngologic surgery”. In: *Laryngoscope* 104.3 (1994), pp. 283–293. DOI: doi:http://dx.doi.org/10.1288/00005537-199403000-00008. URL: https://www.scopus.com/inward/record.uri?eid=2-s2.0-0028204379&doi=10.1288%2f00005537-199403000-00008&partnerID=40&md5=3f8e493ab5549bc146511df42e35839f.

[109] X. Z. Kong et al. “An integrated system for planning, navigation and robotic assistance for mandible reconstruction surgery”. In: *Intelligent Service Robotics* 9.2 (2016), pp. 113–121. DOI: doi:http://dx.doi.org/10.1007/s11370-015-0189-7. URL: https://www.scopus.com/inward/record.uri?eid=2-s2.0-84961201908&doi=10.1007%2fs11370-015-0189-7&partnerID=40&md5=7ff688fa52c9068c86b56ccd875aedac.

[110] L. Lin et al. “Preliminary clinical experience of robot-assisted surgery in treatment with genioplasty”. In: *Sci Rep* 11.1 (2021), p. 6365. DOI: doi:http://dx.doi.org/10.1038/s41598-021-85889-w.

[111] M. Sun et al. “Fully Automatic Robot-Assisted Surgery for Mandibular Angle Split Osteotomy”. In: *J Craniofac Surg* 31.2 (2020), pp. 336–339. DOI: doi:http://dx.doi.org/10.1097/scs.0000000000005587.

[112] S. Weihe et al. “Synthesis of CAD/CAM, robotics and biomaterial implant fabrication: single-step reconstruction in computer-aided frontotemporal bone resection”. In: *Int J Oral Maxillofac Surg* 29.5 (2000), pp. 384–388. DOI: doi:http://dx.doi.org/10.1016/s0901-5027(00)80059-4.

[113] T. C. Lueth et al. “A surgical robot system for maxillofacial surgery”. In: *IECON ’98. Proceedings of the 24th Annual Conference of the IEEE Industrial Electronics Society (Cat. No.98CH36200)*. Vol. 4, 2470–2475 vol.4. DOI: 10.1109/IECON.1998.724114. URL: https://ieeexplore.ieee.org/stampPDF/getPDF.jsp?tp=&arnumber=724114&ref=.

[114] T. Cui et al. “Control Strategy and Experiments for Robot Assisted Craniomaxillofacial Surgery System”. In: *Mathematical Problems in Engineering* 2019 (2019). DOI: doi:http://dx.doi.org/10.1155/2019/4853046. URL: https://www.scopus.com/inward/record.uri?eid=2-s2.0-85064255775&doi=10.1155%2f2019%2f4853046&partnerID=40&md5=335d34fe37decac583ce4f398f93d996.

[115] X. Duan et al. “Modelling and Experiment Based on a Navigation System for a Cranio-Maxillofacial Surgical Robot”. In: *J Healthc Eng* 2018 (2018), p. 4670852. DOI: doi:http://dx.doi.org/10.1155/2018/4670852.

[116] J. H. Zhu et al. “Prospects of Robot-Assisted Mandibular Reconstruction with Fibula Flap: Comparison with a Computer-Assisted Navigation System and Freehand Technique”. In: *J Reconstr Microsurg* 32.9 (2016), pp. 661–669. DOI: doi:http://dx.doi.org/10.1055/s-0036-1584805.

[117] Yonggui Wang et al. “Spatial Registration for a Three-Arm Robot Assisted Mandible Reconstruction Surgery”. In: *Mathematical Problems in Engineering* 2015 (2015), p. 689278. DOI: 10.1155/2015/689278. URL: https://doi.org/10.1155/2015/689278%20https://downloads.hindawi.com/journals/mpe/2015/689278.pdf.

[118] J. Ansó et al. “Feasibility of using EMG for early detection of the facial nerve during robotic direct cochlear access”. In: *Otol Neurotol* 35.3 (2014), pp. 545–554. DOI: doi:http://dx.doi.org/10.1097/mao.0000000000000187.

[119] N. Gerber et al. “High-accuracy patient-to-image registration for the facilitation of image-guided robotic microsurgery on the head”. In: *IEEE Trans Biomed Eng* 60.4 (2013), pp. 960–968. DOI: doi:http://dx.doi.org/10.1109/tbme.2013.2241063.

[120] S. Weber et al. “Instrument flight to the inner ear”. In: *Sci Robot* 2.4 (2017). DOI: doi:http://dx.doi.org/10.1126/scirobotics.aal4916.

[121] T. M. Williamson et al. “Estimation of tool pose based on force-density correlation during robotic drilling”. In: *IEEE Trans Biomed Eng* 60.4 (2013), pp. 969–976. DOI: doi:http://dx.doi.org/10.1109/tbme.2012.2235439.

[122] B. Bell et al. “In vitro accuracy evaluation of image-guided robot system for direct cochlear access”. In: *Otol Neurotol* 34.7 (2013), pp. 1284–1290. DOI: doi:https://doi.org/10.1097/mao.0b013e31829561b6.

[123] B. Bell et al. “An image-guided robot system for direct cochlear access”. In: *Cochlear Implants Int* 15 (2014), S11–S13. DOI: doi:https://doi.org/10.1179/1467010014z.000000000192.

[124] Y. Feng et al. “An image-guided hybrid robot system for dental implant surgery”. In: *Int J Comput Assist Radiol Surg* 17.1 (2022), pp. 15–26. DOI: doi:http://dx.doi.org/10.1007/s11548-021-02484-0.

[125] B. A. Jereczek-Fossa et al. “CyberKnife robotic image-guided stereotactic radiotherapy for oligometastic cancer : A prospective evaluation of 95 patients/118 lesions”. In: *Strahlenther Onkol* 189.6 (2013), pp. 448–455. DOI: doi:http://dx.doi.org/10.1007/s00066-013-0345-y.

[126] S. Y. Woo et al. “Autonomous bone reposition around anatomical landmark for robot-assisted orthognathic surgery”. In: *J Craniomaxillofac Surg* 45.12 (2017), pp. 1980–1988. DOI: doi:http://dx.doi.org/10.1016/j.jcms.2017.09.001.

[127] M. H. Yoo et al. “A cadaver study of mastoidectomy using an image-guided human-robot collaborative control system”. In: *Laryngoscope Investig Otolaryngol* 2.5 (2017), pp. 208–214. DOI: doi:http://dx.doi.org/10.1002/lio2.111.

[128] G. Fang et al. “Soft robotic manipulator for intraoperative MRI-guided transoral laser microsurgery”. In: *Sci Robot* 6.57 (2021). DOI: doi:http://dx.doi.org/10.1126/scirobotics.abg5575.

[129] Q. Ma et al. “Autonomous Surgical Robot with Camera-Based Markerless Navigation for Oral and Maxillofacial Surgery”. In: *IEEE/ASME Transactions on Mechatronics* 25.2 (2020), pp. 1084–1094. DOI: doi:http://dx.doi.org/10.1109/tmech.2020.2971618. URL: https://www.scopus.com/inward/record.uri?eid=2-s2.0-85083915983&doi=10.1109%2fTMECH.2020.2971618&partnerID=40&md5=a7091089b90f1799afff454a823b1077.

[130] Q. Ma et al. “Development and preliminary evaluation of an autonomous surgical system for oral and maxillofacial surgery”. In: *Int J Med Robot* 15.4 (2019), e1997. DOI: doi:http://dx.doi.org/10.1002/rcs.1997.

[131] M. Augello et al. “Comparative microstructural analysis of bone osteotomies after cutting by computer-assisted robot-guided laser osteotome and piezoelectric osteotome: an in vivo animal study”. In: *Lasers Med Sci* 33.7 (2018), pp. 1471–1478. DOI: doi:http://dx.doi.org/10.1007/s10103-018-2502-0.

[132] K. Bumm et al. “An automated robotic approach with redundant navigation for minimal invasive extended transsphenoidal skull base surgery”. In: *Minim Invasive Neurosurg* 48.3 (2005), pp. 159–164. DOI: doi:http://dx.doi.org/10.1055/s-2005-870903.

[133] J. P. Kobler et al. “An automated insertion tool for cochlear implants with integrated force sensing capability”. In: *Int J Comput Assist Radiol Surg* 9.3 (2014), pp. 481–494. DOI: doi:http://dx.doi.org/10.1007/s11548-013-0936-1.

[134] P. Bohner et al. “Operation planning in craniomaxillofacial surgery”. In: *Computer Aided Surgery* 2.3 (1997), pp. 153–161. DOI: doi:http://dx.doi.org/10.1002/(sici)1097-0150(1997)2:3/4. URL: http://ovidsp.ovid.com/ovidweb.cgi?T=JS&PAGE=reference&D=emed6&NEWS=N&AN=27435432.

[135] H. Liu et al. “A Robotic System Integrated With CBCT for Cochlear Implant Surgery: Accuracy Improvement and Validation”. In: *IEEE Robotics and Automation Letters* 8.12 (2023), pp. 8010–8017. DOI: doi:https://doi.org/10.1109/lra.2023.3325778. URL: https://www.scopus.com/inward/record.uri?eid=2-s2.0-85174804681&doi=10.1109%2fLRA.2023.3325778&partnerID=40&md5=89a12e8d5191d3e71ebb9f23abb1e37e%20https://ieeexplore.ieee.org/stampPDF/getPDF.jsp?tp=&arnumber=10287406&ref=.

[136] J. H. Zhu et al. “Performance of Robotic Assistance for Skull Base Biopsy: A Phantom Study”. In: *J Neurol Surg B Skull Base* 78.5 (2017), pp. 385–392. DOI: doi:http://dx.doi.org/10.1055/s-0037-1602791.

[137] B. Bell et al. “A self-developed and constructed robot for minimally invasive cochlear implantation”. In: *Acta Otolaryngol* 132.4 (2012), pp. 355–360. DOI: doi:http://dx.doi.org/10.3109/00016489.2011.642813.

[138] C. Xu et al. “Application research of master-slave cranio-maxillofacial surgical robot based on force feedback”. In: *Proc Inst Mech Eng H* 235.5 (2021), pp. 583–596. DOI: doi:http://dx.doi.org/10.1177/0954411921997568.

[139] R. Torres et al. “Cochlear Implant Insertion Axis Into the Basal Turn: A Critical Factor in Electrode Array Translocation”. In: *Otol Neurotol* 39.2 (2018), pp. 168–176. DOI: doi:http://dx.doi.org/10.1097/mao.0000000000001648.

[140] L. B. Kratchman et al. “Design of a bone-attached parallel robot for percutaneous cochlear implantation”. In: *IEEE Transactions on Biomedical Engineering* 58.10 (2011), pp. 2904–2910. DOI: doi:http://dx.doi.org/10.1109/tbme.2011.2162512. URL: https://www.scopus.com/inward/record.uri?eid=2-s2.0-80053203494&doi=10.1109%2fTBME.2011.2162512&partnerID=40&md5=206d0b01eab617fa92edae3ddb7b51d8.

[141] L. Wu et al. “Development of a compact continuum tubular robotic system for nasopharyngeal biopsy”. In: *Medical and Biological Engineering and Computing* 55.3 (2017), pp. 403–417. DOI: doi:http://dx.doi.org/10.1007/s11517-016-1514-9. URL: https://www.scopus.com/inward/record.uri?eid=2-s2.0-84969932774&doi=10.1007%2fs11517-016-1514-9&partnerID=40&md5=1c0d5945c5fca31371354c5c1fe8123f.

[142] Gerlig Widmann et al. “Errors and error management in image-guided craniomaxillofacial surgery”. In: *Oral Surgery, Oral Medicine, Oral Pathology, Oral Radiology, and Endodontology* 107.5 (2009), pp. 701–715.

[143] G. Subedi et al. “Factors that may determine the targeting accuracy of image-guided radiosurgery”. In: *Medical Physics* 42.10 (2015), pp. 6004–6010. DOI: doi:http://dx.doi.org/10.1118/1.4930961. URL: http://aapm.onlinelibrary.wiley.com/hub/journal/10.1002/(ISSN)2473-4209/issues/http://ovidsp.ovid.com/ovidweb.cgi?T=JS&PAGE=reference&D=emed16&NEWS=N&AN=606140004.

[144] J. Anso et al. “Electrical Impedance to Assess Facial Nerve Proximity During Robotic Cochlear Implantation”. In: *IEEE Trans Biomed Eng* 66.1 (2019), pp. 237–245. DOI: doi:http://dx.doi.org/10.1109/tbme.2018.2830303.

[145] J. Ansó et al. “A Neuromonitoring Approach to Facial Nerve Preservation During Image-guided Robotic Cochlear Implantation”. In: *Otol Neurotol* 37.1 (2016), pp. 89–98. DOI: doi:http://dx.doi.org/10.1097/mao.0000000000000914.

[146] J. Ansó et al. “Neuromonitoring During Robotic Cochlear Implantation: Initial Clinical Experience”. In: *Ann Biomed Eng* 46.10 (2018), pp. 1568–1581. DOI: doi:http://dx.doi.org/10.1007/s10439-018-2094-7.

[147] K. W. Baek et al. “A comparative investigation of bone surface after cutting with mechanical tools and Er:YAG laser”. In: *Lasers Surg Med* 47.5 (2015), pp. 426–32. DOI: 10.1002/lsm.22352.

[148] H. Bahig et al. “Conventionally fractionated large volume head and neck re-irradiation using multileaf collimator-based robotic technique: A feasibility study”. In: *Clinical and Translational Radiation Oncology* 24 (2020), pp. 102–110. DOI: doi:http://dx.doi.org/10.1016/j.ctro.2020.06.012. URL: https://www.journals.elsevier.com/clinical-and-translational-radiation-oncology/http://ovidsp.ovid.com/ovidweb.cgi?T=JS&PAGE=reference&D=emed21&NEWS=N&AN=2007092258.

[149] M. Caversaccio et al. “Robotic cochlear implantation: surgical procedure and first clinical experience”. In: *Acta Otolaryngol* 137.4 (2017), pp. 447–454. DOI: doi:https://doi.org/10.1080/00016489.2017.1278573.

[150] M. Caversaccio et al. “Robotic middle ear access for cochlear implantation: First in man”. In: *PLoS One* 14.8 (2019). 1932-6203 Caversaccio, Marco Wimmer, Wilhelm Orcid: 0000-0001-5392-2074 Anso, Juan Orcid: 0000-0001-9127-0396 Mantokoudis, Georgios Gerber, Nicolas Rathgeb, Christoph Schneider, Daniel Hermann, Jan Wagner, Franca Orcid: 0000-0001-7502-4814 Scheidegger, Olivier Orcid: 0000-0003-3925-5142 Huth, Markus Anschuetz, Lukas Kompis, Martin Williamson, Tom Bell, Brett Gavaghan, Kate Weber, Stefan Journal Article Research Support, Non-U.S. Gov’t United States 2019/08/03 PLoS One. 2019 Aug 2;14(8):e0220543. doi: 10.1371/journal.pone.0220543. eCollection 2019., e0220543. DOI: 10.1371/journal.pone.0220543. URL: https://journals.plos.org/plosone/article/file?id=10.1371/journal.pone.0220543&type=printable.

[151] Y. Chen et al. “Safety-Enhanced Motion Planning for Flexible Surgical Manipulator Using Neural Dynamics”. In: *IEEE Transactions on Control Systems Technology* 25.5 (2017), pp. 1711–1723. DOI: doi:http://dx.doi.org/10.1109/tcst.2016.2628806. URL: https://www.scopus.com/inward/record.uri?eid=2-s2.0-85029366466&doi=10.1109%2fTCST.2016.2628806&partnerID=40&md5=0b1a493eea526e2f2745446502490519.

[152] K. Deguchi et al. “Application of cyberknife for the treatment of Juvenile nasopharyngeal angiofibroma: A case report”. In: *Auris Nasus Larynx* 29.4 (2002), pp. 395–400. DOI: doi:https://doi.org/10.1016/s0385-8146(02)00060-3. URL: https://www.scopus.com/inward/record.uri?eid=2-s2.0-0036775875&doi=10.1016%2fS0385-8146%2802%2900060-3&partnerID=40&md5=669b201a26683e5f5cd0aee4de471adc%20https://www.sciencedirect.com/science/article/pii/S0385814602000603?via%3Dihub.

[153] S. Dibart et al. “Robot Assisted Implant Surgery: Hype or Hope?” In: *J Stomatol Oral Maxillofac Surg* (2023), p. 101612. DOI: doi:http://dx.doi.org/10.1016/j.jormas.2023.101612.

[154] A. Dizman et al. “Reirradiation with robotic stereotactic body radiation therapy for locally recurrent nasopharyngeal carcinoma”. In: *International Journal of Radiation Oncology Biology Physics* 87.2 (2013), S729. DOI: doi:http://dx.doi.org/10.1016/j.ijrobp.2013.06.1932. URL: http://ovidsp.ovid.com/ovidweb.cgi?T=JS&PAGE=reference&D=emed14&NEWS=N&AN=71187341.

[155] P. Hurmuz et al. “Robotic stereotactic radiosurgery in patients with unresectable glomus jugulare tumors”. In: *Technol Cancer Res Treat* 12.2 (2013), pp. 109–113. DOI: doi:http://dx.doi.org/10.7785/tcrt.2012.500303.

[156] H. Lim et al. “Semi-manual mastoidectomy assisted by human-robot collaborative control - A temporal bone replica study”. In: *Auris Nasus Larynx* 43.2 (2016), pp. 161–165. DOI: doi:http://dx.doi.org/10.1016/j.anl.2015.08.008.

[157] W. Nijdam et al. “Robotic radiosurgery vs. brachytherapy as a boost to intensity modulated radiotherapy for tonsillar fossa and soft palate tumors: The clinical and economic impact of an emerging technology”. In: *Technology in Cancer Research and Treatment* 6.6 (2007), pp. 611–619. DOI: doi:http://dx.doi.org/10.1177/153303460700600604. URL: https://journals.sagepub.com/home/TCThttp://ovidsp.ovid.com/ovidweb.cgi?T=JS&PAGE=reference&D=emed10&NEWS=N&AN=351019276.

[158] C. Rathgeb et al. “The accuracy of image-based safety analysis for robotic cochlear implantation”. In: *Int J Comput Assist Radiol Surg* 14.1 (2019), pp. 83–92. DOI: doi:http://dx.doi.org/10.1007/s11548-018-1834-3.

[159] M. Sin et al. “Development of a Real-Time 6-DOF Motion-Tracking System for Robotic Computer-Assisted Implant Surgery”. In: *Sensors (Basel)* 23.5 (2023). DOI: doi:http://dx.doi.org/10.3390/s23052450.

[160] S. Song et al. “Preliminary study on magnetic tracking-based planar shape sensing and navigation for flexible surgical robots in transoral surgery: methods and phantom experiments”. In: *Int J Comput Assist Radiol Surg* 13.2 (2018), pp. 241–251. DOI: doi:http://dx.doi.org/10.1007/s11548-017-1672-8.

[161] J. A. Vargo et al. “Stereotactic body radiation therapy for locally recurrent, previously irradiated non-squamous cell cancers of the head and neck”. In: *Head Neck* 34.8 (2012), pp. 1153–1161. DOI: doi:http://dx.doi.org/10.1002/hed.21889.

[162] F. Venail et al. “Manual Electrode Array Insertion Through a Robot-Assisted Minimal Invasive Cochleostomy: Feasibility and Comparison of Two Different Electrode Array Subtypes”. In: *Otology and Neurotology* 36.6 (2015), pp. 1015–1022. DOI: doi:https://doi.org/10.1097/mao.0000000000000741. URL: https://www.scopus.com/inward/record.uri?eid=2-s2.0-84933502836&doi=10.1097%2fMAO.0000000000000741&partnerID=40&md5=89ca0ea2b9de4fdbe9ba9b564ff1c7e5.

[163] J. von der Grun et al. “Second infield re-irradiation with a resulting cumulative equivalent dose (EQD2max) of >180 Gy for patients with recurrent head and neck cancer”. In: *Head and Neck* 41.4 (2019), E48–E54. DOI: doi:http://dx.doi.org/10.1002/hed.25428. URL: http://onlinelibrary.wiley.com/journal/10.1002/(ISSN)1097-0347http://ovidsp.ovid.com/ovidweb.cgi?T=JS&PAGE=reference&D=emed20&NEWS=N&AN=625382372.

[164] W. Wimmer et al. “Cone beam and micro-computed tomography validation of manual array insertion for minimally invasive cochlear implantation”. In: *Audiology and Neurotology* 19.1 (2014), pp. 22–30. DOI: doi:https://doi.org/10.1159/000356165. URL: https://www.karger.ch/journals/aud/aud_jh.htmhttp://ovidsp.ovid.com/ovidweb.cgi?T=JS&PAGE=reference&D=emed15&NEWS=N&AN=604041030%20https://karger.com/aud/article-pdf/19/1/22/2245178/000356165.pdf.

[165] W. Wimmer et al. “Semiautomatic cochleostomy target and insertion trajectory planning for minimally invasive cochlear implantation”. In: *Biomed Res Int* 2014 (2014), p. 596498. DOI: doi:https://doi.org/10.1155/2014/596498. URL: https://downloads.hindawi.com/journals/bmri/2014/596498.pdf.

[166] Z. Zhang et al. “Preliminary study of the accuracy and safety of robot-assisted mandibular distraction osteogenesis with electromagnetic navigation in hemifacial microsomia using rabbit models”. In: *Sci Rep* 12.1 (2022), p. 19572. DOI: doi:http://dx.doi.org/10.1038/s41598-022-21893-y.

[167] J Michael Fitzpatrick. “Fiducial registration error and target registration error are uncorrelated”. In: *Medical Imaging 2009: Visualization, Image-Guided Procedures, and Modeling*. Vol. 7261. SPIE. 2009, pp. 21–32.

B

Results in Detail

Measurement	AB Optitrack	BC Optitrack	CD Optitrack	AB Kuka	BC Kuka	CD Kuka	AB Fused	BC Fused	CD Fused	Number	Haply Result	Number	Haply Result
incline	0,469	0,095	0,522	0,041	0,049	0,326	0,072	0,074	0,397	1	0,377	31	0,652
incline	0,237	0,013	0,398	0,034	0,181	0,192	0,165	0,084	0,298	2	0,151	32	0,440
incline	0,282	0,703	0,001	0,161	0,426	0,403	0,160	0,502	0,277	3	0,806	33	0,587
incline	0,156	0,239	0,370	0,052	0,053	0,225	0,021	0,088	0,284	4	0,428	34	0,496
incline	0,196	0,083	0,488	0,038	0,152	0,185	0,207	0,103	0,309	5	0,518	35	0,611
incline	0,020	0,029	0,017	0,179	0,006	0,044	0,017	0,013	0,050	6	0,654	36	0,631
Z	0,146	0,652	0,093	0,044	0,220	0,089	0,058	0,359	0,091	7	0,713	37	1,074
Z	0,029	0,249	0,080	0,073	0,065	0,115	0,033	0,170	0,062	8	0,531	38	0,933
Z	0,161	0,378	0,085	0,078	0,107	0,087	0,022	0,181	0,013	9	0,694	39	0,878
Z	0,273	0,593	0,082	0,066	0,202	0,078	0,113	0,311	0,023	10	0,564	40	0,720
Z	0,011	0,388	0,163	0,204	0,028	0,076	0,146	0,137	0,078	11	0,675	41	0,833
Z	0,004	0,076	0,251	0,074	0,052	0,260	0,086	0,098	0,304	12	0,608	42	0,775
Z	0,011	0,289	0,198	0,068	0,040	0,192	0,030	0,100	0,039	13	0,701	43	0,809
Z	0,263	0,264	0,433	0,139	0,027	0,162	0,185	0,090	0,050	14	0,346	44	0,722
Z	0,152	0,372	0,278	0,106	0,074	0,076	0,153	0,148	0,036	15	0,536	45	0,038
X	0,261	0,487	0,131	0,088	0,025	0,071	0,089	0,027	0,064	16	0,546	46	0,060
X	0,301	0,812	0,613	0,157	0,132	0,494	0,159	0,132	0,494	17	0,493	47	0,035
X	0,110	0,467	0,274	0,127	0,024	0,264	0,127	0,024	0,264	18	0,625	48	0,043
X	0,183	0,128	0,227	0,074	0,015	0,507	0,075	0,015	0,508	19	0,477	49	0,048
X	0,080	0,780	0,650	0,065	0,175	0,279	0,064	0,175	0,279	20	0,665	50	0,025
X	0,038	0,401	0,572	0,348	0,121	0,458	0,348	0,122	0,457	21	0,404	51	0,043
X	0,058	0,126	0,099	0,096	0,006	0,360	0,096	0,006	0,360	22	0,628	52	0,115
X	0,020	0,125	0,303	0,249	0,192	0,427	0,249	0,192	0,426	23	0,574	53	0,023
X	0,080	0,383	0,113	0,342	0,285	0,259	0,346	0,289	0,259	24	0,467	54	0,264
Y	0,142	0,017	0,178	0,014	0,037	0,332	0,014	0,036	0,331	25	0,859	55	0,229
Y	0,022	0,552	0,040	0,014	0,241	0,183	0,015	0,241	0,183	26	0,772	56	0,279
Y	0,030	0,539	0,020	0,047	0,128	0,295	0,047	0,128	0,295	27	0,764	57	0,223
Y	0,211	0,391	0,175	0,069	0,245	0,341	0,107	0,565	0,173	28	0,798	58	0,335
Y	0,226	0,070	0,392	0,005	0,348	0,425	0,277	0,148	0,377	29	0,556	59	0,176
Y	0,378	0,204	0,536	0,101	0,117	0,623	0,264	0,215	0,590	30	0,585		
MEAN	**0,152**	**0,330**	**0,259**	**0,105**	**0,126**	**0,261**	**0,125**	**0,159**	**0,246**		**0,584**		**0,417**
STDEV	0,121	0,235	0,195	0,087	0,108	0,154	0,097	0,135	0,166		0,155		0,335

	Median	**0,201**		**Median**	**0,119**		**Median**	**0,141**		**Median**	**0,556**		
	Mean	**0,247**		**Mean**	**0,164**		**Mean**	**0,177**		**Mean**	**0,502**		
	StDev	**0,201**		**StDev**	**0,137**		**StDev**	**0,143**		**StDev**	**0,270**		
	Max	**0,812**		**Min**	**0,623**		**Min**	**0,590**		**Min**	**0,023**		
	Min	**0,001**		**Max**	**0,005**		**Max**	**0,006**		**Max**	**1,074**		

# Moves ABCD	90
# Fusion best	18
Percentage	20%

Figure B.1: Results from Experiments 1a and 1b, evaluating the technical accuracy of individual hardware components used in this research.

FUSED	1 Fusion	2 Fusion	3 Fusion	4 Fusion	5 Fusion	6 Fusion	7 Fusion	8 Fusion	9 Fusion	10 Fusion	11 Fusion	12 Fusion	13 Fusion	14 Fusion	15 Fusion
Midline os frontale	2,062	0,754	0,628	0,449	0,281	1,876	2,922	0,958	0,802	2,329	0,678	1,110	1,177	0,681	1,357
Glabella	0,505	1,015	0,502	0,298	0,441	1,127	1,336	0,431	1,236	1,013	0,442	1,025	0,424	0,854	0,684
Left lateral orbital rim	0,448	1,007	0,592	0,825	0,467	1,709	1,615	0,239	1,072	0,955	1,306	0,896	0,596	0,740	1,349
Right lateral orbital rim	0,559	0,961	0,130	0,588	0,394	1,228	2,367	0,114	0,245	0,476	0,491	1,379	0,861	0,553	1,523
Left inferior orbital rim	0,635	1,006	0,303	0,485	0,629	1,098	0,352	0,320	0,717	0,216	0,217	1,704	0,533	0,913	1,295
Right inferior orbital rim	1,099	1,176	0,853	0,839	0,982	0,657	0,602	0,483	0,605	0,692	0,347	1,278	0,904	1,003	0,918
MEAN recording	**0,885**	**0,987**	**0,501**	**0,581**	**0,532**	**1,282**	**1,532**	**0,424**	**0,779**	**0,947**	**0,580**	**1,232**	**0,749**	**0,791**	**1,188**
STDEV	0,568	0,124	0,233	0,197	0,226	0,405	0,906	0,267	0,320	0,675	0,353	0,264	0,257	0,150	0,290
MEDIAN	**0,778**														
MEAN	**0,866**														
STDEV	**0,517**														

KUKA	1 KUKA	2 KUKA	3 KUKA	4 KUKA	5 KUKA	6 KUKA	7 KUKA	8 KUKA	9 KUKA	10 KUKA	11 KUKA	12 KUKA	13 KUKA	14 KUKA	15 KUKA
Midline os frontale	0,694	0,799	0,587	0,492	0,247	1,268	0,596	0,683	0,757	1,505	0,626	1,044	1,105	0,723	0,844
Glabella	0,500	0,985	0,489	0,268	0,494	0,429	0,449	0,476	1,213	1,010	0,426	1,042	0,339	0,583	0,723
Left lateral orbital rim	0,460	0,945	0,647	0,834	0,446	0,432	0,691	0,260	1,089	0,834	1,226	0,932	0,811	0,722	0,367
Right lateral orbital rim	0,529	0,906	0,234	0,648	0,591	0,370	0,499	0,172	0,519	0,411	0,542	1,441	0,838	0,588	0,755
Left inferior orbital rim	0,668	1,055	0,294	0,486	0,721	0,356	0,336	0,293	0,565	0,210	0,270	1,699	0,508	0,386	0,429
Right inferior orbital rim	1,109	1,282	0,656	0,832	1,081	0,395	0,509	0,420	0,569	0,722	0,370	1,334	0,956	1,011	1,043
MEAN recording	**0,660**	**0,995**	**0,485**	**0,593**	**0,597**	**0,542**	**0,513**	**0,384**	**0,785**	**0,782**	**0,577**	**1,249**	**0,759**	**0,669**	**0,694**
STDEV	0,218	0,150	0,166	0,202	0,260	0,326	0,111	0,167	0,272	0,418	0,312	0,268	0,260	0,190	0,233
MEDIAN	**0,611**														
MEAN	**0,686**														
STDEV	**0,326**														

OptiTrack	1 OptiTrack	2 OptiTrack	3 OptiTrack	4 OptiTrack	5 OptiTrack	6 OptiTrack	7 OptiTrack	8 OptiTrack	9 OptiTrack	10 OptiTrack	11 OptiTrack	12 OptiTrack	13 OptiTrack	14 OptiTrack	15 OptiTrack
Midline os frontale	0,185	1,784	1,300	0,955	1,274	0,832	1,575	2,312	0,728	0,903	0,410	2,016	1,964	0,762	1,186
Glabella	0,143	0,964	1,432	0,828	0,260	0,998	1,110	0,997	1,466	1,835	0,400	1,433	1,152	0,985	1,140
Left lateral orbital rim	0,416	0,712	0,750	1,255	0,539	1,802	1,092	0,652	1,085	2,708	1,723	1,210	1,109	0,845	1,153
Right lateral orbital rim	0,446	0,571	0,624	1,017	0,910	1,018	1,560	0,963	0,734	1,793	0,514	0,957	1,266	0,869	1,520
Left inferior orbital rim	0,238	0,892	1,110	0,489	0,628	1,034	0,445	1,863	1,485	0,924	0,971	0,844	0,663	1,290	0,617
Right inferior orbital rim	0,727	1,750	2,021	1,657	1,996	0,704	1,476	1,340	0,728	1,370	1,042	1,061	1,102	1,641	1,450
MEAN recording	**0,359**	**1,112**	**1,206**	**1,033**	**0,934**	**1,065**	**1,209**	**1,354**	**1,038**	**1,589**	**0,843**	**1,253**	**1,209**	**1,065**	**1,178**
STDEV	0,199	0,480	0,462	0,361	0,570	0,350	0,395	0,570	0,334	0,621	0,469	0,389	0,387	0,308	0,291
MEDIAN	**1,026**														
MEAN	**1,097**														
STDEV	**0,504**														

Total number of points	90
Total number of measureme	270
Fusion outperformance	28
Percentage	31,11%

Figure B.2: Detailed results from the second experiment, assessing the Target Registration Error (TRE) on a rigidly fixed phantom skull using the KUKA LBR iiwa 14 and OptiTrack tracking systems, as well as these modalities fused through a Kalman filter.

	Instrument Tracking - Patient Tracking								
	TRE OptiTrack - OptiTrack	TRE OptiTrack - Haply	TRE OptiTrack - Fused	TRE KUKA - OptiTrack	TRE KUKA - Haply	TRE KUKA - Fused	TRE Fused - OptiTrack	TRE Fused - Haply	TRE Fused - Fused
P1 - Q1									
Midline os frontale	0,855	10,159	1,002	1,054	10,705	1,140	2,033	11,260	1,871
Glabella	1,708	5,966	1,908	1,269	7,300	1,235	1,278	7,275	1,274
Left lateral orbital rim	2,267	5,219	2,417	1,032	7,594	0,734	1,102	7,477	0,819
Right lateral orbital rim	1,723	8,396	1,899	1,445	10,466	1,034	1,241	10,231	0,849
Left inferior orbital rim	0,826	3,262	1,622	0,850	4,467	0,549	0,771	4,379	0,553
Right inferior orbital rim	1,541	4,963	1,496	0,885	5,790	0,692	0,878	5,764	0,687
P2 - Q2									
Midline os frontale	0,618	4,377	0,650	1,665	3,935	1,694	1,655	3,955	1,673
Glabella	0,691	3,008	1,082	2,069	2,576	2,681	1,976	2,586	2,584
Left lateral orbital rim	1,539	4,753	1,097	2,223	3,851	2,203	2,099	3,917	2,060
Right lateral orbital rim	0,757	4,571	0,249	2,513	3,739	2,198	2,348	3,798	2,030
Left inferior orbital rim	0,261	1,798	1,105	1,870	0,979	0,846	1,841	0,950	0,826
Right inferior orbital rim	0,795	2,829	0,405	1,916	2,216	1,820	1,820	2,176	1,744
P3 - Q3									
Midline os frontale	0,822	3,892	0,617	1,883	3,471	1,790	1,777	3,536	1,665
Glabella	1,406	3,741	1,538	2,662	4,275	2,843	2,509	4,223	2,691
Left lateral orbital rim	1,729	3,608	1,347	3,102	4,078	2,883	2,957	4,007	2,731
Right lateral orbital rim	1,115	2,730	1,156	2,783	4,595	2,396	2,773	4,588	2,385
Left inferior orbital rim	2,398	2,589	1,396	3,525	3,421	2,449	3,365	3,375	2,290
Right inferior orbital rim	1,449	2,263	1,394	2,271	2,454	2,502	2,091	2,417	2,324
R4 - S4									
Glabella	1,259	3,675	3,421	2,812	4,670	5,541	2,607	4,552	5,342
Left lateral orbital rim	1,210	3,094	1,327	2,701	4,683	2,894	3,106	4,912	3,288
Right lateral orbital rim	1,030	3,648	0,890	2,640	5,029	2,466	2,432	4,845	2,255
Left inferior orbital rim	1,136	2,852	1,064	2,694	3,281	1,837	2,970	3,624	2,099
Right inferior orbital rim	1,534	3,423	1,291	1,168	3,275	1,635	1,149	3,432	1,638
R5 - S5									
Midline os frontale	0,896	13,187	0,917	0,983	13,085	0,712	0,946	13,133	0,681
Glabella	1,376	10,138	1,373	1,081	10,335	1,106	1,194	10,416	1,210
Left lateral orbital rim	1,380	9,119	1,429	0,926	9,837	1,230	0,944	9,840	1,236
Right lateral orbital rim	1,411	11,148	1,340	1,247	12,289	1,106	1,228	12,243	1,086
Left inferior orbital rim	1,354	6,491	1,572	1,216	7,049	0,381	1,204	6,964	0,499
Right inferior orbital rim	1,365	8,457	1,673	1,130	8,424	0,630	1,002	8,409	0,486
R6 - S6									
Midline os frontale	0,793	4,573	0,841	2,510	5,083	2,578	2,355	4,987	2,424
Glabella	0,603	3,492	0,709	3,137	1,656	3,221	2,894	1,684	2,978
Left lateral orbital rim	0,569	4,798	0,803	2,931	2,355	2,900	2,903	2,411	2,880
Right lateral orbital rim	0,829	5,945	0,411	3,343	3,798	3,056	3,774	4,056	3,436
Left inferior orbital rim	0,562	2,075	0,744	3,316	1,617	2,933	3,068	1,436	2,685
Right inferior orbital rim	1,279	3,284	0,470	2,746	3,562	3,397	2,352	3,305	3,001
U7 - T7									
Midline os frontale	0,327	14,904	0,441	1,046	15,518	1,091	0,978	15,513	0,995
Glabella	0,597	10,173	0,734	1,846	10,371	1,709	1,787	10,385	1,636
Left lateral orbital rim	1,831	12,567	1,310	1,880	11,739	1,459	1,860	11,837	1,402
Right lateral orbital rim	0,799	14,369	0,724	1,374	13,787	1,171	1,259	13,870	1,025
Left inferior orbital rim	0,360	4,993	1,357	1,488	5,180	1,263	1,488	5,144	1,253
Right inferior orbital rim	0,745	7,248	0,793	2,262	8,118	1,876	2,219	8,041	1,862
U8 - T8									
Midline os frontale	1,290	7,493	0,849	2,192	5,945	1,941	2,036	6,103	1,755
Glabella	0,664	4,777	1,050	1,703	4,521	1,694	1,552	4,496	1,569
Left lateral orbital rim	1,610	3,975	1,397	1,637	4,114	1,662	1,520	4,016	1,551
Right lateral orbital rim	0,965	3,870	1,410	1,128	4,582	1,514	1,154	4,591	1,540
Left inferior orbital rim	1,690	3,061	1,869	2,172	2,601	2,376	2,098	2,655	2,311
Right inferior orbital rim	1,326	4,194	1,452	1,144	3,321	1,434	0,985	3,450	1,288
U9 - T9									
Midline os frontale	2,026	2,986	3,711	2,111	2,210	4,283	2,117	2,237	4,234
Glabella	2,016	2,756	1,959	1,832	2,159	2,056	1,820	2,255	2,144
Left lateral orbital rim	2,201	3,221	2,084	1,955	2,614	1,977	1,973	2,547	1,981
Right lateral orbital rim	1,942	3,029	1,838	1,145	1,812	1,146	1,437	1,882	1,430
Left inferior orbital rim	1,794	3,190	1,741	1,129	2,485	1,025	1,065	2,549	1,008
P10 - R10									
Midline os frontale	0,913	16,359	0,981	1,892	17,083	2,162	1,806	17,059	2,083
Glabella	0,116	12,014	0,468	2,352	10,927	2,468	2,177	11,009	2,287
Left lateral orbital rim	0,683	12,562	0,586	2,374	11,111	2,081	2,387	11,088	2,089
Right lateral orbital rim	0,920	16,138	0,587	2,736	14,746	2,492	3,185	14,562	2,909
Left inferior orbital rim	0,525	7,136	0,745	2,512	6,303	2,552	2,354	6,313	2,385
Right inferior orbital rim	2,104	9,582	0,546	2,074	8,968	2,899	1,797	8,847	2,624

Figure B.3: Detailed TRE (Target Registration Error) Measurements from the third experiment assessing the TRE in dynamic configuration: This table showcases individual TRE calculations for various tracking combinations across different anatomical landmarks. Each row represents a unique session and anatomical landmark, with columns denoting the TRE results from specific instrument and patient tracking combinations. This is Part 1 of 2 of the comprehensive dataset.

	Instrument Tracking - Patient Tracking								
	TRE OptiTrack - OptiTrack	TRE OptiTrack - Haply	TRE OptiTrack - Fused	TRE KUKA - OptiTrack	TRE KUKA - Haply	TRE KUKA - Fused	TRE Fused - OptiTrack	TRE Fused - Haply	TRE Fused - Fused
P11 - Q11									
Midline os frontale	2,001	6,442	2,285	1,485	7,048	1,681	2,398	8,640	2,062
Glabella	0,946	6,120	0,415	0,980	6,155	0,475	1,320	6,359	0,782
Left lateral orbital rim	0,677	6,815	0,761	0,438	6,306	0,471	0,483	6,543	0,536
Right lateral orbital rim	1,294	7,849	1,349	1,130	7,480	1,225	1,047	7,826	1,095
Left inferior orbital rim	2,135	5,277	2,320	0,948	4,316	1,150	1,683	5,106	1,475
Right inferior orbital rim	1,983	4,562	2,081	0,426	3,388	0,526	0,678	3,260	0,715
P12 - S12									
Midline os frontale	1,988	10,362	2,015	2,331	11,508	2,277	3,388	12,746	3,278
Glabella	0,906	6,708	1,484	1,567	7,393	1,567	2,627	8,390	2,423
Left lateral orbital rim	1,199	7,250	0,662	1,750	7,535	1,361	3,145	8,789	2,713
Right lateral orbital rim	1,156	9,005	0,487	1,647	9,683	1,104	3,296	11,251	2,716
Left inferior orbital rim	1,930	4,448	1,856	1,644	4,495	1,453	12,207	12,726	12,227
Right inferior orbital rim	2,537	5,627	2,666	2,619	5,209	2,612	2,951	5,692	2,875
P13 - T13									
Midline os frontale	1,697	8,865	1,896	1,912	9,991	2,249	1,907	9,978	2,244
Glabella	2,009	7,195	2,040	2,811	7,884	2,851	2,756	7,857	2,799
Left lateral orbital rim	3,113	6,256	3,904	3,895	6,643	4,589	3,789	6,575	4,481
Right lateral orbital rim	3,583	6,496	4,429	4,195	6,546	5,019	4,302	6,730	5,111
Left inferior orbital rim	1,374	6,138	1,658	2,296	6,162	2,572	2,227	6,166	2,509
Right inferior orbital rim	1,435	7,804	1,445	1,618	7,579	1,753	1,589	7,461	1,732
P14 - U14									
Midline os frontale	2,211	14,023	2,203	2,696	12,031	2,720	2,569	12,088	2,590
Glabella	2,411	10,125	2,319	2,721	8,068	2,653	2,646	8,183	2,575
Left lateral orbital rim	3,214	9,950	3,757	3,196	7,708	3,032	2,985	8,011	2,878
Right lateral orbital rim	3,224	12,794	3,767	2,940	10,355	2,861	2,871	10,452	2,832
Left inferior orbital rim	1,667	5,696	1,615	2,793	4,843	2,794	2,804	4,829	2,804
Right inferior orbital rim	1,985	8,048	1,968	3,257	6,850	3,294	3,166	6,870	3,203
Q15 - S15									
Midline os frontale	0,749	11,067	0,829	1,917	10,526	1,981	1,858	10,559	1,926
Glabella	1,323	7,006	1,031	2,188	7,209	1,949	2,131	7,167	1,880
Left lateral orbital rim	2,361	6,173	2,135	2,785	7,558	2,511	2,785	7,429	2,506
Right lateral orbital rim	1,134	8,920	0,996	2,783	9,052	2,544	2,673	9,052	2,419
Left inferior orbital rim	2,150	3,741	2,090	2,145	4,240	2,048	2,125	4,190	2,030
Right inferior orbital rim	2,255	5,389	2,242	1,924	4,982	1,869	1,888	4,969	1,833
R16 - T16									
Midline os frontale	1,676	6,381	1,335	1,664	6,351	1,388	1,983	6,309	1,658
Glabella	0,675	4,774	0,825	1,205	4,073	1,647	1,207	4,089	1,624
Left lateral orbital rim	0,933	5,149	6,350	1,247	4,135	5,995	1,105	4,296	6,029
Right lateral orbital rim	1,016	6,956	3,819	1,426	5,563	3,683	1,361	5,644	3,683
Left inferior orbital rim	1,008	3,822	2,566	1,333	2,059	1,782	1,218	2,163	1,786
Right inferior orbital rim	0,796	4,767	0,586	1,539	3,806	1,654	12,222	11,191	12,297
U17 - P17									
Midline os frontale	1,372	5,195	1,448	1,376	6,170	1,662	1,149	5,706	1,431
Glabella	1,108	6,082	1,446	0,920	6,833	0,807	1,920	7,813	1,460
Left lateral orbital rim	1,125	7,381	1,128	1,270	7,663	1,154	2,265	9,191	2,474
Right lateral orbital rim	1,565	8,427	1,475	1,285	8,845	1,208	1,302	8,558	1,125
Left inferior orbital rim	2,218	3,811	1,624	1,961	4,395	1,525	2,001	4,231	1,521
Right inferior orbital rim	1,837	4,898	1,698	0,578	3,574	0,560	0,929	3,989	0,831
Median	**1,340**	**5,821**	**1,395**	**1,888**	**5,868**	**1,853**	**1,992**	**6,135**	**2,045**
Mean	**1,405**	**6,519**	**1,543**	**1,944**	**6,384**	**2,019**	**2,227**	**6,657**	**2,288**
StDev	**0,685**	**3,376**	**0,985**	**0,794**	**3,404**	**1,054**	**1,639**	**3,533**	**1,757**
Min	**0,116**	**1,798**	**0,249**	**0,426**	**0,979**	**0,381**	**0,483**	**0,950**	**0,486**
Max	**3,583**	**16,359**	**6,350**	**4,195**	**17,083**	**5,995**	**12,222**	**17,059**	**12,297**

Total number of target point	100
Total number of measureme	300
Total number of measured n	51
Total number of TRE calcula	900

Figure B.4: Detailed TRE (Target Registration Error) Measurements from Experiment 3: This table showcases individual TRE calculations for various tracking combinations across different anatomical landmarks. Each row represents a unique session and anatomical landmark, with columns denoting the TRE results from specific instrument and patient tracking combinations. This is Part 2 of 2 of the comprehensive dataset.

KUKA	KUKA_1, FRE = 0.7710	KUKA_2, FRE = 0.5618	KUKA_3, FRE = 0.6966	KUKA_4, FRE = 0.3540	KUKA_5, FRE = 0.6179	KUKA_6, FRE = 0.5200	KUKA_7, FRE = 0.6054	KUKA_8, FRE = 0.6217	KUKA_9, FRE = 0.6150
Midline os frontale	0,514	0,753	0,797	1,025	1,195	0,720	0,906	1,082	1,108
Glabella	0,353	0,380	0,511	0,602	0,297	0,383	0,639	0,646	0,706
Left lateral orbital rim	0,366	0,188	0,403	0,387	0,268	0,188	0,405	0,393	0,547
Right lateral orbital rim	0,680	0,432	0,633	0,417	0,441	0,370	0,679	0,860	0,775
Left inferior orbital rim	0,397	0,350	0,517	0,537	0,224	0,141	0,466	0,259	0,466
Right inferior orbital rim	1,353	1,007	1,512	1,142	0,972	0,619	1,161	1,052	0,716
MEAN recording	**0,610**	**0,518**	**0,729**	**0,685**	**0,566**	**0,403**	**0,709**	**0,716**	**0,720**
STDEV	0,384	0,303	0,406	0,321	0,413	0,230	0,283	0,342	0,223
Median	**0,542**								
Mean	**0,629**								
StDev	**0,301**								
Min	**1,512**								
Max	**0,141**								

OptiTrack	OptiTrack_1, FRE = 0.6048	OptiTrack_2, FRE = 0.9498	OptiTrack_3, FRE = 1.3481	OptiTrack_4, FRE = 0.7052	OptiTrack_5, FRE = 0.9229	OptiTrack_6, FRE = 0.7397	OptiTrack_7, FRE = 0.8137	OptiTrack_8, FRE = 0.9820	OptiTrack_9, FRE = 0.8300
Midline os frontale	0,538	1,715	1,251	0,429	0,615	1,226	1,100	0,840	0,641
Glabella	0,240	0,388	1,169	0,442	0,672	0,524	0,665	0,651	0,448
Left lateral orbital rim	0,256	0,382	1,350	0,365	0,901	0,239	1,288	0,492	0,550
Right lateral orbital rim	0,730	0,336	2,231	0,848	1,401	0,687	0,874	1,155	0,702
Left inferior orbital rim	0,615	1,017	0,513	0,803	0,776	0,776	1,239	0,497	0,875
Right inferior orbital rim	1,368	1,625	0,749	0,783	0,905	1,665	2,985	1,384	1,347
MEAN recording	**0,625**	**0,911**	**1,211**	**0,612**	**0,878**	**0,853**	**1,359**	**0,836**	**0,761**
STDEV	0,413	0,640	0,594	0,221	0,282	0,513	0,830	0,366	0,322
Median	**0,776**								
Mean	**0,894**								
StDev	**0,518**								
Min	**2,985**								
Max	**0,239**								
Total number of points	54								
Total number of calculations	108								

Figure B.5: Results of Experiment 4 comparing the optical tracking system OptiTrack with the dual-robot tracking system, composed of two KUKA LBR iiwa robotic manipulators, in a dynamic registration and navigation experiment.

C

Hardware

Device	Type	Workspace	Performance	Availability	Update freq.
Hexagon romer compact 7312	Coordinate measuring machine arm	1200 mm	Accuracy: 0.008 mm (MPEp)	+€60k, available for rent (€200 per day)	-
Hexagon absolute arm 8320-6	Coordinate measuring machine arm	2230 mm	Accuracy: 0.040 mm (Euni)	+€60k, available for rent (€200 per day)	-
Haply Inverse3	Haptic interface device	Translational: 510 x 230 x 460 mm	Resolution: 0.2 mm position, 16 bit quaternion orientation	€4675	4000 Hz positional, 60 Hz rotational
Haption desktop virtuose 6D	Haptic interface device	Rotational: 270 x 120 x 250°, Translational: 520 x 220 x 400 mm	Resolution: 0.023 position, 0.0023 deg rotation	€27000	1000 Hz
Haption desktop virtuose 3D	Haptic interface device	Rotational: 260 x 105 x 360°, Translational: 520 x 220 x 400 mm	Resolution: 0.023 position, 0.35 deg rotation	€13500	1000 Hz
Franka Emika Research	Robotic manipulator	855 mm	Repeatability: 0.001 mm	Available at TUD	1000 Hz
Mecademic	Robotic manipulator	330 mm	Repeatability: 0.005 mm	€15000	+1000 Hz
OptiTrack Prime	Motion capture camera	9m	3D accuracy: 0.3mm	€2500, available at TUD	240 FPS
Kuka LBR iiwa R800	Robotic arm	800 mm	0.1 mm (ISO 9283)	Reservation TUD	Not provided
Kuka LBR iiwa R820	Robotic arm	820 mm	0.15 mm (ISO 9283)	Reservation TUD	Not provided

Table C.1: Selection of possible hardware solutions for the surgical navigation setup, different components could both be used as patient and instrument tracking methods.